ADVANCED SIGNAL PROCESSING TECHNIQUES FOR NOISE SOURCE IDENTIFICATION IN MINING EQUIPMENT

by

John Patrick Homer

BS Mechanical Engineering, The Pennsylvania State University, 2000

Submitted to the Graduate Faculty of

the School of Engineering in partial fulfillment

of the requirements for the degree of

Master of Science in Mechanical Engineering

University of Pittsburgh

2003

UNIVERSITY OF PITTSBURGH

SCHOOL OF ENGINEERING

This thesis was presented

by

John Patrick Homer

It was defended on

April 11, 2003

and approved by

William W. Clark, Ph. D., Associate Professor, Mechanical Engineering

Dipo Onipede, Jr., Ph. D., Assistant Professor, Mechanical Engineering

Thesis Advisor: Jeffrey S. Vipperman, Ph. D., Assistant Professor, Mechanical Engineering

ABSTRACT

EVALUATION OF ADVANCED SIGNAL PROCESSING TECHNIQUES USED FOR NOISE SOURCE IDENTIFICATION IN MINING EQUIPMENT

John Patrick Homer, MS

University of Pittsburgh, 2003

This thesis presents the analysis of five measurement techniques used to identify noise sources and transmission paths of a chain conveyor / motor test bed. The measurement techniques are: near-field sound pressure, sound intensity, structural tap testing, coherent power, and enhanced time measurements. Sound pressure is inherently measured with sound intensity, and thus both of these were used to identify noise sources and spectral distributions along the surface of the chain conveyor test bed. Tap tests were used to identify the vibration characteristics of individual system sections and to identify structural resonances that potentially radiate noise. There are two types of coherent power measurements analyzed in this thesis. The first is the Frequency Response Function (FRF) approach, which was used to estimate individual source contributions to a specific receiver. A more sophisticated coherent power method is the Partial Coherence Function (PCF) approach, which is capable of identifying unique contributions of system noise sources. Finally, enhanced time measurements were performed. These measurements are capable of identifying specific events in a repetitive process, since averaging

is performed in the time domain. A trigger signal is created from some event in the cyclic process. All of these methods proved to be valuable for identifying noise sources in mining equipment, especially when performing analyses in a less than ideal measurement environment. References will be made about the application of these noise source identification techniques on more complex mining equipment.

ACKNOWLEDGEMENTS

Funding and equipment for the research presented in this thesis was provided by the NIOSH agency and the University of Pittsburgh. First, I would like to thank my advisor Dr. Jeffrey S. Vipperman for his guidance, motivation, and support through the duration of my graduate study. Second, I would like to thank Dr. Efrem Reeves, Deyu Li, Fatih Ayhan, Bob Barbish, and Angela Flamm for their contributions to my research. Finally, I would like to thank the committee members Dr. William W. Clark and Dr. Dipo Onipede Jr. for participating in the defense of my thesis. I would especially like to acknowledge my family and friends for their continuous support and motivation.

TABLE OF CONTENTS

LIST OF TABLES

LIST OF FIGURES

1.0 INTRODUCTION

Hearing loss is one of the most common disabilities associated with the mining industry. The Mine Safety and Health Administration (MSHA) reported that "in many U.S. mines, the miners are exposed to extremely loud and sustained noise levels. MSHA estimates that unless something is done, 13 percent of U.S. miners - about 37,000 will suffer a significant loss of hearing" [24]. In 2001 alone, 151 hearing loss cases, which constitute 18.9 % of all mining occupational illnesses, were reported to MSHA [30]. Analyses of mining related hearing loss have revealed that many miners suffer from a severe case of hearing loss. For example, it was discovered that "at age 60, over 70 % of all miners had a hearing loss greater than 25 dB, and about 28 % had a hearing loss greater than 40 dB" [2]. This evidence suggests that the extent and severity of hearing loss in the mining industry is of great proportion.

Hearing loss in miners is caused by prolonged exposure to severe noise levels produced by the operation of heavy equipment. The confined nature of mining environments greatly contributes to the severity of these noise levels. This type of hearing loss, known as Noise-Induced Hearing Loss (NIHL), permanently damages the auditory system [35]. The victim's ability to communicate is impaired; isolating them from society and severely compromising their social and mental health.

"Job-related hearing loss, however, can be diagnosed, and prevented or reduced in severity" [24]. Typical methods of prevention include auditory protection and the implementation of engineering and administrative controls in the work place. Due to the adverse effects of hearing loss and its prevalence in the mining industry, new federal regulations have been developed by MSHA. These regulations define dose limitations for miners and require the use of certified protection in areas with high noise levels. Further, MSHA requires that miners

exposed to environments with average continuous sound levels of 85 dBA or greater over an eight-hour shift receive special training, hearing tests, and hearing protection. If levels meet or exceed 90 dBA for an eight-hour shift, feasible engineering and administrative controls must be used to reduce noise levels. More sophisticated protection must be provided to miners in environments of 105 dBA or greater. Finally, miners are never permitted to enter areas where levels exceed 115 dBA [31]. The Occupational Safety and Health Administration (OSHA) has also developed federal regulations regarding occupational noise exposure that apply to all of industry in the United States except mining. Permissible noise exposures are outlined in OSHA Noise Standard 1910.95 and summarized in Table 1 [29, 32].

Table 1 Permissible Noise Exposures [29, 32]

Duration per day (hrs)	Sound Level (dBA)
8	90
6	92
4	95
3	97
2	100
1 ½	102
1	105
½	110
¼	115

Noise regulations present the need for effective methods of identifying the acoustic and vibration properties of harmful environments and their sources so that extreme levels can be effectively reduced. Noise reduction can be achieved by either isolating or removing the noise source, or by altering the transmission path [16]. In order to accomplish these objectives, the noise source must first be identified, followed by identification of the transmission path. The spectrum of an acoustic signal is also helpful for identifying a noise source [8]. This information is then examined and used to propose an effective noise reduction solution [7, 8, 23, 29, 36]. There are various techniques available to identify, rank, and determine acoustic properties of noise sources and their transmission; however, the worth and feasibility of many techniques is

unknown for mining applications. Subsequently, the National Institute of Occupational Safety and Health (NIOSH) is currently evaluating *in-situ* noise source identification and classification techniques for analysis of mining equipment.

The purpose of this thesis is to select and evaluate the effectiveness of advanced signal processing techniques used for noise source / path identification. The techniques are examined on a chain conveyor test bed, which is a simplified subcomponent of a continuous coal miner [3]. Noise source identification techniques that were examined involve measurements of near-field sound pressure, sound intensity, structural modal response, coherent power, and enhanced time pressure and vibration. Conclusions regarding these techniques and their ability to identify noise sources, transmission paths, and spectral properties of the test system will be made. Additionally, insight into reducing damaging sound levels produced by mining equipment will be provided.

Sound pressure can be used to calculate sound power and identify noise sources when measured in the free-field [25, 34]. Controlled environments such as anechoic and reverberant chambers provide suitable conditions for sound pressure measurement to be used for sound power calculations [4, 34]. When measured in the near-field, also called the evanescent field, sound pressure measurements for sound power typically yield unreliable results [34]. This is due to the fact that a portion of the sound field is reactive [34]. However, since near-field sound pressure measurements were necessary to determine sound intensity, they will also be used to identify potential noise sources and spectral characteristics along the surface of the test bed.

Sound intensity measurements have been successfully utilized on complex mechanical systems such as diesel engines to identify noise sources and calculate sound power [15]. The results of this technique have proven accurate when compared to methods such as surface intensity and wrapping techniques [15]. Also known as acoustic intensity, this measurement produces repeatable results for noise control applications in any acoustic fields [13, 34]. Noise source ranking and identification is accomplished by mapping intensity over a conformal surface to the system, known as contour plotting [14, 19, 34, 36]. Broadband intensity measurements also provide the spectral content of a noise source [15, 34]. Near-field sound pressure measurements will be compared to sound intensity, the latter of which are much more complex to perform.

Tap tests can be performed on a structure in order to identify its modal parameters [33, 36]. Lightly damped structural modes can radiate sound when excited [18]. The spectral response of a structure can be compared with acoustic spectra to help identify frequencies where structural radiation exists. Common peaks in the structural and acoustic spectra typically indicate such a condition.

Coherent power measurement techniques can also be used to identify noise sources (inputs) and their spectral contributions to the overall noise of a receiver (output) [10, 11, 16]. There are two different coherence techniques, which are known as the Frequency Response Function (FRF) and Partial Coherence Function (PCF) methods [16]. The FRF method is used to relate the output to the inputs of a system [16]. This method can also be used to identify the contribution from each individual source to the receiver. Note that an individual source contribution determined using the FRF method is equivalent to the expected output in the absence of all other inputs. The PCF method is used to identify the unique contribution of each input to the output in a Multiple Input Single Output (MISO) system [10, 11, 16]. Note that the PCF method includes only the unique portion of the source contribution, excluding portions coherent with other sources. Both of these techniques can also be used to identify the spectral distribution of a source contribution. Coherent power measurement techniques can be performed on any combination of signal transducers (e.g. accelerometers and microphones), since the calculations used to obtain the results are independent of measurement quantities.

The periodic content of signals produced by a cyclical system can be identified using enhanced time measurements [20, 22, 28, 37]. This technique provides the means to average unwanted noise from a time-domain signal through the use of a synchronous trigger signal [37]. Enhanced time measurements are used to separate specific events of a cycle, such as a pump valve opening and closing, which in turn can be used for noise control design [23]. Note that uniformly spaced conveyor components comprise a periodic event when operated at a constant speed.

These five methods are evaluated on the chain conveyor test bed in order to learn about the mechanisms and possible control of noise in this system, as well as to evaluate the suitability of the methods themselves for *in-situ* analyses of mining equipment. The theoretical foundations are laid in chapter 2. Chapter 3 describes the test bed and measurement conditions. In chapter 4, the data from each of the five techniques are presented, followed by a summary and conclusions in chapter 5. The conclusions and experience obtained from analyzing the test bed were used to determine the effectiveness of the advanced signal processing techniques evaluated in this thesis. Recommendations for future evaluation of noise source investigation techniques and the application of the techniques analyzed in this thesis are also disclosed. Dynamic capability / pressure-intensity index plots regarding the sound intensity probe and data used for this analysis are presented in Appendix A. Additional pictures of the chain conveyor / motor test bed are included in Appendix B.

2.0 ADVANCED SIGNAL PROCESSING TECHNIQUES

Each of the five techniques used for noise source / transmission path identification on a chain conveyor / motor test bed are presented in greater detail below. They are near-field sound pressure, sound intensity, tap testing, coherent power, and enhanced time measurements. Some of these techniques are derived from basic quantities such as sound pressure. Alternatively, other techniques utilize multiple quantities both mathematically and comparatively to arrive at conclusions about system noise sources.

2.1 Near-Field Sound Pressure

Sound pressure level measurements can be used to identify noise sources by associating their specific location with high sound pressure levels, but only when measurements are taken in the free-field or an anechoic or reverberant sound field [34]. Neither of these environments was available for testing performed on this system, as is typical for *in-situ* analyses of large equipment. However, since sound pressure is more easily obtainable than sound intensity the results of *in-situ* near-field sound pressure level measurements will be evaluated in this thesis. The specific objective of the near-field sound pressure level analysis is to determine the ability of measurements taken in a less than ideal environment to identify noise sources.

Sound pressure data for discrete frequency points are obtained by taking the square root of the auto-spectral density, also the power spectrum, $G_{yy}(\omega)$ (V_{rms}^2) measured from a microphone y with a dynamic signal analyzer and multiplying the results by the calibration factor K_p (Pa / V) of the microphone to obtain the sound pressure level spectrum $p_{rms}(\omega)$ (Pa). These quantities can be put into standard logarithmic format by utilizing the equation

$$SPL(\omega) = 20\log_{10}\left(p_{rms}(\omega)/p_{ref}\right)\ dB, \qquad (2\text{-}1)$$

where $p_{rms}(\omega) = \sqrt{G_{yy}(\omega)}\ K_p$ and p_{ref} = 20x10^{-6} Pa [12]. In theory, the power spectrum of a continuous signal *y(t)* is determined using the Fourier Transform of the signal *Y(ω)* according to the following formula

$$G_{yy}(\omega) \;=\; 2\lim_{T\to\infty}\frac{1}{T}Y^{*}(\omega)Y(\omega)\,, \qquad (2\text{-}2)$$

where $Y^{*}(\omega)$ denotes the complex conjugate of *Y(ω)* [9]. However, real-world measurements are taken with a dynamic signal analyzer which produces discrete time signal values that can be easily converted to discrete frequency data using the Fast Fourier Transform. All sound pressure and sound intensity results are A-weighted in this thesis because the results are ultimately used in regard to what is experienced by the human ear.

2.2 Sound Intensity

Sound intensity is a vector quantity describing the rate of sound energy flow per unit area normal to the direction of travel in units of power per area. Measurements taken across the surface of a system can be used to identify noise sources associated with locations having the highest outward intensity levels. When measured in the free-field, the sound pressure level (*SPL*) and sound intensity level (*IL*) are nearly equal [12]

$$IL \;=\; SPL \;-\; 0.16\ dB \;\approx\; SPL\,, \qquad (2\text{-}3)$$

and sound power can be accurately approximated from sound pressure measurements. Thus, the identification of noise sources using sound pressure is more accurate when measured in a non-reactive field.

Sound intensity, in theory, is determined by taking the time-averaged product of pressure and particle velocity [34]. Particle velocity can be estimated using the signals from two microphones located a known distance apart and aligned with the direction in which particle velocity and, hence, sound intensity are to be measured. This is typically accomplished using a sound intensity probe, as in Figure 1 [34].

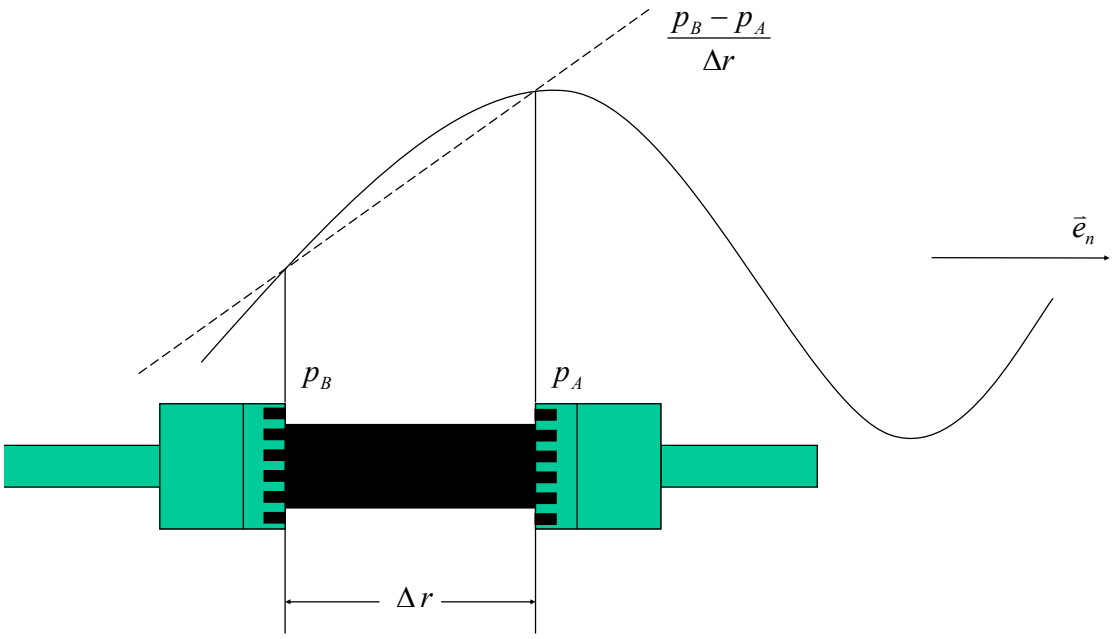

Figure 1 Sound Intensity Probe Configuration [34]

Particle velocity is calculated using the Finite Difference Approximation which is stated as follows:

$$\vec{u} = -\frac{1}{\rho} \int \frac{p_B - p_A}{\Delta r} \, dt \;\; \vec{e}_n , \tag{2-4}$$

where ρ (kg/m^3) is the density of air, p_A (Pa) and p_B (Pa) are pressures measured by the two microphones, Δr (m) is the distance between the two microphones, and $\vec{e}_n$ is the unit normal vector directed from p_B towards p_A [34]. Positive velocity flows in the direction of p_B towards p_A making p_B the measurement closest to the sound energy source. Average pressure is used when calculating sound intensity as [34]

$$p = \frac{p_A + p_B}{2}. \tag{2-5}$$

The sound intensity vector is then calculated by the following formula [34]

$$\vec{I} = \overline{p \cdot \vec{u}} = -\frac{p_A + p_B}{2\rho \Delta r} \int \left(p_B - p_A \right) \, dt \;\; \vec{e}_n . \tag{2-6}$$

When using a dynamic signal analyzer to determine sound intensity the following formula is used

$$\vec{I}(\omega) \;=\; -\frac{1}{\rho\,\omega\,\Delta r}\,\mathrm{Im}\left(G_{AB}(\omega)\right)\;\vec{e}_n\,, \tag{2-7}$$

where Im( ) represents the imaginary part, $G_{AB}(\omega)$ (V^2) is the cross-spectrum between the two microphone measurements, and ω (rad/s) is the circular frequency of each corresponding discrete value of the cross-spectrum [34]. Theoretically, the cross-spectrum of two continuous signals *a(t)* and *b(t)* is determined using the Fourier Transform of the signals $A(\omega)$ and $B(\omega)$ according to the following formula

$$G_{AB}(\omega) \;=\; 2\lim_{T\to\infty}\frac{1}{T}\,A^{*}(\omega)\,B(\omega)\,, \tag{2-8}$$

where $A^{*}(\omega)$ denotes the complex conjugate of $A(\omega)$ [9]. Since the cross-spectrum G_{AB} has units of volts squared (V^2) it must be multiplied by the calibration factor K_p (Pa / V) of each microphone in order to obtain sound intensity $\vec{I}$ with units of watts per meter squared (W/m^2). These quantities can be put into standard logarithmic format by utilizing the equation

$$IL \;=\; 10\log_{10}\left(I/I_{ref}\right)\;dB\,, \tag{2-9}$$

where $I=\left|\vec{I}\right|=\left|G_{AB}K_p\;\vec{e}_n\right|$ and $I_{ref}= 10^{-12}$ W/m^2 [12].

The usable frequency band of sound intensity data is physically limited by the separation distance Δr of the two microphones. The wavelength cannot be very large or small compared to the spacing Δr. The frequency band for which sound intensity data are accurate can be precisely determined by comparing the dynamic capability of the sound intensity probe microphones to the pressure-intensity index of the measurement. The dynamic capability is determined using a sound intensity calibrator and the Pressure-Intensity Index (PII) is the difference between pressure and intensity levels (PII = SPL - IL). Sound intensity measurements are accurate in the frequency band where the pressure-intensity index is less than the dynamic capability of the sound intensity probe. Appendix A contains residual pressure-intensity index calibration plots from the probe used to measure data for this thesis. It was found that the usable bandwidth of the sound intensity probe was substantially greater than the very conservative specification provided by the manufacturer.

2.3 Tap Tests

Tap tests are performed on physical structures in order to determine their modal frequencies and damping ratios. Modal frequencies of a structure can be extracted from Frequency Response Function (FRF) data which is derived from signals produced by inducing an impulsive force on the structure with a modally tuned hammer (input x) and measuring the response with an accelerometer (output y). A dynamic signal analyzer is used to measure the input and output signals and produce complex-valued frequency response data, $H(\omega)$, over the analysis spectrum. The FRF is calculated using the following relation

$$H(\omega) = \frac{X^*(\omega)Y(\omega)}{X^*(\omega)X(\omega)} = \frac{G_{xy}(\omega)}{G_{xx}(\omega)}, \tag{2-10}$$

where $G_{xx}(\omega)$ is the auto-spectrum of input x, $G_{xy}(\omega)$ is the cross-spectrum between input x and output y, $X(\omega)$ is the Fourier Transform of the signal $x(t)$ from input x and $Y(\omega)$ is the Fourier Transform of the signal $y(t)$ from output y [7, 9, 12, 33]. The complex-valued frequency response function $H(\omega)$ data can be translated into real valued magnitude $|H(\omega)|$ and phase $\Phi(\omega)$ components according to the following formulas [9, 33]

$$\begin{aligned} |H(\omega)| &= \sqrt{(\mathrm{Re}(H(\omega)))^2 + (\mathrm{Im}(H(\omega)))^2} = \frac{\sqrt{(\mathrm{Re}(G_{xy}(\omega)))^2 + (\mathrm{Im}(G_{xy}(\omega)))^2}}{G_{xx}(\omega)} \\ \Phi(\omega) &= \tan^{-1}\left(\frac{\mathrm{Im}(H(\omega))}{\mathrm{Re}(H(\omega))}\right) = \tan^{-1}\left(\frac{\mathrm{Im}(G_{xy}(\omega))}{\mathrm{Re}(G_{xy}(\omega))}\right) \end{aligned}. \tag{2-11}$$

Real valued magnitude and phase data can be plotted versus frequency to observe the spectral distributions of the structural frequency response function.

2.4 Coherent Power Measurements

Coherent power measurements can be utilized in multiple noise source environments to identify and rank noise sources while developing a more thorough understanding of the contributions from structure-borne and air-borne noise sources to specific receivers [16]. Coherence techniques used in this thesis are performed using the following two methods.

2.4.1 Frequency Response Function (FRF) Method

The Frequency Response Function (FRF) method utilizes the FRF between each source and receiver and the auto-spectral density of that source to estimate the contribution to the auto-spectral density measured at the receiver. The auto-spectral contribution from a source x_1 to the receiver y for a well-defined linear time-invariant system is calculated using the following equation

$$G_{yy\_1}(\omega) = H_1^*(\omega)\ G_{11}(\omega)\ H_1(\omega), \tag{2-12}$$

where $H_1^*(\omega)$ is the complex conjugate of $H_1(\omega)$, the frequency response function between input x_1 and output y, and $G_{11}(\omega)$ is the auto-spectral density of the input x_1 [16]. The quantity G_{yy_1} represents the spectral contribution of source x_1 to G_{yy}, which is also the expected auto-spectral density of output y in the absence of all other sources [16]. Note that the results of this equation are most accurate when there is very little coherence between sources. High levels of source coherence would indicate that source contributions include portions common to multiple sources. The next section presents a more sophisticated method that is capable of identifying the unique contributions of multiple system noise sources.

2.4.2 Partial Coherence Function (PCF) Method

The Partial Coherence Function (PCF) method is used to determine the unique contribution of a source to a receiver using the coherent residual spectral density function. This is achieved by removing the effects of all sources in the system except the unique contribution of the source under investigation from the auto-spectral density of the receiver [16].

PCF analysis results are represented with symbolic notation which consists of ($\gamma^2_{**.***}$) terms and ($G_{**.***}$) terms. Terms denoted as $\gamma^2_{**.***}$ represent partial coherence functions and terms denoted as $G_{**.***}$ represent residual auto-spectral and residual cross-spectral density functions [16]. A $G^{**}.^{***}$ term preceded by a $\gamma^2_{**.***}$ term describes a coherent residual spectral density function [16]. For example, consider a system consisting of four sources (x_1, x_2, x_3, x_4) and a single receiver (y). The notation $\gamma^2_{1y.234}$ represents the partial coherence between source x_1 and receiver y less the effects of sources x_2, x_3, and x_4 [11]. Notation $G_{55.234}$ represents

the residual auto-spectrum of receiver y due to the unique effect of source x_1 and less the effects of sources x_2, x_3, and x_4, hence in a well defined system the contribution from source x_1 to receiver y [11]. In this case, $\gamma^2_{1y\cdot 234}\, G_{yy\cdot 234}$ represents the coherent residual auto-spectral density of receiver y from source x_1, derived by eliminating the effects of sources x_2, x_3, and x_4 [16].

The residual auto-spectral density functions of a multiple input (x_1, x_2, x_3, …, x_i) single output (y) system are computed using the following equations [11]

(auto-spectral)
$$G_{yy.1} = G_{yy}\left(1-\gamma^2_{1y}\right), \tag{2-13}$$

$$G_{yy.12} = G_{yy.1}\left(1-\gamma^2_{2y.1}\right), \tag{2-14}$$

$$G_{yy.123} = G_{yy.12}\left(1-\gamma^2_{3y.12}\right). \tag{2-15}$$

The partial coherence functions used in equations (2-13) through (2-15) are obtained using the following formulas [11]

(coherence)
$$\gamma^2_{iy} = \frac{\left|G_{iy}\right|^2}{G_{ii}G_{yy}} = \gamma^2_{yi}, \tag{2-16}$$

$$\gamma^2_{iy.1} = \frac{\left|G_{iy.1}\right|^2}{G_{ii.1}G_{yy.1}} = \gamma^2_{yi.1}, \tag{2-17}$$

$$\gamma^2_{iy.12} = \frac{\left|G_{iy.12}\right|^2}{G_{ii.12}G_{yy.12}} = \gamma^2_{yi.12}. \tag{2-18}$$

The residual cross-spectral density functions used in equations (2-16) through (2-18) are obtained using following formulas

(cross-spectral)
$$G_{iy.1} = \frac{G_{11}G_{iy} - G_{i1}G_{1y}}{G_{11}}, \tag{2-19}$$

$$G_{iy.12} = \frac{G_{22.1}G_{iy.1} - G_{i2.1}G_{2y.1}}{G_{22.1}}, \tag{2-20}$$

$$G_{iy.123} = \frac{G_{33.12}G_{iy.12} - G_{i3.12}G_{3y.12}}{G_{33.12}}, \tag{2-21}$$

where the *1*, *2*, *3*, *i*, and *y* indices can be interchanged and/or added throughout any of the equations above in order to obtain necessary results [11]. Note that the results of the coherent residual spectral density function are most representative of the sources' contribution to the receiver when there is very little coherence between the sources. The coherent residual spectral density function represents the unique contributions from the source excluding contributions common with other sources [16].

2.5 Enhanced Time Measurements

Enhanced time measurements are used to determine components of a signal related to a system event which undergoes cyclic or repetitive motion. This is accomplished by time averaging the signal using a trigger signal synchronous with the periodic event of interest. A signal obtained by frequency domain averaging is represented by the following equation

$$G_{yy} = G_{aa} + G_{nn}, \tag{2-22}$$

where G_{yy} is the auto-spectrum of the signal averaged in the frequency domain, G_{aa} is the deterministic portion of the signal related to the periodic event of interest, and G_{nn} is the uncorrelated portion or noise component of the signal [37]. Enhanced time averaging and post-processing with the Fast Fourier Transform permits the uncorrelated noise component G_{nn} of the frequency averaged signal G_{yy} to be averaged out of the results revealing the deterministic component G_{aa} [28, 37]. The deterministic component G_{aa} represents the cyclic portion of a signal correlated with the periodic event of interest. This component presented in the time domain represents the deterministic signal response relative to the trigger signal event and can be used to correlate intense portions of the time signal to specific events in the cycle. For time domain averaging equation (2-22) becomes

$$G_{yy} = G_{aa} + \frac{1}{N_a} G_{nn}, \tag{2-23}$$

where N_a is the number of averages. "Every time the number of averages is increased tenfold, the noise component is reduced by 10 dB, i.e. Reduction = 10 x log(N_a)", where N_a is the number of averages [37].

3.0 TEST SETUP AND PROCEDURE

Analysis was performed on a chain conveyor / motor test bed provided by NIOSH, as shown in Figure 2. The test bed was located inside a building and had many walls or objects within close proximity. For example, there was a steel wall located approximately three feet behind the conveyor and motor as shown in Figures 2 and 3. There was also a steel stair case and structure approximately three feet to the left of the conveyor as shown in Figures 2 and 3, which would be largely acoustically transparent at low frequencies. A measurement environment of this nature is cumbersome to accurately identify noise sources in due to the presence of very complex reflective surfaces within close proximity to the test bed. However, this is very typical of *in-situ* noise measurements performed on large industrial equipment.

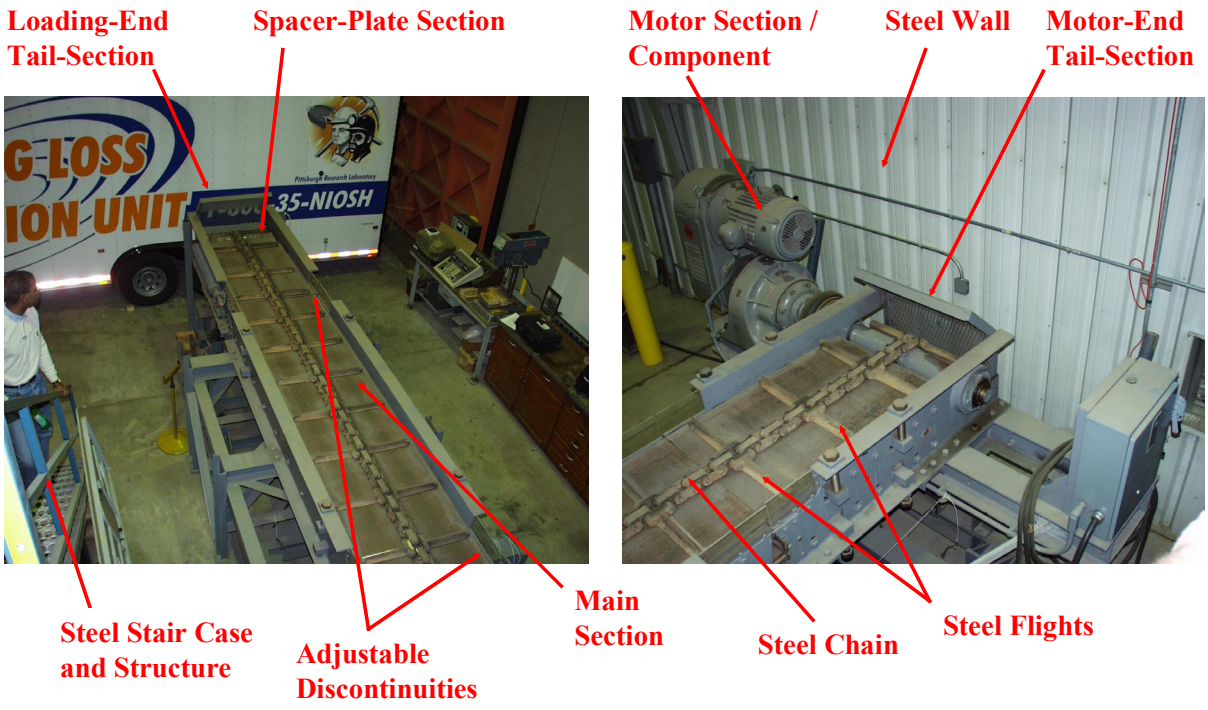

Figure 2 Chain Conveyor / Motor Test Bed

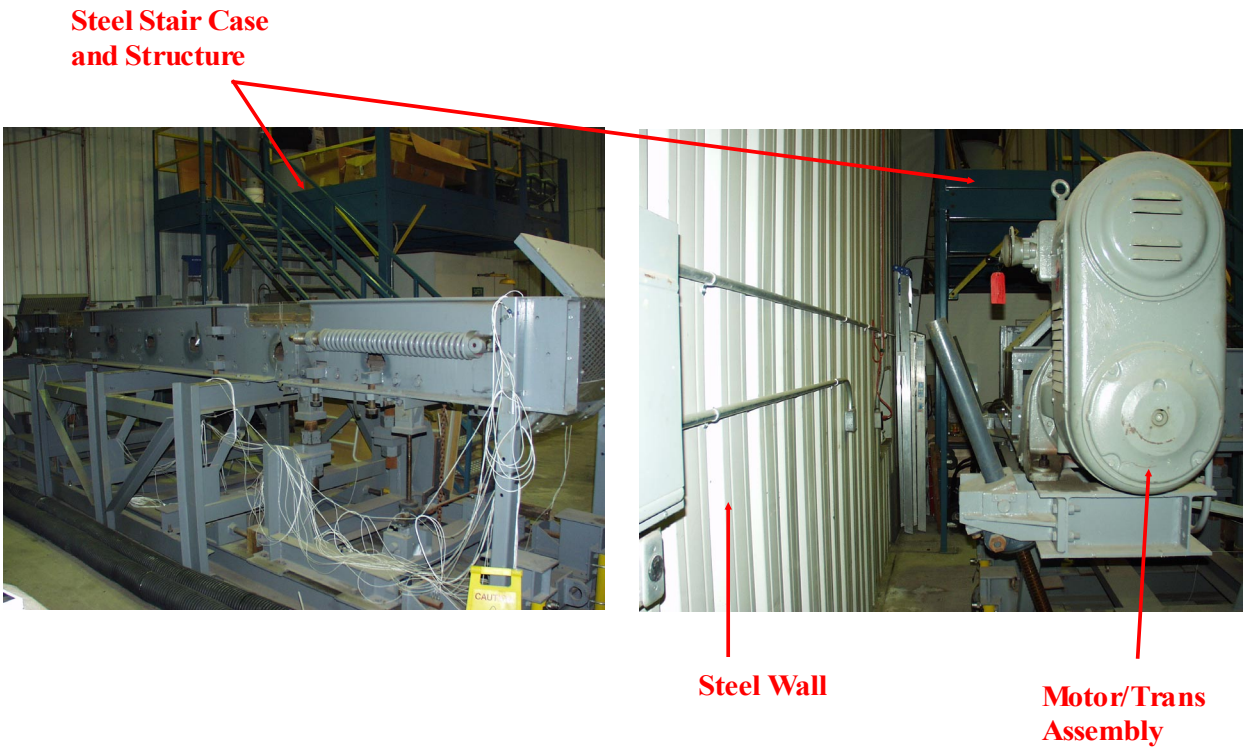

Figure 3 Reflective Surfaces

A chain conveyor is but one component of complex mining machines, such as continuous miners or long wall miners. This simplified mockup of just a chain conveyor / motor system was used for testing in order to simplify measurement complexity, while evaluating novel measurement methods. In order to more easily present the findings, the surfaces of the test bed were "unfolded" into sections and labeled as shown in Figure 4. The entire system consists of two components, the conveyor and the motor, where the conveyor component is further divided into twelve sections for a total of thirteen separate sections.

All measurements used in this thesis were taken with a SIGLAB 20-42 dynamic signal analyzer. The data were post-processed using MATLAB to create graphical and tabular results. The results were collected using Microsoft's Power Point and Excel software.

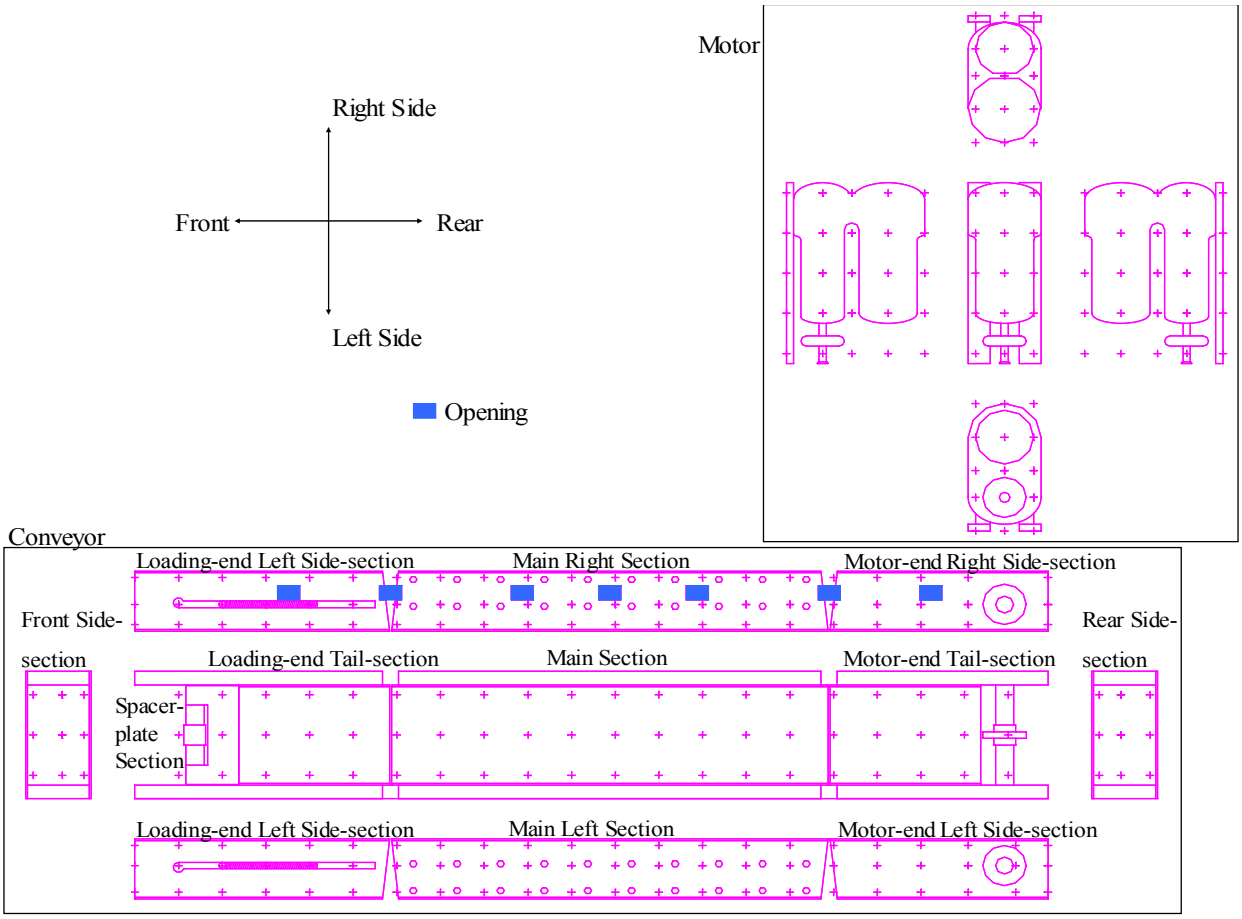

Figure 4 Chain Conveyor / Motor Section Layout

3.1 Speed Properties

The unloaded chain conveyor / motor test bed was operated and analyzed at two different speed settings. The speeds analyzed were set on the motor speed control and are referred to as speed 1 and speed 4 throughout the remainder of this thesis. Speed 1 and speed 4 settings have corresponding linear velocities of the chain and flights and drive shaft angular velocities as given in Table 2. These values were determined by time averaging ten revolutions of the chain at each speed to determine the angular speed, in Rotations Per Minute (RPM), of the chain and by measuring the length of the chain. The length of the chain was calculated by counting the number of flights and measuring the distance between each flight.

Table 2 Chain Conveyor / Motor Speed Data

Flights	Flight Spacing (in)	Chain Length (in)
29	15.75	462

Drive-gear Teeth	Drive-links	Idler-links	Connecting-links	Drive Ratio
5	88	88	176	17.6

	Measured Data		Chain		Drive Shaft
	Chain Revolutions	Time (sec)	Angular Velocity (RPM)	Linear Velocity (ft/sec)	Angular Velocity (RPM)
Speed 1	10	228.13	2.63	1.69	46.29
Speed 4	10	84.32	7.12	4.57	125.24

In order to provide specific frequencies associated with the speed of the system, operating frequencies of system components were determined. The identified frequencies were that of "flight passing frequency", "drive-link passing frequency", and "connecting-link passing frequency", which are listed in Table 3. The distinction between drive-links and connecting-links is as follows. Drive-links are comprised of every other link in the chain, which have a hole

in the center that accepts the drive-gear teeth where connecting-links consist of all links (drive-links and idler-links) included in the chain as shown in Figure 5. Note that flights are attached to idler-links and there are twice as many connecting-links as drive-links.

Table 3 Passing Frequency Values

	Flights	Links	
	Flight Passing Frequency (Hz)	Drive-link Passing Frequency (Hz)	Connecting-link Passing Frequency (Hz)
Speed 1	1.29	3.86	7.71
Speed 4	3.48	10.44	20.87

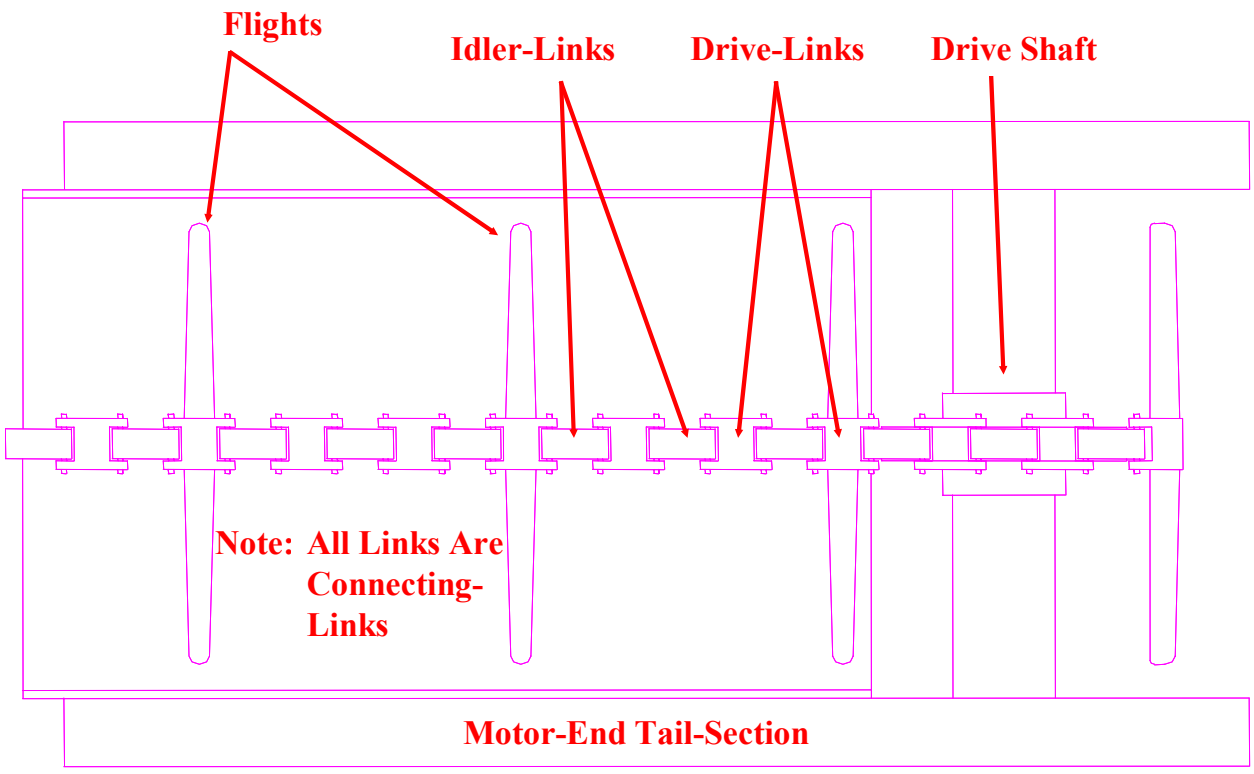

Figure 5 Chain and Drive Components

3.2 Near-Field Sound Pressure / Sound Intensity

Near-field sound pressure level and sound intensity measurements were taken every square foot according to a conformal grid formed along the surface of the system at speeds 1 and 4. All sound intensity measurements are normal to the surface of the system. The measurement grid consists of 301 points that can be identified by the cross-hair marks in Figures 4 and 6, producing a total of 602 data files for the sound pressure and sound intensity analyses. String, a tape measure, and a permanent marker were used to accurately locate and mark measurement points on the surface of the test bed. The axial and transverse grid points were numbered or labeled, as shown in Figure 6, to establish a naming convention for the near-field sound pressure and sound intensity data files.

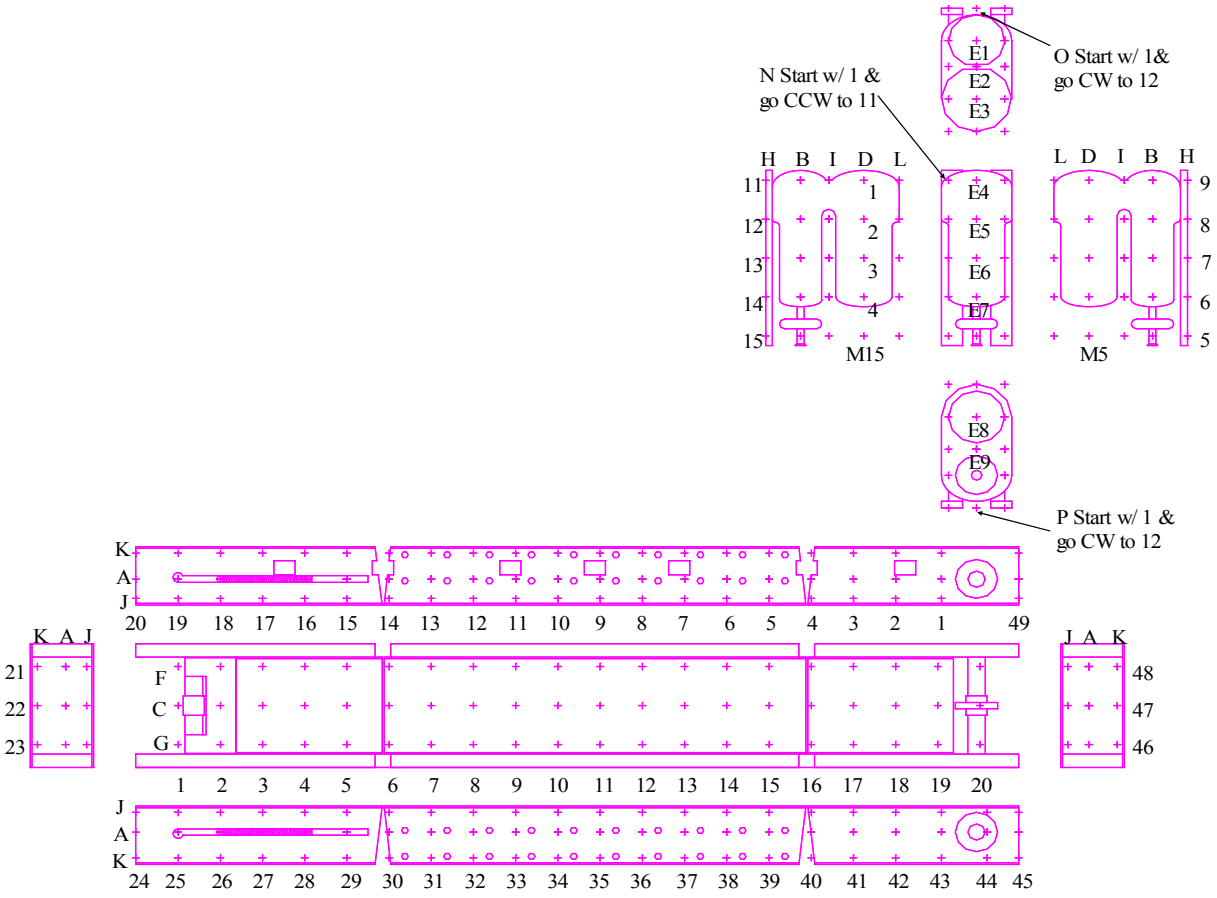

Figure 6 Sound Intensity / Near-Field Sound Pressure Level Measurement Point Grid

Near-field sound pressure level measurements were taken with a Brüel & Kjær 3519 sound intensity probe at 6 inches from the test bed surface for speeds 1 and 4. Measurements were taken using two phase matched Brüel & Kjær 4181 ½" condenser microphones and a Brüel & Kjær 5935 dual microphone supply. The probe was held approximately 4 feet to the side, orthogonal to the direction of flow, of the measurement point in order to avoid interference from the data collector's body. Positioning of the probe was held constant at each measurement point by using fixed visual reference points and markings placed on the surface. These measurements were used to produce broadband, 1/3-octave, and overall near-field sound pressure (20-20,000 Hz) and sound intensity (20-4,000 Hz) plots for select measurement points. They were also used to produce 1/3-octave and overall near-field sound pressure level and sound intensity contour plots. These contour plots were used to better understand and identify the sound pressure level and sound intensity distributions along the surface of the chain conveyor / motor test bed.

Maximum and minimum values were determined for Near-Field Sound Pressure Level (NF SPL) and Sound Intensity (SI) measurements. This was necessary to draw conclusions about the chain conveyor / motor system's sound pressure and sound intensity surface distributions. The following extremes were determined for each of the thirteen sections, the conveyor component, and the entire system from the NF SPL and SI data:

Near-field Sound Pressure Level / Sound Intensity Extremes:

1.) max / min level of each 1/3-octave
2.) max / min level of all 1/3-octaves
3.) max / min overall level

Tables and plots associated with these extremes will be presented in chapter 4. The reader is reminded that the entire system, conveyor component, motor component, and each of the thirteen sections referred to above can be identified through reference of Figure 4.

3.3 Tap Tests

Vibration tap tests were performed on six of the thirteen sections using six PCB 352C22 accelerometers, a PCB 086C03 modal hammer, and two PCB 442A104 ICP sensor signal conditioners powered by PCB 441A101 AC power supplies to measure frequency response function data. The material of the hammer tip was selected to maximize input to the system for each frequency band being measured. The accelerometers were attached using beeswax and positioned to capture structural modes. The arrangement of input and output points for each section can be seen in Figure 7 where the circles represent the hammer input locations and the other shapes represent the six accelerometer measurement points for each section. For data identification purposes, the six measurement configurations were color coded for each section. Nine data files were taken for each of the six sections resulting in a total of 54 data files. Each file contained transfer function data over a 1 kHz zoomed frequency band with a 10 Hz overlap between data files. The analysis covers the 20-8,000 Hz frequency band. Transfer function data were plotted along side sound pressure level data for speeds 1 and 4. A total of 324 plots were created (6 accelerometers over 6 sections with 9 plots per section). These plots were used to identify frequencies where structural radiation may exist.

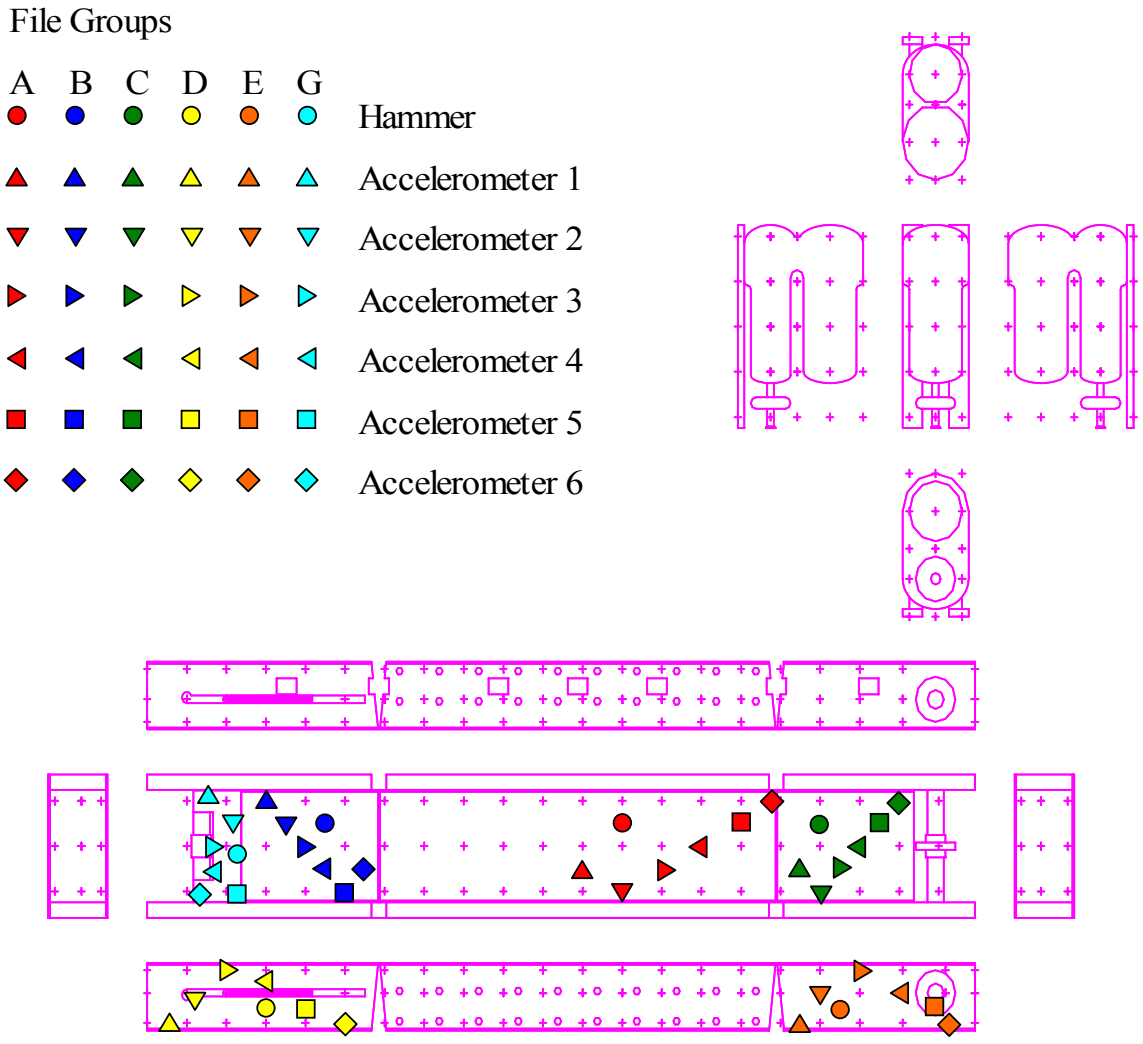

Figure 7 Tap Test Measurement Configurations

3.4 Coherent Power Measurements

Coherent power measurements were taken at various points on the system using five Brüel & Kjær 4188 microphones with Brüel & Kjær 2671 ICP compatible preamps and eight PCB 352C22 accelerometers which were all connected to two PCB 442A104 ICP sensor signal conditioners powered by PCB 441A101 AC power supplies at speeds 1 and 4. The measurement points are shown in Figure 8. Note that accelerometers located on top conveyor sections were attached on the surface beneath that in contact with moving flight and chain components. Microphone 5 was placed in the far-field to simulate what might be experienced by an operator, while the other four microphones were placed in the far-field at six inches from the surface of the system. Coherence techniques were used to look for relations between an accelerometer and microphone or a near-field and far-field microphone. As a result, a better understanding of the correlation between structural components, near-field sound pressure, and far-field sound pressure spectrums could be obtained, using the FRF and PCF methods.

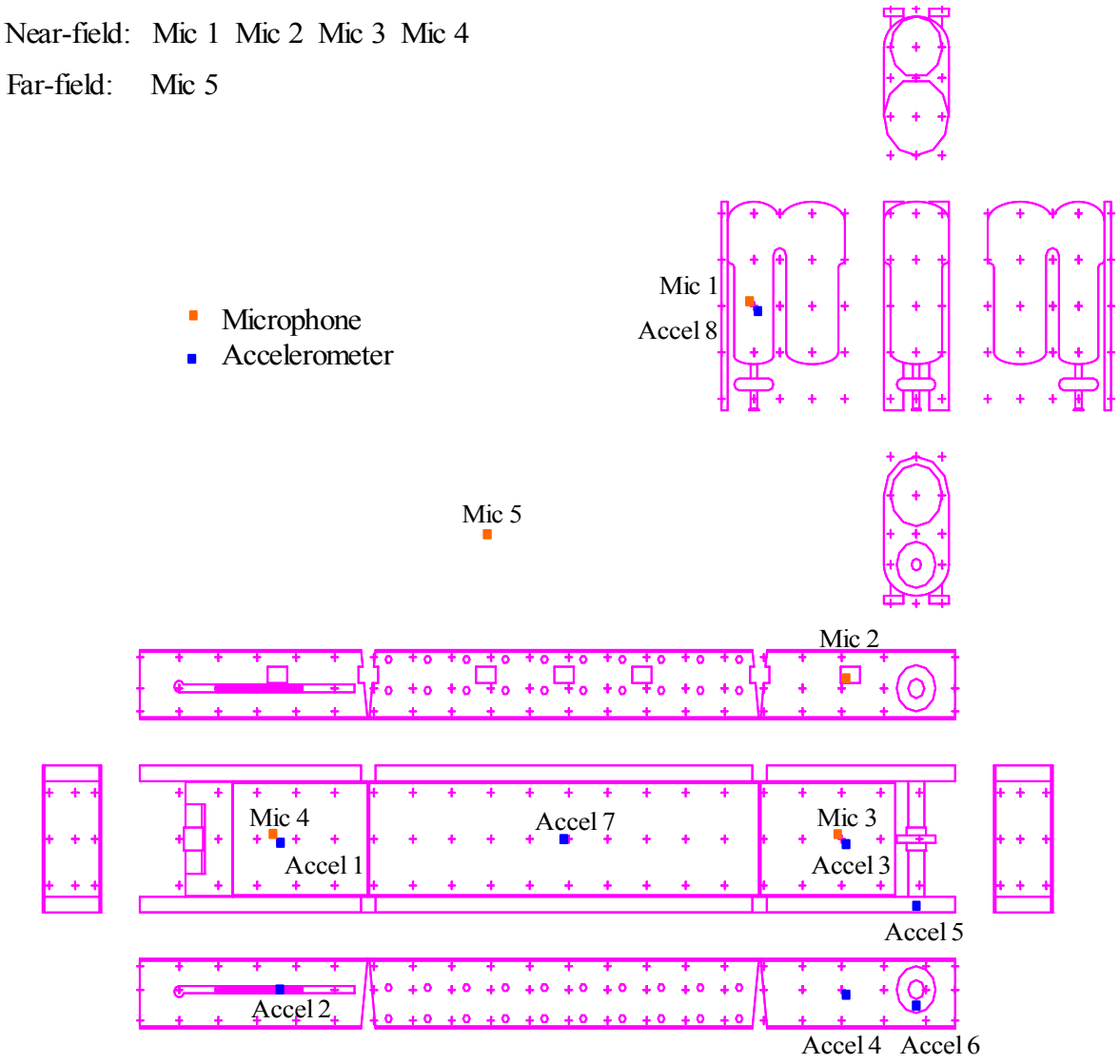

Figure 8 Coherent Power Measurement Configuration

3.5 Enhanced Time Measurements

Enhanced time measurements were taken with respect to repetitive flight-passing events at speeds 1 and 4. Time averaging was triggered by successive flights passing beneath an Omron E2K-C capacitive proximity sensor. System response data were recorded at both speeds with respect to flight cycle time using four accelerometers and three microphones of the same type as those used for coherent power measurements. Accelerometer and microphone measurement points are shown in Figure 9. Two sets of data were recorded for each of the measurement components: one with respect to the flight trigger located on the motor-end tail-section and the other located on the loading-end tail-section as shown in Figure 9. These signals were also averaged in both the time domain, with the use of flight triggering, and the frequency domain. Time-averaged and frequency-averaged data were plotted together versus frequency to identify the signal portion produced by cyclic driving mechanisms. The mechanisms were identified by plotting the time-averaged response over a time interval relative to component position. Note that the chain / conveyor motor test bed was located in an alternate environment for enhanced time data collection than for all other analyses, since NIOSH needed to clear space in the original location.

Sensors

- Microphone
- Accelerometer
- Proximity Sensor Flight Trigger Location 1 (PSFT 1)
- Proximity Sensor Flight Trigger Location 2 (PSFT 2)

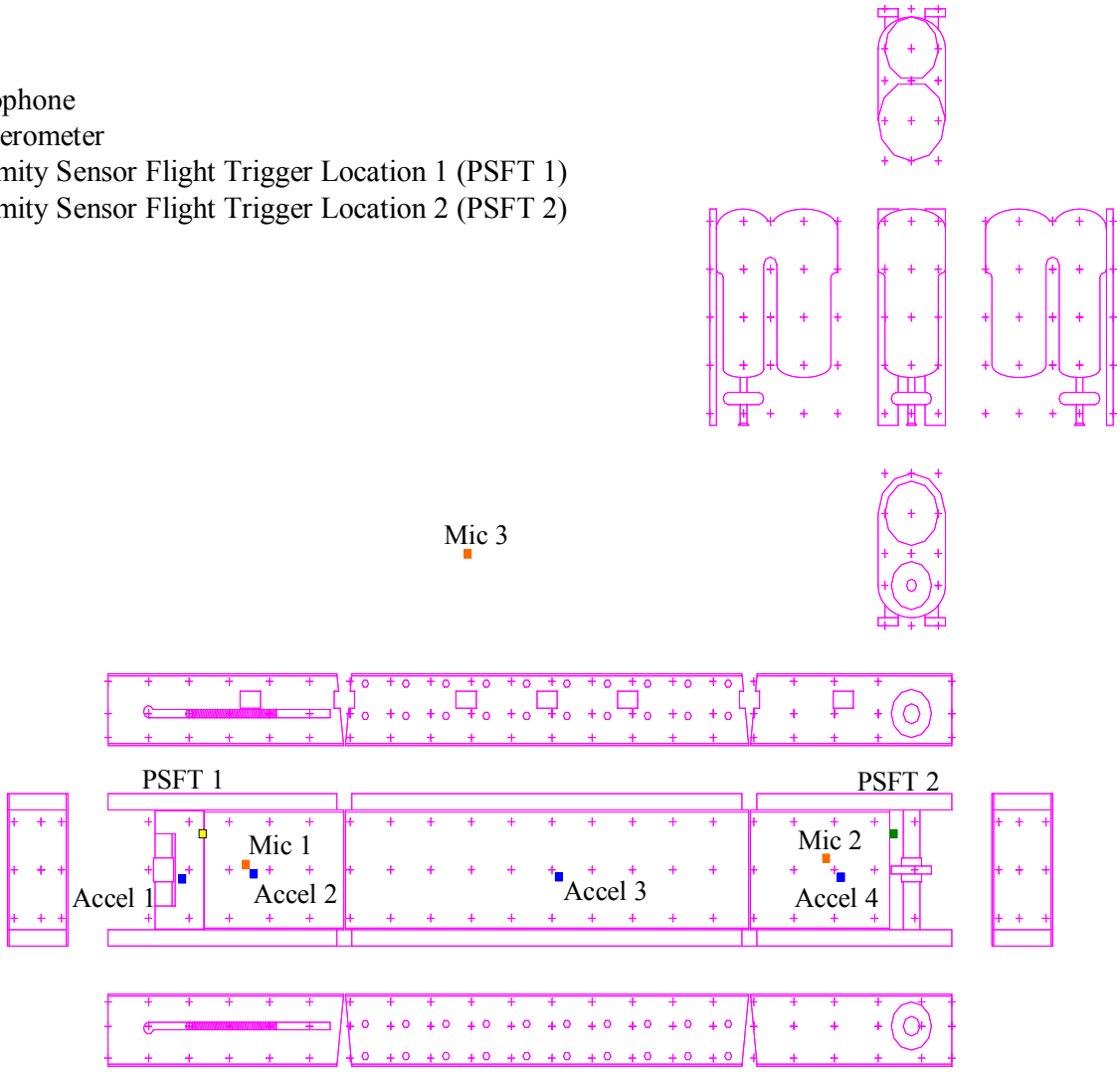

Figure 9 Enhanced Time Measurement Configuration

4.0 RESULTS AND DISCUSSION

The results of the five data measurement types: near-field sound pressure, sound intensity, tap testing, coherent power, and enhanced time measurements will be presented and discussed in this chapter.

4.1 Near-Field Sound Pressure

Near-field sound pressure level measurements were gleaned from the sound intensity data since a dual-microphone sound intensity probe was used. All logarithmic sound pressure values were determined using the standard reference pressure of 20e-6 Pa. Near-field sound pressure plots were produced for each measurement point at both conveyor speeds 1 and 4. These plots include broadband, 1/3-octave, and overall near-field sound pressure levels versus frequency. 1/3-octave and overall levels were determined by numerically integrating the sound pressure power spectral density functions with respect to frequency. Note that certain 1/3-octaves may contain no data. This is because the signal processing equipment used for analysis measures discrete frequency data, which may not included values within some 1/3-octave bands. Surface contour plots were then created at speeds 1 and 4 for 1/3-octave and overall levels in order to develop a graphical understanding of the sound pressure distribution along the surface of the system. Data for the contour plots were created using MATLAB's "meshgrid.m" and "griddata(…,'v4').m" scripts, which produced intermediate interpolated values between the measurement points. The plots were then produced using MATLAB's "contourf.m" script. Overall sound pressure level surface distributions over the 20-20,000 Hz frequency band for speeds 1 and 4 can be seen in Figures 10 and 11, respectively.

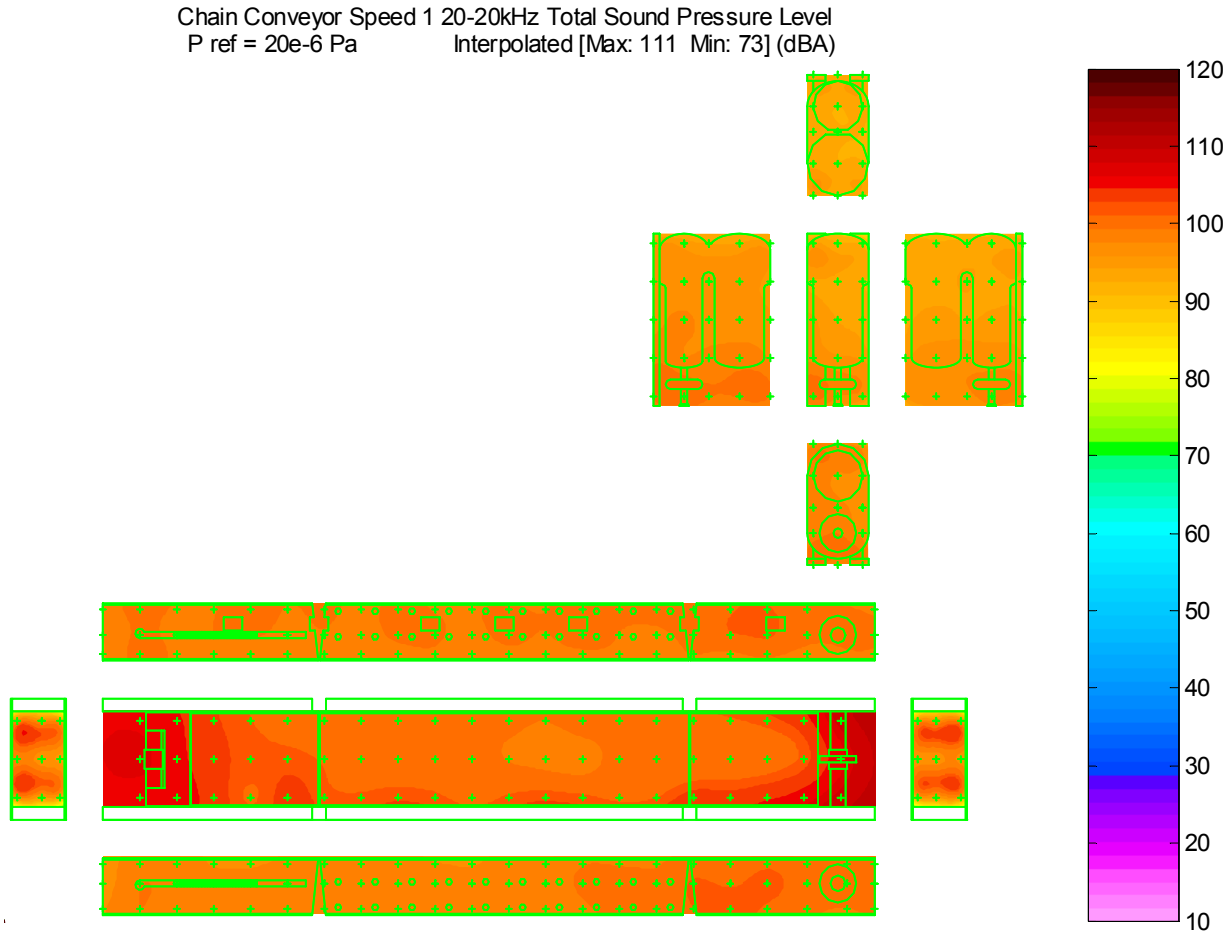

Figure 10 Speed 1 Overall Sound Pressure Level Surface Contour Plot

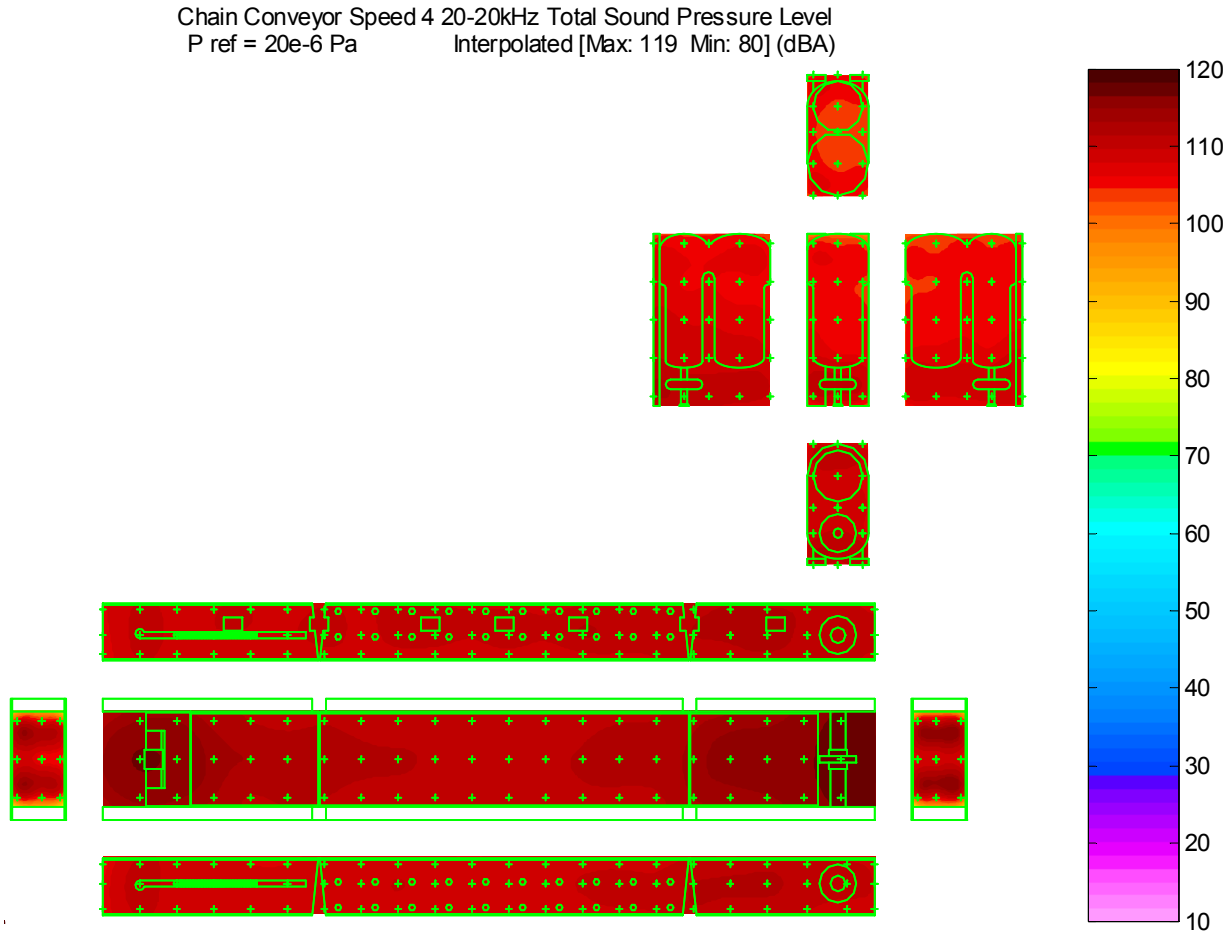

Figure 11 Speed 4 Overall Sound Pressure Level Surface Contour Plot

As expected the overall near-field sound pressure level distributions at speed 4 are greater, by approximately 10 dBA, than at speed 1. For the entire system at speed 1, the maximum "interpolated" overall near-field sound pressure level is 111 dBA and the maximum "measured" level is 108.7 dBA, which are located on the motor-end tail-section; the minimum "interpolated" overall near-field sound pressure level is 73 dBA and the minimum "measured" level is 92.6 dBA, which are located on the motor. The term "measured" refers to actual measured values obtained at the measurement points while the term "interpolated" refers to the inclusion of both measured values and MATLAB-produced intermediate values between the measurement points, which may or may not actually exist. Interpolation was performed on linear pressure quantities, rather than on logarithmic dB quantities. For the entire system at speed 4, the maximum interpolated overall near-field sound pressure level is 119 dBA and the maximum measured level is 118.3 dBA, which are also located on the motor-end tail-section; the minimum interpolated overall near-field sound pressure level is 80 dBA and the minimum measured level is 103.2 dBA, which also correspond with locations on the motor. The minimum interpolated values are suspect, since they are 20 dBA or more lower than any measured points.

The sound pressure level surface contour plots in Figures 10 and 11 reveal that the loading-end tail-section, spacer-plate section, and motor-end tail-section of the conveyor component are the areas of the system with the greatest overall near-field sound pressure levels at both speeds under test. The plots also show that the motor is a less significant sound pressure contributor, by approximately 8 dBA, when compared to the top surface of the conveyor component. The motor has a maximum measured overall near-field sound pressure level of 101.2 dBA for speed 1 and 112 dBA for speed 4, while the conveyor component has a level of 108.7 dBA for speed 1 and 118.3 dBA for speed 4. Figures 10 and 11 show that the openings on the right side of the conveyor component, marked by blue rectangles in Figure 4, produce near-field sound pressure levels that are somewhat higher, by approximately 3 dBA, than the closed surface areas. This suggests that a significant amount of sound pressure exists inside the conveyor component and should be contained or damped through treatments to reduce overall levels.

Maximum and minimum overall interpolated values discussed above are disclosed in the headings of Figures 10 and 11. A more detailed list of measured extremes for speeds 1 and 4 can be found in Tables 4 and 5, respectively. Note that the results for all thirteen sections of the system are given in the first thirteen rows of data in Tables 4 and 5, while the last two rows contain extreme results for the conveyor component (twelve conveyor sections) and the entire system (twelve conveyor sections and motor section / component). The most extreme sections (highest maximum values and lowest minimum values) are indicated in bold face type.

Table 4 Measured Sectional Maximum and Minimum Near-Field Sound Pressure Levels
Speed 1

Speed 1 Sound Pressure Level = (SPL) Pref = 20e-6 Pa	**Maximum**					
	1/3-octave			**Overall**		
	SPL (dBA)	1/3-octave (Hz)	Location	SPL (dBA)	Location	Rank
Loading-end Tail-section	**99.5**	**1250**	**G 3**	**104.3**	**G 3**	**3**
Motor-end Tail-section	**103.9**	**1250**	**F 20**	**108.7**	**F 20**	**1**
Main Section	96	2000	G 8	102.8	G 8	4
Spacer-plate Section	**101.8**	**1250**	**C 1**	**107.5**	**C 1**	**2**
Motor	97.5	2000	B 5	101.2	B 15	9
Loading-end Left Side-section	94	1250	A 25	100	K 25	11
Loading-end Right Side-section	95.2	1250	A 16	101	K 16	10
Main Left Side-section	94.2	2000	A 38	101.4	A 38	8
Main Right Side-section	95	1250	A 7	101.8	A 7	7
Motor-end Left Side-section	95.7	1250	K 41	102.6	K 41	5
Motor-end Right Side-section	95.4	1250	K 4	102.3	A 2	6
Front Side-section	92	1250	K 21	98.3	K 22	12
Rear Side-section	90.5	630	A 48	97.5	K 48	13
All Conveyor Sections	**103.9**	**1250**	**F 20**	**108.7**	**F 20**	
Entire System	**103.9**	**1250**	**F 20**	**108.7**	**F 20**	

	Minimum					
	1/3-octave			**Overall**		
	SPL (dBA)	1/3-octave (Hz)	Location	SPL (dBA)	Location	Rank
Loading-end Tail-section	22.8	25	G 5	101	F 5	12
Motor-end Tail-section	18.4	20	F 19	100.2	C 16	11
Main Section	13.6	20	G 13	99	C 13	8
Spacer-plate Section	23.2	20	G 2	105.3	F 2	13
Motor	**12.1**	**20**	**B 1**	**92.6**	**B 7**	**1**
Loading-end Left Side-section	17.1	20	K 28	96.6	A 24	4
Loading-end Right Side-section	15.2	20	J 17	97.8	J 20	5
Main Left Side-section	15.6	20	K 30	97.9	J 34	6
Main Right Side-section	12.1	20	J 5	98.2	J 13	7
Motor-end Left Side-section	12.1	20	A 44	100	K 44	10
Motor-end Right Side-section	12.8	20	A 49	99.4	J 1	9
Front Side-section	21.8	25	K 23	95.2	J 22	2
Rear Side-section	23.2	20	A 48	96	A 46	3
All Conveyor Sections	**12.1**	**20**	**A 44**	**95.2**	**J 22**	
Entire System	**12.1**	**20**	**A 44**	**92.6**	**B 7**	

Table 5 Measured Sectional Maximum and Minimum Near-Field Sound Pressure Levels
Speed 4

Speed 4 Sound Pressure Level = (SPL) Pref = 20e-6 Pa	**Maximum**					
	1/3-octave			**Overall**		
	SPL (dBA)	1/3-octave (Hz)	Location	SPL (dBA)	Location	Rank
Loading-end Tail-section	**107.4**	**1250**	**C 4**	**114.7**	**C 3**	**3**
Motor-end Tail-section	**111.8**	**1250**	**F 20**	**118.3**	**C 20**	**1**
Main Section	106.2	1600	C 14	113.3	C 15	5
Spacer-plate Section	**109.8**	**2000**	**C 1**	**117.3**	**C 1**	**2**
Motor	104.4	1250	B 2	112	B 15	8
Loading-end Left Side-section	102.5	1250	A 25	111.1	A 25	10
Loading-end Right Side-section	102.6	1250	A 17	110.6	A 19	11
Main Left Side-section	104.2	1250	A 38	111.3	A 38	9
Main Right Side-section	105.3	1250	A 7	112.3	A 7	7
Motor-end Left Side-section	105.4	1250	K 40	112.7	A 42	6
Motor-end Right Side-section	106.3	1250	A 2	113.9	A 2	4
Front Side-section	99.4	1250	K 23	107.4	K 22	13
Rear Side-section	100.8	630	A 48	108.5	A 48	12
All Conveyor Sections	**111.8**	**1250**	**F 20**	**118.3**	**C 20**	
Entire System	**111.8**	**1250**	**F 20**	**118.3**	**C 20**	

	Minimum					
	1/3-octave			**Overall**		
	SPL (dBA)	1/3-octave (Hz)	Location	SPL (dBA)	Location	Rank
Loading-end Tail-section	30.2	25	F 5	111.2	F 5	11
Motor-end Tail-section	31.9	25	G 19	113.6	F 16	12
Main Section	31.3	25	F 6	110.4	F 8	10
Spacer-plate Section	31.7	25	F 1	115	F 1	13
Motor	**24.6**	**25**	**B 1**	**103.2**	**B 2**	**1**
Loading-end Left Side-section	23.5	25	K 24	106.2	J 24	3
Loading-end Right Side-section	23	25	J 20	106.7	J 20	4
Main Left Side-section	26.1	25	K 33	108.1	J 34	6
Main Right Side-section	24.9	25	J 10	108.9	J 8	7
Motor-end Left Side-section	23.3	25	J 44	109.4	K 44	8
Motor-end Right Side-section	27.6	25	J 4	109.4	K 49	8
Front Side-section	27.6	25	J 21	105	J 21	2
Rear Side-section	38.2	25	K 48	107.3	K 47	5
All Conveyor Sections	**23**	**25**	**J 20**	**105**	**J 21**	
Entire System	**23**	**25**	**J 20**	**103.2**	**B 2**	

Tables 4 and 5 corroborate conclusions made from Figures 10 and 11 that the motor-end tail-section, the spacer-plate section, and the loading-end tail-section have the greatest overall near-field sound pressure levels for speeds 1 and 4. The motor-end tail-section is ranked 1st having a maximum measured overall near-field sound pressure level of 108.7 dBA for speed 1 at measurement point F20 and 118.3 dBA at measurement point C20 for speed 4. The spacer-plate section and the loading-end tail-section rank 2nd and 3rd, respectively. Recall that all measurement points can be located from Figure 6.

Sound pressure plots from measurement point F20 of the motor-end tail-section, can be seen in Figures 12 and 13. Figure 12 presents broadband near-field sound pressure levels in blue for speed 1 and black for speed 4. The integrated overall level is represented by the magenta and red lines for speeds 1 and 4, respectively. Integrated 1/3-octave levels for F20 are presented in Figure 13 with blue bars representing speed 1 and red for speed 4. Corresponding 1/3-octave and overall values for Figures 12 and 13 are given in Table 6. The peaks at 925, 1,300, 2,275, and 4,225 Hz are denoted in Figure 12. These are important frequencies relating to the motor-end tail-section only, which will recur as peak values throughout the analyses in this chapter.

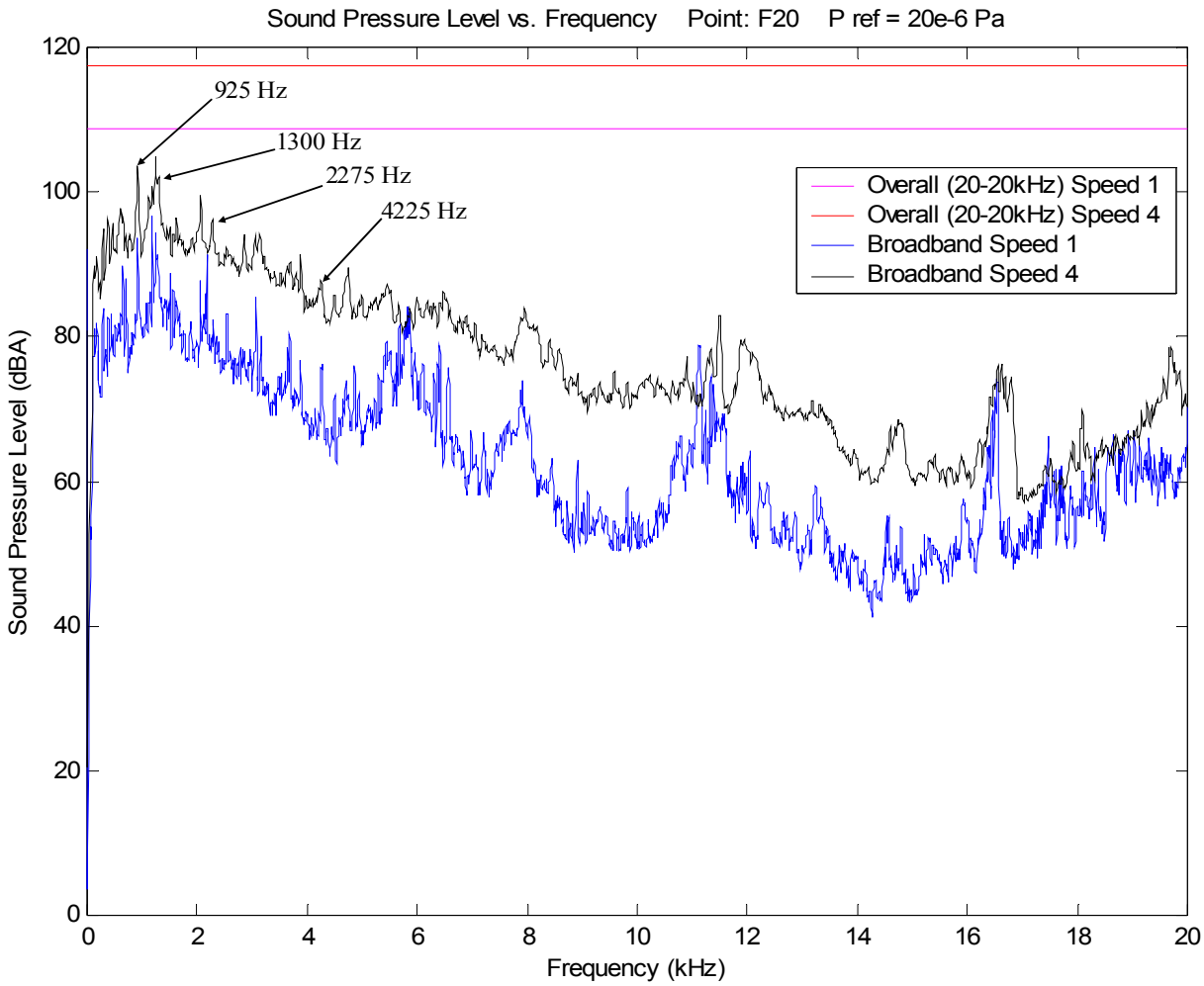

Figure 12 Measurement Point F20: Near-Field Sound Pressure Level (Broadband / Overall)

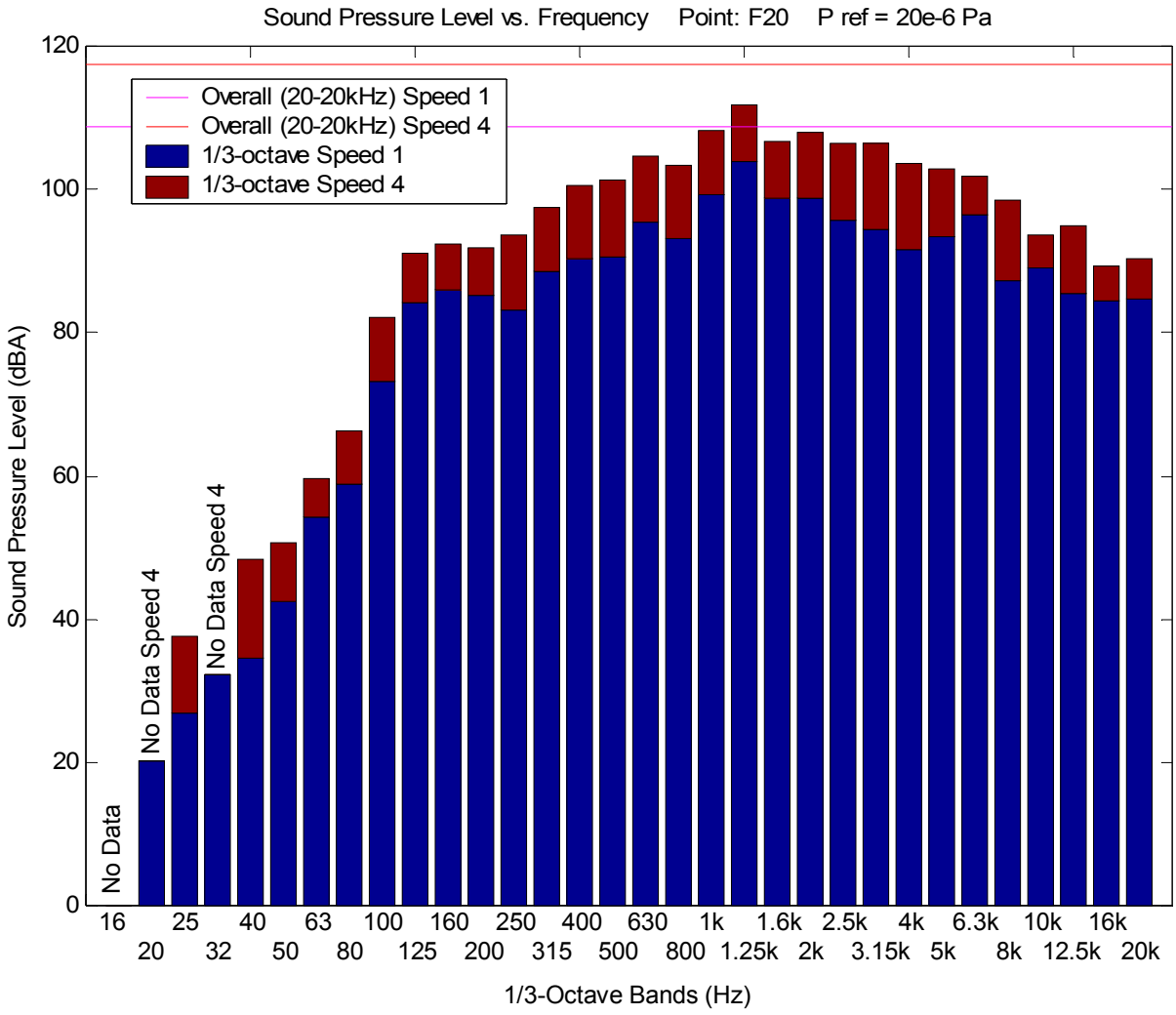

Figure 13 Measurement Point F20: Near-Field Sound Pressure Level (1/3-Octave / Overall)

Table 6 Measurement Point F20: 1/3-octave and Overall Near-Field Sound Pressure Levels

	SPL (dBA) Pref = 20e-6 Pa	
1/3-Octave (Hz)	Speed 1	Speed 4
16	No Data	No Data
20	20.2	No Data
25	26.9	37.7
32	32.3	No Data
40	34.6	48.4
50	42.4	50.5
63	54.1	59.7
80	58.7	66.2
100	73.2	82.2
125	84.1	91.1
160	85.9	92.3
200	85.3	92
250	83.2	93.5
315	88.5	97.6
400	90.3	100.5
500	90.6	101.4
630	95.4	104.5
800	93.2	103.4

	SPL (dBA) Pref = 20e-6 Pa	
1/3-Octave (Hz)	Speed 1	Speed 4
1000	99.2	108.2
1250	**103.9**	**111.8**
1600	98.8	106.6
2000	98.8	107.9
2500	95.7	106.4
3150	94.5	106.5
4000	91.7	103.5
5000	93.3	102.9
6300	96.4	101.8
8000	87.3	98.6
10000	88.9	93.6
12500	85.3	94.9
16000	84.3	89.3
20000	84.7	90.2
Overall (20-20,000 Hz)	108.7	117.6

Further, comparing near-field sound pressure versus frequency for measurement point F20 at speed 1 to speed 4, broadband, 1/3-octave, and overall levels all increase in magnitude with respect to speed. Also, the broadband peaks present at speed 1 in Figure 12 become less distinguished at speed 4 while some even disappear since the broadband noise levels increase. A few of these peaks change frequency. Some of the significant broadband peaks that were identified in Figure 12 occur at 925, 1,300, 2,275, and 4,225 Hz for speed 4, 925 and 1,300 Hz are also present at speed 1. Spectral distributions for other measurement points located on the motor-end tail-section are similar to those reported for measurement point F20.

From Figure 13, it is easy to see that the bulk of the A-weighted energy is from 500-5,000 Hz, where the most damage occurs to hearing. In order to further identify significant sound pressure levels and frequency ranges, 95 and 90 dBA will be used as reference levels. From Figures 12 and 13 and Table 6, measurement point F20 (motor-end tail-section) has near-

field sound pressure levels exceeding 95 dBA predominantly in the 630-2,500 Hz 1/3-octave range and exceeding 90 dBA from 400-6,300 Hz at speed 1. The 1,000-1,600 Hz band contains broadband near-field sound pressure levels greater than 90 dBA for this measurement point. Results regarding the spectral content of maximum measurement points located on the motor-end tail-section, the spacer-plate section, and the loading-end tail-section are summarized in Table 7. These indicate that the bandwidth of levels exceeding 90 dBA widens as the operating speed of the chain conveyor / motor system is increased, since the overall levels increase.

Table 7 Summary of Maximum Measured Sound Pressure Level Spectral Results

Motor-end Tail-section

	Measurement Point	1/3-octaves > 95 dBA	1/3-octaves > 90 dBA	1/3-octaves w/ Discrete Levels > 90 dBA
Speed 1	F20	630-2500 Hz	400-6300 Hz	1000-1600 Hz
Speed 4	C20	315-8000 Hz	125-20000 Hz	125-3150 Hz
	F20	315-8000 Hz	125-20000 Hz	160-3150 Hz

Spacer-plate Section

	Measurement Point	1/3-octaves > 95 dBA	1/3-octaves > 90 dBA	1/3-octaves w/ Discrete Levels > 90 dBA
Speed 1	C1	1000-3150 Hz	500-6300 Hz	1250 Hz, 3150 Hz
Speed 4	C1	0.4-20 kHz	0.125-20 kHz	500-3150 Hz

Loading-end Tail-section

	Measurement Point	1/3-octaves > 95 dBA	1/3-octaves > 90 dBA	1/3-octaves w/ Discrete Levels > 90 dBA
Speed 1	G3	1250 Hz	630-4000 Hz	1250 Hz
Speed 4	C3	315-5000 Hz	125-8000 Hz	315-3150 Hz
	C4	400-4000 Hz	125-8000 Hz	400-2000 Hz

Both maximum measured 1/3-octave near-field sound pressure levels for the motor-end tail-section and the entire system are located at measurement point F20 and have a 1/3-octave center frequency of 1,250 Hz. The 1,250 Hz 1/3-octave is within the most sensitive frequency band of the human ear, 1-3 kHz [35]. This frequency band requires the least amount of sound energy to reach damaging levels and thus can produce the largest hearing loss [35]. The surface contour plots for speeds 1 and 4 with 1/3-octave center frequency of 1,250 Hz can be seen in

Figures 14 and 15, respectively. As with the overall near-field sound pressure level contour plots, these figures show that the highest distributions for the 1,250 Hz 1/3-octave band are also at the tail-sections. Again supporting that sections located at the motor-end and loading-end represent the greatest near-field sound pressure levels. It is interesting to note that the 1,250 Hz 1/3-octave levels in these areas are approximately 5-6 dBA lower than corresponding overall levels, indicating that a significant amount of the energy is within this band.

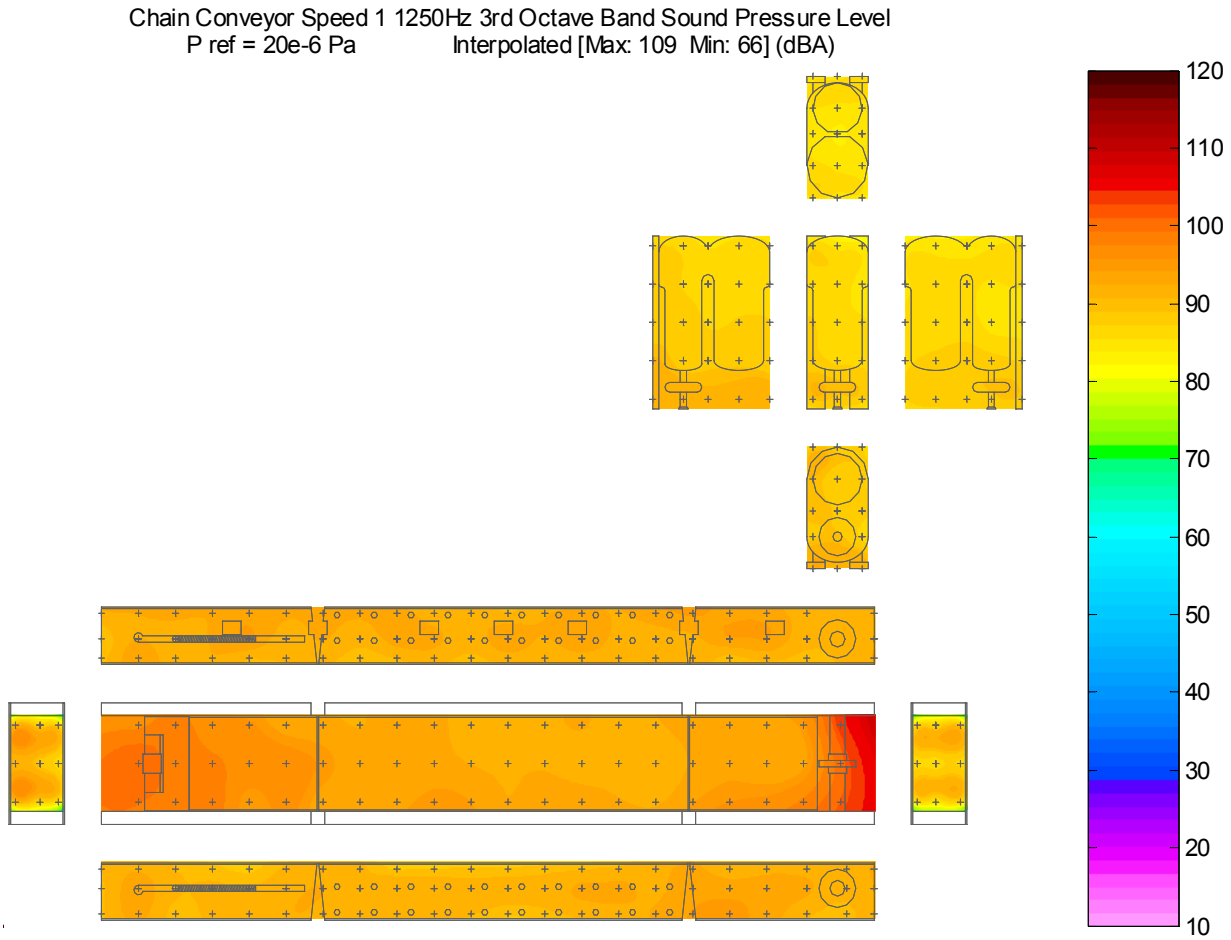

Figure 14 Speed 1 1,250 Hz 1/3-octave Sound Pressure Level Surface Contour Plot

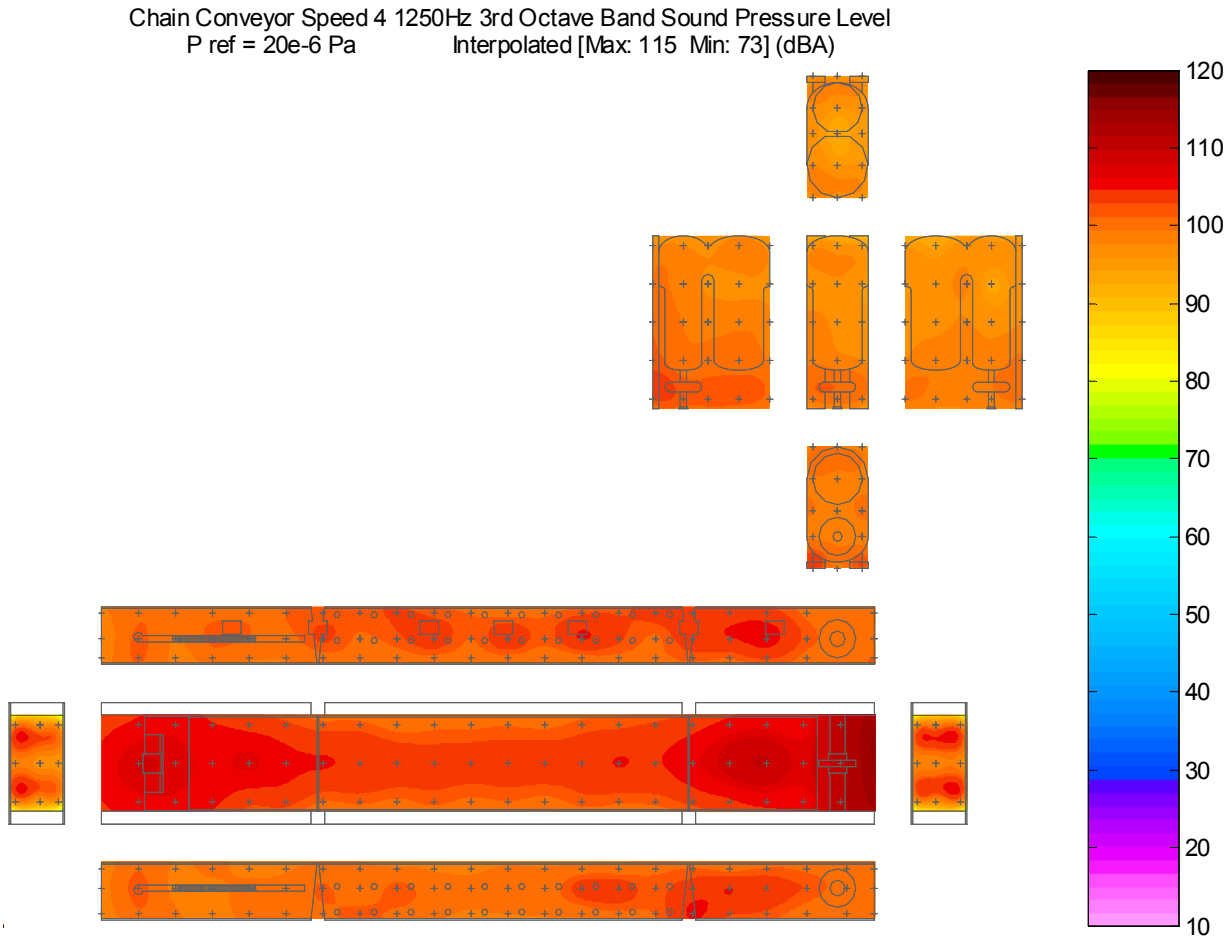

Figure 15 Speed 4 1,250 Hz 1/3-octave Sound Pressure Level Surface Contour Plot

4.2 Sound Intensity

Sound intensity measurements were taken normal to the chain conveyor / motor test bed surface at speeds 1 and 4 in order to determine the magnitude and gradients of sound intensity normal to the surface of the system. All logarithmic sound intensity values were determined using the standard reference intensity of 1e-12 W/m^2. Measurements were taken using a Brüel & Kjær 3519 sound intensity probe consisting of two ½" 4181 microphones and a 50 mm spacer. This configuration provided accurate sound intensity data over the 20-4,000 Hz range, which was determined by measuring the dynamic capability of the probe. Appendix A contains data plots for these measurements. Sound intensity plots covering the 20-4,000 Hz band were produced for each measurement point at both operating speeds 1 and 4. These plots include broadband, 1/3-octave, and overall sound intensity versus frequency. Again for the sound intensity analysis, certain 1/3-octaves may not contain data, for the same reasons described in the near-field sound pressure analysis. 1/3-octave and overall sound intensity was determined by numerically integrating the sound intensity power spectral density functions with respect to frequency. The data were also used to produce sound intensity color contour plots with gradient arrows, which were used to better understand normal sound intensity characteristics at the surface of the system. The color associated with a particular area of the conveyor represents the magnitude and orientation of the sound intensity normal to the surface of the test bed. Red (warm) colors represent sound intensity in the outward direction and blue (cool) shades represent inward intensity. Note that the arrows on the contour plots represent the magnitude and direction of the sound intensity gradient and not the actual sound intensity corresponding to the plane parallel to the surface of the test bed. MATLAB's "gradient.m" and "quiver.m" scripts were used to produce the gradient arrows on the contour plots. Overall sound intensity surface distributions over the 20-4,000 Hz frequency band for speeds 1 and 4 can be seen in Figures 16 and 17, respectively.

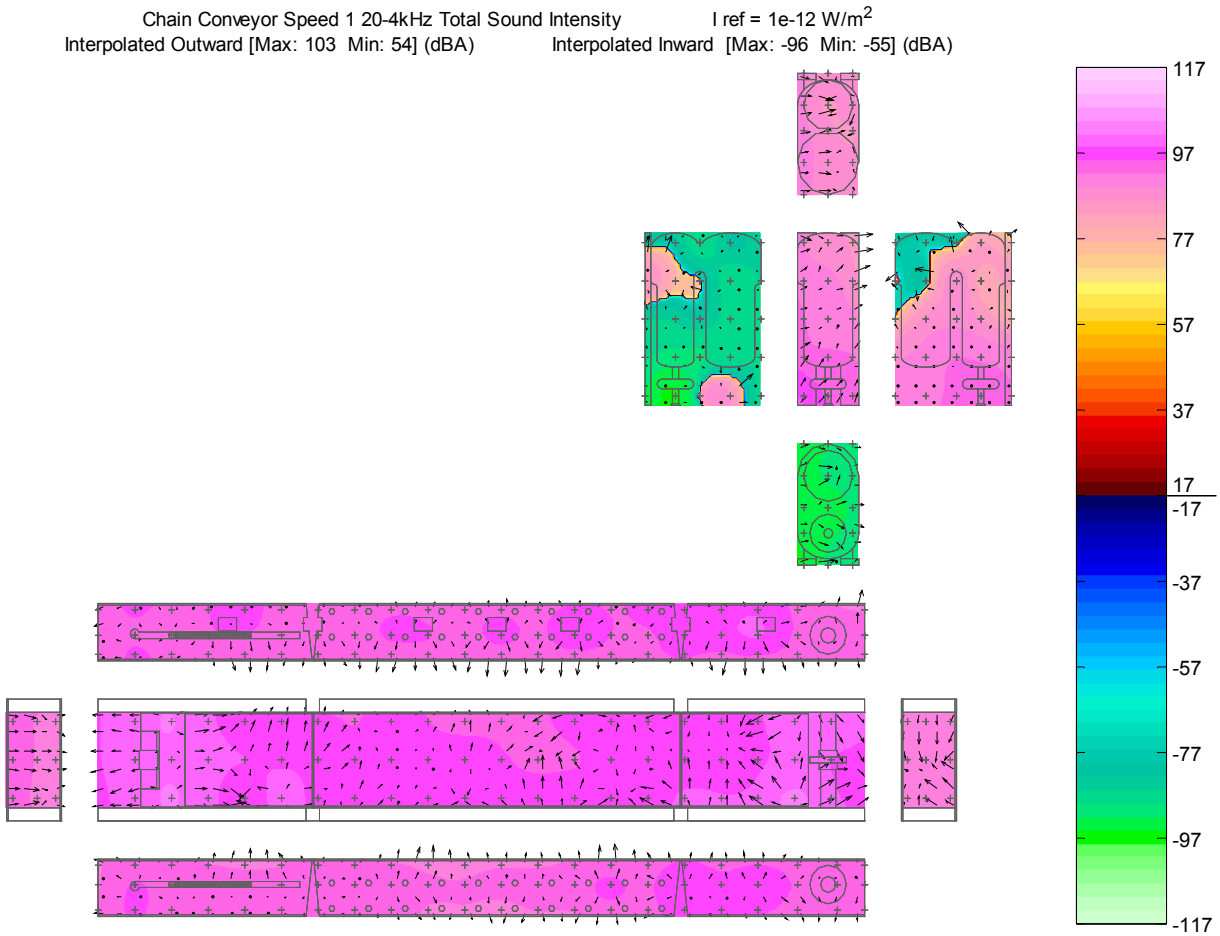

Figure 16 Speed 1 Overall Sound Intensity Surface Contour Plot and Gradient

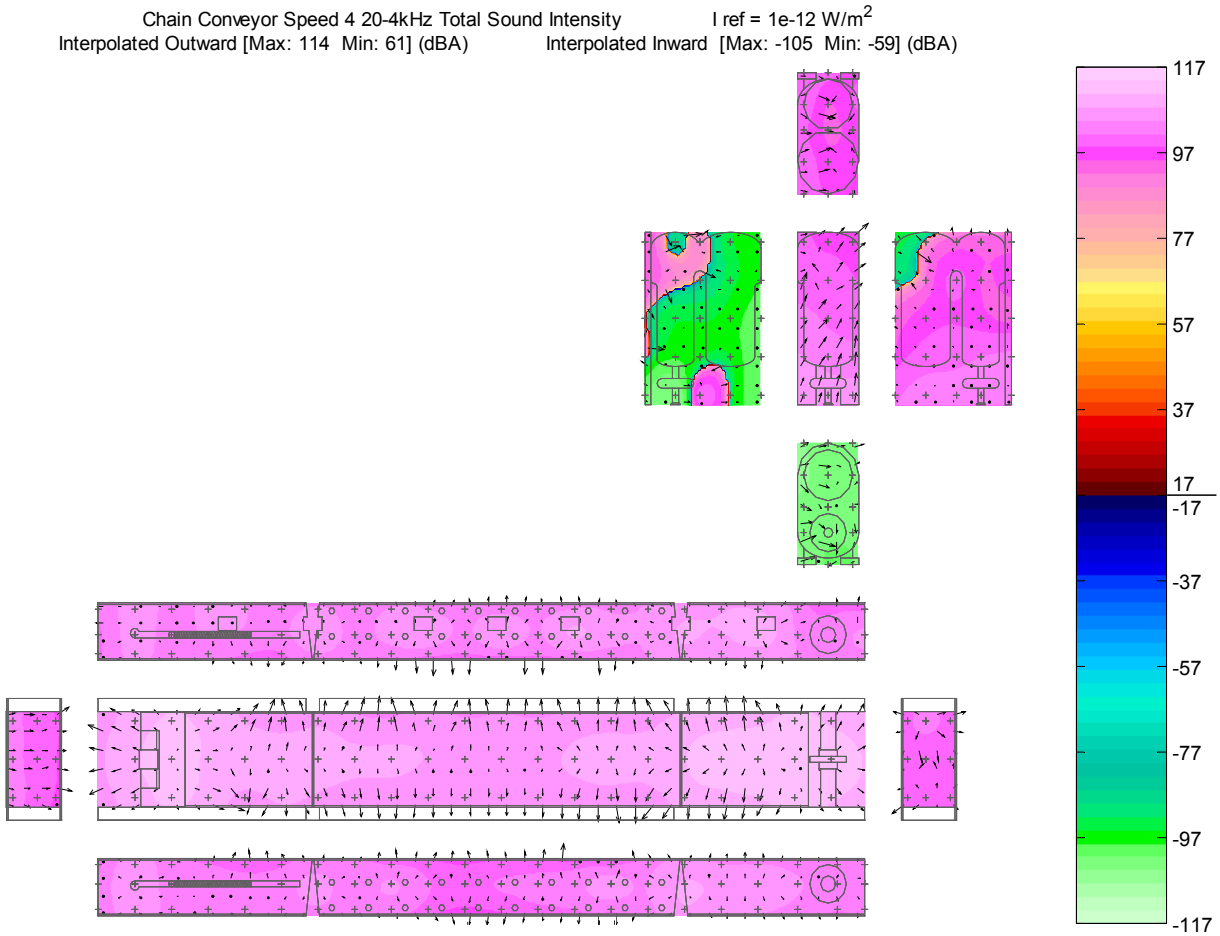

Figure 17 Speed 4 Overall Sound Intensity Surface Contour Plot and Gradient

As with near-field sound pressure, the overall outward sound intensity distributions are greater at speed 4. Extreme interpolated overall sound intensity values are listed in the headings of Figures 16 and 17. Measured overall outward sound intensity is 102.5 dBA and the minimum intensity is 70.7 dBA for speed 1. For speed 4, the maximum measured overall outward sound intensity is 113.7 dBA and the minimum measured overall outward sound intensity is 72.1 dBA. Maximum values for sound intensity are again located at the motor-end tail-section, while minimum values are at the motor. Sound intensity levels were approximately 5 dBA less than near-field sound pressure levels due to the presence of reactive components in the near-field.

The magnitude and orientation of the contour plots in Figures 16 and 17 used with the gradient arrows allowed for the identification of dominant noise sources. The results showed that the conveyor produces high levels of outward sound intensity over the entire surface. The levels produced by the conveyor are greater than those produced by the motor by approximately 4 dBA for speed 1 and 7 dBA at speed 4. The overall sound intensity plots also verify that the loading-end tail-section, spacer-plate section, and motor-end tail-section are the truly dominant noise sources. This corresponds with conclusions drawn from the near-field sound pressure analysis. Conveyor component discontinuities, located where the tail-sections meet the main section, provide concentrations of slightly increased outward sound intensity. Also, sound intensity at the openings on the right side of the conveyor component, marked by blue rectangles in Figure 4, are noticeably higher, by approximately 4 dBA, than the closed surface areas. This reinforces the conclusion drawn from the near-field sound pressure analysis that a significant amount of sound power exists inside the conveyor component and should be contained or damped through treatments to reduce overall levels.

It is interesting to note that, like the outward sound intensity, the overall inward sound intensity distributions are also greater at speed 4 than at speed 1. This can be determined by observing the overall inward sound intensity data summarized in Table 8. The smaller motor component, identified in Figure 4, has inward and outward sound intensity while the larger conveyor component consists mainly of outward sound intensity of greater magnitude. This phenomenon provides that the conveyor component has a much greater contribution to the entire system's sound power than the motor component. Figures 16 and 17 provide that the left and

front sides of the motor component consist mainly of inward sound intensity. The sides of the system can be identified by the legend in Figure 4. The presence of inward sound intensity on the left side of the motor is due to the dominating sound power flow from the conveyor component of the system towards this face of the motor. The left side of the motor is parallel to the right side of the conveyor with opposite orientation. Since the net sound intensity between these oppositely oriented faces provides that sound flows from the conveyor towards the motor it was again concluded that the conveyor is the dominant system sound source. The front side of the motor component is orthogonal to the right side and located at the rear of the conveyor component. The presence of inward sound intensity on the front face of the motor is also due to the dominating sound power flow from the conveyor component of the system.

Table 8 Maximum / Minimum Measured and Interpolated Inward Sound Intensity Data

Inward Sound Intensity = (SI in) I ref = 1e-12 W/m^2	Maximum SI in (dBA)		Minimum SI in (dBA)	
	Interpolated	Measured	Interpolated	Measured
Speed 1	-96	-95.7	-55	-75
Speed 4	-105	-104.4	-59	-74.9

Maximum and minimum measured extremes for speeds 1 and 4 can be found in Tables 9 and 10, respectively. Note that the results for all thirteen sections of the system are given in the first thirteen rows of data in Tables 9 and 10, while the last two rows contain extreme results for the conveyor component (twelve conveyor sections) and the entire system (twelve conveyor sections and motor section / component). The most extreme sections are indicated in bold face type.

Table 9 Speed 1 Measured Sectional Maximum and Minimum Outward Sound Intensity Levels

Speed 1 Outward Sound Intensity = (SI out) Iref = 1e-12 W/m^2	**Maximum**					
	1/3-octave			**Overall**		
	SI out (dBA)	1/3-octave (Hz)	Location	SI out (dBA)	Location	Rank
Loading-end Tail-section	**95.6**	**1600**	**G 5**	**100.2**	**C 3**	**3**
Motor-end Tail-section	**95.6**	**1250**	**G 19**	**102.5**	**G 19**	**1**
Main Section	92.6	1600	C 9	98.3	G 6	7
Spacer-plate Section	**96.9**	**1250**	**F 2**	**102.2**	**G 2**	**2**
Motor	95.3	2000	B 5	98.5	B 5	6
Loading-end Left Side-section	91.6	1250	A 25	96.4	K 25	11
Loading-end Right Side-section	92.5	1250	A 16	96.8	K 16	10
Main Left Side-section	90.9	1250	A 38	97	A 38	9
Main Right Side-section	92.6	1250	A 7	98.1	A 7	8
Motor-end Left Side-section	92.6	1250	K 40	98.6	A 40	5
Motor-end Right Side-section	93.1	1250	A 2	99.2	A 2	4
Front Side-section	89.9	1250	K 21	94.8	K 21	12
Rear Side-section	86.6	630	J 48	91.6	K 48	13
All Conveyor Sections	**96.9**	**1250**	**F 2**	**102.5**	**G 19**	
Entire System	**96.9**	**1250**	**F 2**	**102.5**	**G 19**	

	Minimum					
	1/3-octave			**Overall**		
	SI out (dBA)	1/3-octave (Hz)	Location	SI out (dBA)	Location	Rank
Loading-end Tail-section	19.7	20	F 3	96.7	F 5	11
Motor-end Tail-section	18	20	F 20	97.3	C 16	12
Main Section	17.1	20	G 15	95	C 12	10
Spacer-plate Section	26.8	25	G 2	100.4	G 1	13
Motor	**17.1**	**20**	**B 6**	**70.7**	**B 12**	**1**
Loading-end Left Side-section	17.2	25	K 27	90.9	J 24	5
Loading-end Right Side-section	17.8	20	J 19	91.6	J 20	7
Main Left Side-section	17.2	20	J 32	90.3	J 33	4
Main Right Side-section	17.3	25	J 12	92.7	J 10	8
Motor-end Left Side-section	17.5	20	A 40	92.9	K 44	9
Motor-end Right Side-section	17.2	20	J 3	91.4	K 49	6
Front Side-section	18.2	25	K 21	90.1	J 22	3
Rear Side-section	21	20	K 46	89.3	A 47	2
All Conveyor Sections	**17.1**	**20**	**G 15**	**89.3**	**A 47**	
Entire System	**17.1**	**20**	**G 15**	**70.7**	**B 12**	

Table 10 Speed 4 Measured Sectional Maximum and Minimum Outward Sound Intensity Levels

Speed 4 Outward Sound Intensity = (SI out) Iref = 1e-12 W/m^2	**Maximum**					
	1/3-octave			**Overall**		
	SI out (dBA)	1/3-octave (Hz)	Location	SI out (dBA)	Location	Rank
Loading-end Tail-section	**104.8**	**1600**	**C 5**	**110.7**	**C 3**	**3**
Motor-end Tail-section	**107.7**	**1600**	**C 18**	**113.7**	**C 18**	**1**
Main Section	104.1	1600	C 14	109.3	C 15	5
Spacer-plate Section	**104.9**	**1600**	**C 2**	**111.9**	**C 2**	**2**
Motor	99.6	630	B 7	107	B 5	8
Loading-end Left Side-section	99	1250	A 25	106.8	A 25	9
Loading-end Right Side-section	99.1	1250	A 17	105.9	K 19	11
Main Left Side-section	100.3	1250	A 38	106.5	A 38	10
Main Right Side-section	102.7	1250	A 7	108.4	A 7	6
Motor-end Left Side-section	102.7	1250	K 40	108.2	A 40	7
Motor-end Right Side-section	104	1250	A 2	109.9	A 2	4
Front Side-section	96.3	1250	K 23	103.3	K 21	12
Rear Side-section	97	630	A 48	102.7	A 48	13
All Conveyor Sections	**107.7**	**1600**	**C 18**	**113.7**	**C 18**	
Entire System	**107.7**	**1600**	**C 18**	**113.7**	**C 18**	

	Minimum					
	1/3-octave			**Overall**		
	SI out (dBA)	1/3-octave (Hz)	Location	SI out (dBA)	Location	Rank
Loading-end Tail-section	18.4	25	C 5	106.4	F 5	11
Motor-end Tail-section	25.7	25	G 17	109.2	F 16	12
Main Section	18.3	25	G 13	105.4	F 10	10
Spacer-plate Section	18.2	25	F 2	109.5	F 1	13
Motor	**17.6**	**50**	**B 6**	**72.1**	**B 13**	**1**
Loading-end Left Side-section	19.4	40	J 24	100.2	J 28	5
Loading-end Right Side-section	19.7	63	A 19	100.5	J 20	6
Main Left Side-section	17.4	63	J 39	98.2	K 34	2
Main Right Side-section	17	25	K 14	101.7	J 10	7
Motor-end Left Side-section	17.9	25	J 44	102.2	K 44	9
Motor-end Right Side-section	23.1	40	J 1	101.8	K 49	8
Front Side-section	20.8	25	J 21	98.9	J 23	3
Rear Side-section	35.5	25	K 47	99.1	A 47	4
All Conveyor Sections	**17**	**25**	**K 14**	**98.2**	**K 34**	
Entire System	**17**	**25**	**K 14**	**72.1**	**B 13**	

Tables 9 and 10 also show that the motor-end tail-section has the greatest overall outward sound intensity followed by the spacer-plate section and loading-end tail-section, respectively. The motor-end tail-section has a maximum measured overall outward sound intensity of 102.5 dBA for speed 1 at measurement point G19 and 113.7 dBA at measurement point C18 for speed 4. The first three ranked sections for maximum overall outward sound intensity correspond with results from the near-field sound pressure analysis.

Sound intensity plots from measurement point G19 of the motor-end tail-section, can be seen in Figures 18 and 19. Figure 18 presents broadband sound intensity levels in blue for speed 1 and black for speed 4. The integrated overall level is represented by the magenta line for speed 1 and the red line for speed 4. Note that intensity is positive at all frequencies except at approximately 3,300 Hz. Integrated 1/3-octave levels for G19 are presented in Figure 19 with blue bars representing speed 1 and red for speed 4. Corresponding 1/3-octave and overall values for Figures 18 and 19 are given in Table 11. Figure 18 denotes recurring peaks at 925, 1,300, and 2,275 Hz for speed 4 and 925 Hz also at speed 1. These frequencies were more distinct in the near-field sound pressure analysis, but will recur as peak values for the motor-end tail-section in later analyses.

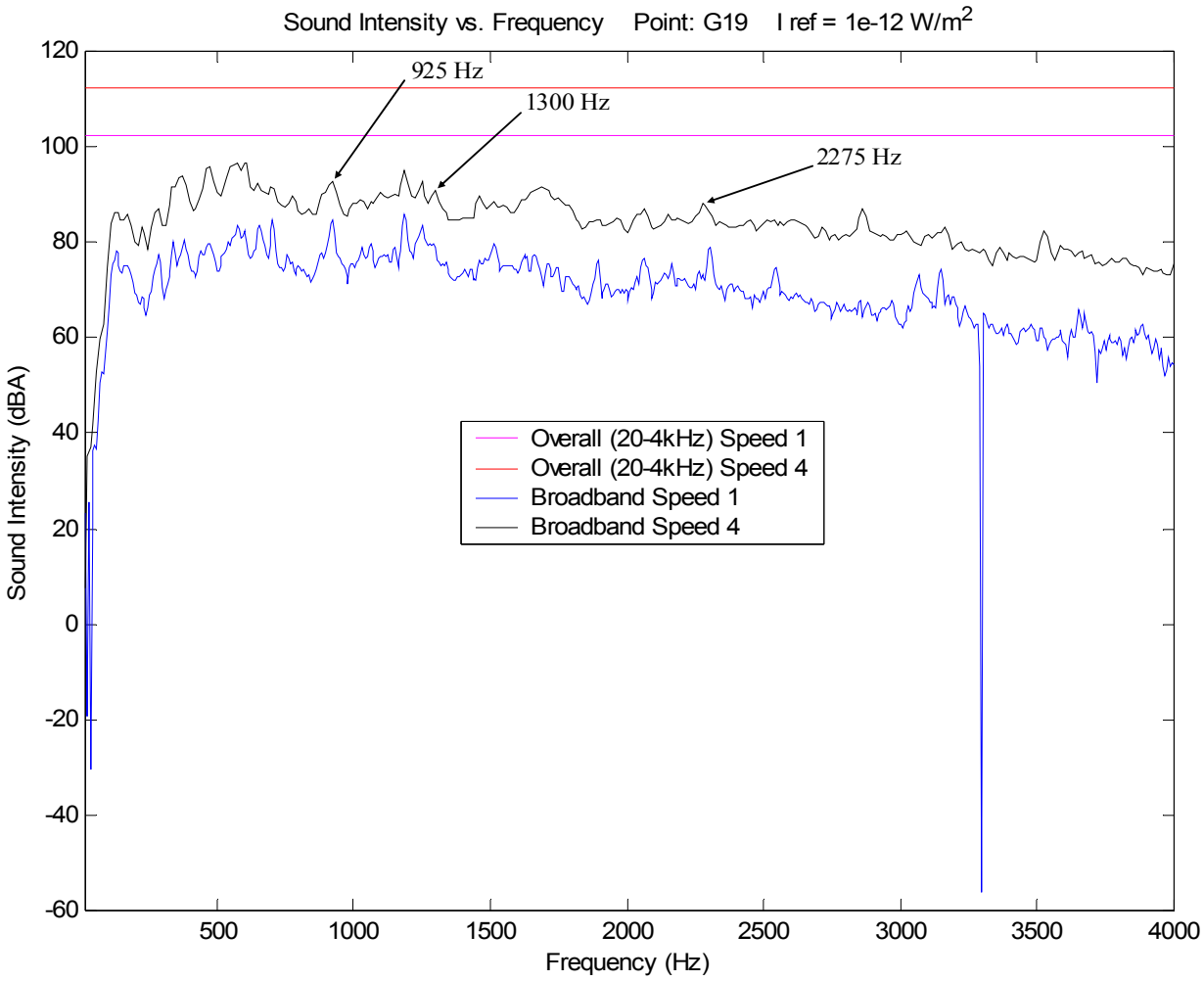

Figure 18 Measurement Point G19: Sound Intensity (Broadband / Overall)

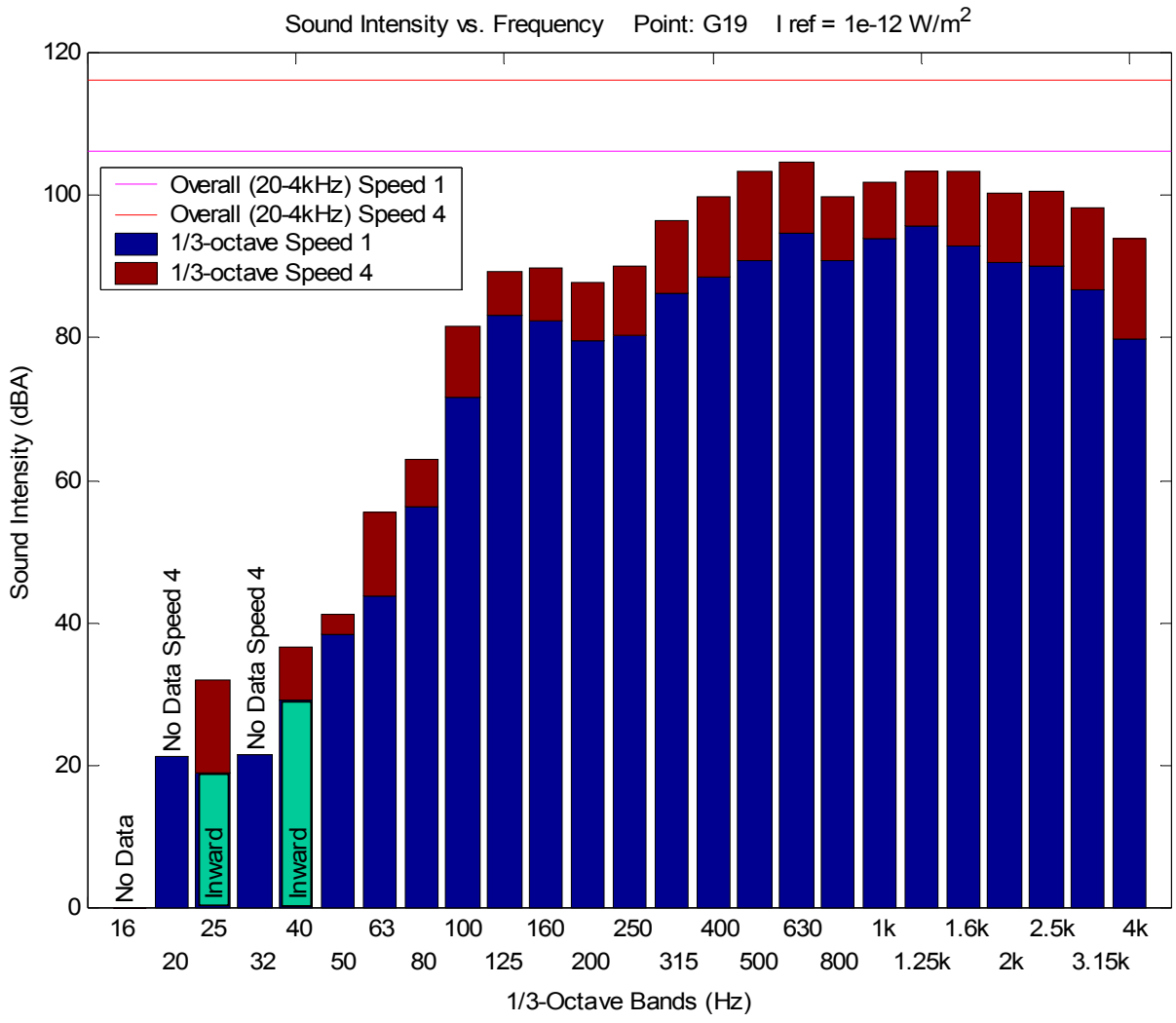

Figure 19 Measurement Point G19: Sound Intensity (1/3-Octave / Overall)

Table 11 Measurement Point G19: 1/3-Octave and Overall Sound Intensity Levels

	SI (dBA) I ref = 1e-12 W/m^2	
1/3-Octave (Hz)	Speed 1	Speed 4
16	No Data	No Data
20	21.3	No Data
25	-18.9	32
32	21.6	No Data
40	-29.2	36.5
50	38.4	41.2
63	43.7	55.4
80	56.3	63
100	71.8	81.7
125	83.2	89.4
160	82.5	89.9
200	79.7	87.8
250	80.3	90
315	86.2	96.4

	SI (dBA) I ref = 1e-12 W/m^2	
1/3-Octave (Hz)	Speed 1	Speed 4
400	88.5	99.7
500	90.9	103.3
630	94.7	104.5
800	90.8	99.7
1000	93.8	101.9
1250	95.6	103.4
1600	93	103.4
2000	90.5	100.3
2500	90.1	100.6
3150	86.7	98.4
4000	79.7	93.9
Overall (20-4,000 Hz)	102.5	112.2

The maximum measured 1/3-octave outward sound intensity for the entire system is located at measurement point F2 (spacer-plate section) and has a 1/3-octave center frequency of 1,250 Hz for speed 1. For speed 4 the 1,600 Hz 1/3-octave band dominates the system at measurement point C18 (motor-end tail-section). The surface contour plots for the 1,250 Hz 1/3-octave at speed 1 and the 1,600 Hz 1/3-octave at speed 4 can be seen in Figures 20 and 21, respectively. These plots show again that the highest distributions are located at the tail-sections for these 1/3-octave bands. As with near-field sound pressure, the 1,250 and 1,600 Hz 1/3-octave levels in these areas are approximately 5-6 dBA lower than corresponding overall levels, indicating that a significant amount of the systems sound power is produced within these frequency bands.

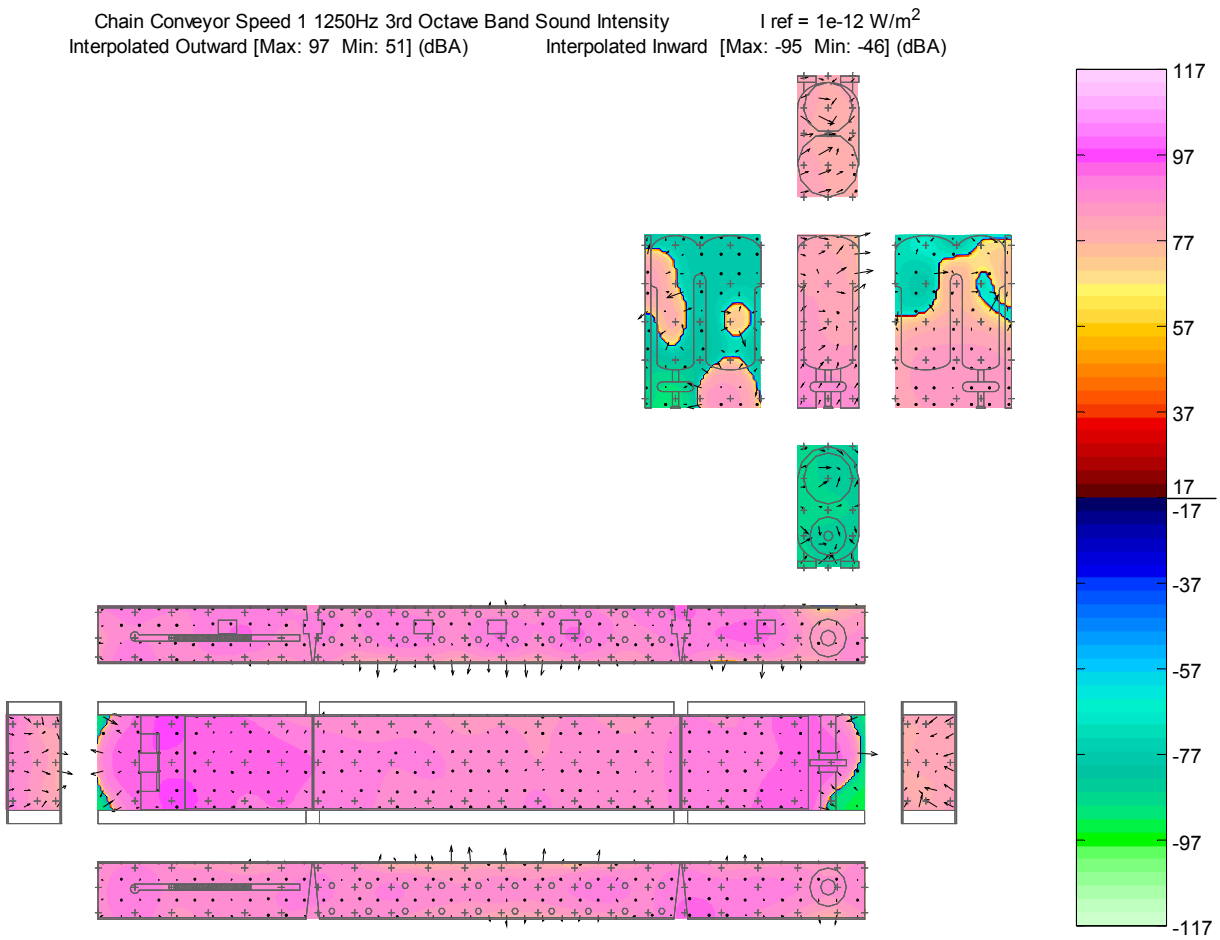

Figure 20 Speed 1 1,250 Hz 1/3-octave Sound Intensity Surface Contour Plot

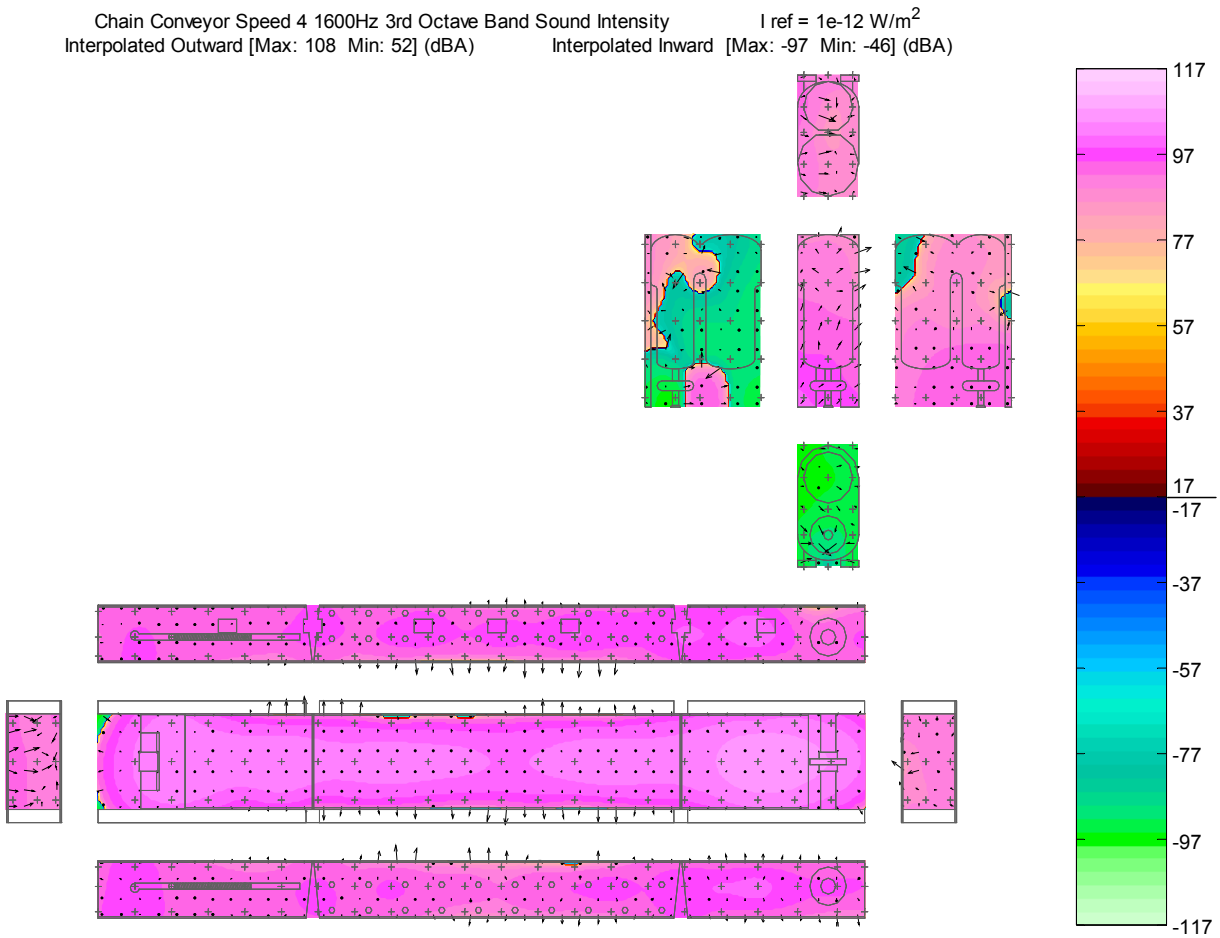

Figure 21 Speed 4 1,600 Hz 1/3-octave Sound Intensity Surface Contour Plot

4.3 Tap Tests

Tap tests were performed on various sections of the chain conveyor component in order to identify structural resonances that may be responsible for sound radiation. The high modal density of the structures made curve-fitting transfer functions to identify natural frequencies and damping ratios prohibitive. Instead, magnitude and phase of the transfer function data were plotted along side conditioned near-field sound pressure levels so that common frequency peaks could be identified. Near-field sound pressure levels were conditioned for the analysis by first cubing and then normalizing the values in order to amplify spectral peaks. The analysis covers the 20-8,000 Hz frequency band which was divided into 1 kHz wide zoomed spectrums.

The various tap test input output configurations and their data files were given in Figure 7. Transfer function magnitude and phase plots with proximal conditioned near-field sound pressure levels at speeds 1 and 4 were created for each tap test output accelerometer. After the plots for each tap test output accelerometer and proximal conditioned near-field sound pressure readings were created, vertical lines were placed on the plots at frequencies where peak pressure corresponds with a structural mode. Structural modes were identified at peak transfer function magnitudes corresponding with a 180 degree phase shift.

The sections of interest for the tap test analysis are the motor-end tail-section (C), spacer-plate section (G), and loading-end tail-section (B) due to the fact that these sections have the three greatest measured overall near-field sound pressure and sound intensity levels. Proximal accelerometer / sound pressure measurement point(s) for the three sections of interest can be found in Table 12. A vertical line is drawn where peaks in the structural and acoustic responses match frequency as in Figure 22. This figure indicates that there is potentially a structural-acoustic relation at 925 Hz for the motor-end tail-section. The figure shows peaks at 925 Hz for accelerometers 1, 5, and 6 and sound pressure measurement point G20 at speed 1 and points F20, C20, and G20 at speed 4. The results of frequency, accelerometer, and near-field sound pressure level measurement point(s) for speeds 1 and 4 for the motor-end tail-section can be found in Table 13.

Table 12 Proximal Accelerometer locations to Sound Pressure Level Measurement Points

	Sound Pressure Measurement Points (see Figure 5)		
Accelerometer (see Figure 6)	Motor-end Tail-section	Spacer-plate Section	Loading-end Tail-section
1	C16 C17 G16 G17	F1 F2	F3
2	G17	C2 F2	C3 C4 F3 F4
3	C17 C18 G17 G18	C2	C4
4	C18	C1 C2 G1 G2	C4 C5 G4 G5
5	C18 C19 F18 F19	G2	G5
6	F19	G1 G2	C5 F5

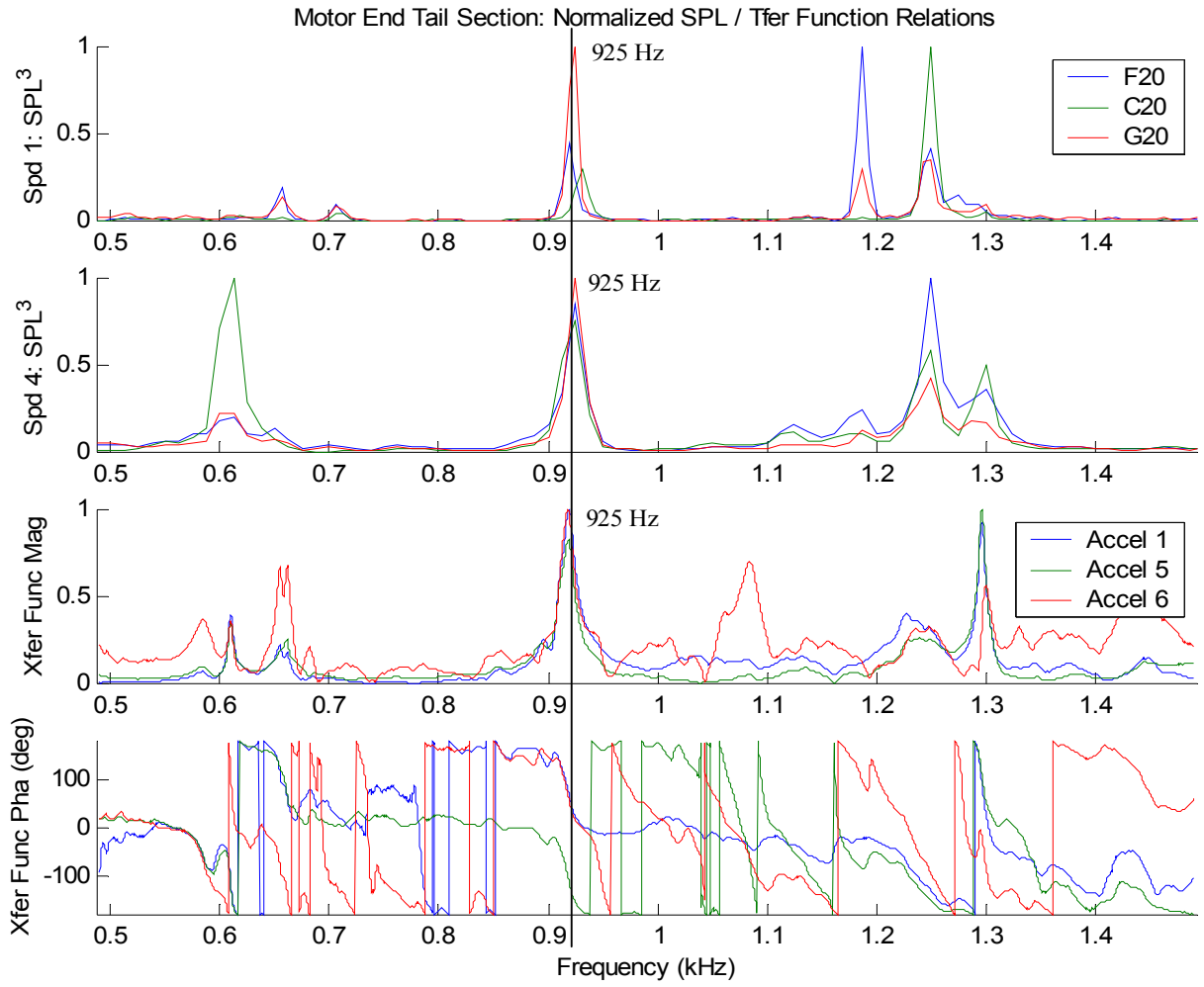

Figure 22 Motor-end Tail-section: Tap Test / Conditioned Sound Pressure Level (500-1,500 Hz)

Table 13 Motor-end Tail-section: Locations of Coincident Structural and Acoustic Frequencies

Speed 1

Frequency (Hz)	SPL Measurement Points (see Figure 3)	Accelerometers (see Figure 4)
610	C16	1
925	**C17 G17 C19 G20**	**1 5 6**
1300	**C17 C18 C19 G16**	**1 2 3 4 5**
2275	**C18**	**4**
3150	C18 F19 G17	1 5
3510	C16 C18	1 3 4 5
4225	**G17 F19**	**1 3 6**
9180	G16	1
10630	C18	4

Speed 4

Frequency (Hz)	SPL Measurement Points (see Figure 3)	Accelerometers (see Figure 4)
610	C16 G16 G17 G18	1 3
925	**C16 C20 F20 G20**	**1 5 6**
1300	**C16 C17 C18 C19 F18 G16 G17**	**1 2 3 4 5**
1610	G16	1
2275	**C18**	**4**
3150	C16 C17	1
3510	C18 C19 F18 F19 G16	1 3 4 5
4225	**C16 C17 C18 C19 F18 F19 G16 G17 G18**	**1 3 5 6**
5000	C17 C19 F19 G17 G18	2 3 5 6
6700	C18	4
7610	C16 C17	1
9180	G16 G17	1 2
10630	C18	4

Results provide that all three sections, motor-end tail-section, spacer-plate section, and loading-end tail-section, have coincident resonant frequencies at which relations between sound pressure and structural resonance recur for the various measured points. Certain frequencies that were slightly present at speed 1 seem to be magnified at speed 4 to meet the level of frequencies with consistently greater presence at speeds 1 and 4. This phenomenon is consistent with that of significant broadband sound pressure level diminishment from speed 1 to speed 4. The numbers of sound pressure / structural resonance correlated frequencies increase for the motor-end tail-section and the spacer-plate section from speed 1 to speed 4, while the loading-end tail-section

does not follow this trend. For the motor-end tail-section and the spacer-plate section many of these frequencies stay the same while new values arise from speed 1 to speed 4, which would suggest a radiating structural mode. The same phenomena are observed for the loading-end tail-section, but some of the frequencies disappear from speed 1 to speed 4. Significant broadband peaks at 925, 1,300, 2,275, and 4,225 Hz were identified on the motor-end tail section for speeds 1 and 4. These frequencies and their corresponding measurement points are identified in Table 13 with bold face type, and are consistent with near-field sound pressure and sound intensity results. The tap test analysis performed on these three sections identified many coincident structural acoustic frequencies and it is very likely that many are due to structural radiation. This in fact supports the idea that the system would benefit from passive damping treatments applied to the conveyor panels.

4.4 Coherent Power Measurements

Coherent power measurements were taken at speeds 1 and 4 between five microphones and eight accelerometers strategically placed in the system as seen in Figure 8. These locations were selected using previous conclusions from near-field sound pressure, sound intensity, and tap test analyses, in part to see if the results could be replicated. Note that unknown systems can be analyzed by distributing microphones and accelerometers across the system. Eight accelerometers were placed on surfaces suspected of being dominant noise sources while four microphones were placed next to suspected sound radiating surfaces of interest. The fifth microphone was placed in the far-field to simulate what might be experienced by an operator. The objective is to determine which near-field microphones and accelerometers contribute the most to the far-field position. Multiple far-field points could similarly be analyzed simultaneously. Accelerometer to near-field microphone coherent power measurements were used to determine the presence of structural radiation in the company of nearby air-borne sources.

The coherence microphones measured overall sound pressure levels. The results identified microphone 3, located at the motor-end tail-section of the test bed, as the loudest

position at both speeds 1 and 4. The remaining four microphones ranked as follows when considering maximum measured overall sound pressure. The second loudest was microphone 4, located at the loading-end tail-section. Following the two loudest tail-sections of the system was microphone 2, located at an opening to the inside of the conveyor structure on the motor-end right side-section. Microphone 1, located at the motor and drive assembly of the system, had the lowest measured overall near-field sound pressure level. As expected the far-field microphone 5 received the lowest overall sound pressure of all five microphones. The above rankings for sound pressure levels hold for both speeds 1 and 4. These findings are consistent with near-field sound pressure and sound intensity results. The results of the measured overall sound pressure levels for the five coherent power microphones, with the loudest levels given in bold face type, can be seen in Table 14.

Table 14 Measured Overall Sound Pressure Levels of Coherence Microphones

	Overall SPL (dBA)				
	Mic 1	Mic 2	**Mic 3**	Mic 4	Mic 5
Speed 1	100	105.2	**106.3**	105.3	97.1
Speed 4	109	114.6	**117.4**	115.2	106.9

Two coherence techniques [11, 16] for identifying noise sources in a multiple source environment were used to analyze the coherent power data taken from the system. They are the FRF "Frequency Response Function" and the PCF "Partial Coherence Function" methods. The coherence data consists of accelerometer, near-field microphone, and far-field microphone measurements. Thus, the following coherent power contribution types were ranked and analyzed to develop an in depth understanding of noise sources and their contributions.

Coherent Power Contribution Types:

1.) accelerometer to near-field microphone

2.) accelerometer to far-field microphone

3.) near-field to far-field microphone

The dynamic signal analyzer used to collect coherence data provided values at discrete frequencies, which did not provide data for five 1/3-octave bands (16, 20, 32, 40, and 63 Hz). Tabulated data for these 1/3-octaves and other cases when no data exists are marked with "DNE" in this section.

4.4.1 Frequency Response Function (FRF) Approach

The FRF method results for accelerometer and microphone contributions are derived using the frequency response between the source and receiver. Due to the FRF technique's dependence on the use of the source / receiver frequency response function the results may exceed 100 % upon summing all source contributions. This occurs when there is coherence between the source signals. Nevertheless, the results can be used to rank the relative contributions from multiple sources to a receiver.

The FRF method applied to the accelerometer to near-field and far-field microphone overall (20-8,000 Hz) sound pressure level contributions can be seen in Table 15 for speed 1 and Table 16 for speed 4. The results are given in terms of relative contributions (% and dBA) where the maximum contributions are in bold face type. Note that overall and 1/3-octave values for the receivers may vary slightly throughout the FRF approach analysis. The variation is due to the use of multiple data files. As a result, percent contributions and corresponding level contributions referred to throughout the analysis may have mild discrepancies. However, when used jointly they provide relative noise contributions and the ability to identify dominant noise sources.

Table 15 FRF Accelerometer to Microphone Overall (20-8,000 Hz) Sound Pressure Level Contributions Speed 1

Speed 1		Overall Percent (%) Contributions To				
		Mic 1	Mic 2	Mic 3	Mic 4	Mic 5
Overall Percent (%) Contributions From	Accel 1	13	13	12	**46**	**14**
	Accel 2	12	11	10	29	14
	Accel 3	20	37	**50**	14	12
	Accel 4	**31**	**43**	38	17	12
	Accel 5	27	33	21	30	11
	Accel 6	26	28	22	27	11
	Accel 7	9	10	14	17	11
	Accel 8	22	19	18	19	11

		Overall SPL (dBA) Contributions To				
		Mic 1	Mic 2	Mic 3	Mic 4	Mic 5
Overall SPL (dBA) Contributions From	Accel 1	80.6	86.7	87.5	**99.1**	**78.8**
	Accel 2	80.9	85	86.3	94.8	78
	Accel 3	83.7	91.2	**100.1**	85.3	78.6
	Accel 4	**87.3**	**93.3**	96.9	86.9	78.3
	Accel 5	84.8	91	92.2	87.8	77.8
	Accel 6	84.4	91.1	92.6	86.4	78.1
	Accel 7	80	84.5	89.2	90.4	78.8
	Accel 8	85.8	90.5	90.5	85.9	77.9

Table 16 FRF Accelerometer to Microphone Overall (20-8,000 Hz) Sound Pressure Level Contributions Speed 4

Speed 4		Overall Percent (%) Contributions To				
		Mic 1	Mic 2	Mic 3	Mic 4	Mic 5
Overall Percent (%) Contributions From	Accel 1	10	9	10	**48**	10
	Accel 2	10	9	10	32	12
	Accel 3	23	**36**	**54**	13	12
	Accel 4	**26**	34	42	14	**13**
	Accel 5	18	20	25	12	9
	Accel 6	16	18	27	10	11
	Accel 7	18	11	11	7	9
	Accel 8	10	11	12	13	11

		Overall SPL (dBA) Contributions To				
		Mic 1	Mic 2	Mic 3	Mic 4	Mic 5
Overall SPL (dBA) Contributions From	Accel 1	88.1	93.6	97.5	**108.5**	86.5
	Accel 2	87.6	93.4	96.8	103.2	87.5
	Accel 3	95.2	**102.3**	**111.6**	95.5	88.1
	Accel 4	**96.2**	102.1	108.6	95.4	**88.1**
	Accel 5	93.7	100.2	105.9	94.1	85.9
	Accel 6	92.9	100.3	106.9	94	86.1
	Accel 7	93.5	95.8	98.3	91.8	85.9
	Accel 8	88.2	93.3	96.9	96.3	86.1

By examining the first column of Tables 15 and 16, it can be seen that accelerometer 4 (motor-end left side-section) is the most contributive source to microphone 1 (motor) at both speeds 1 (31 %) and 4 (26 %). Also, the contribution of accelerometer 8 to microphone 1, both located on the motor, drops from 22% at speed 1 to 10% at speed 4. This clarifies that the motor's contribution is further suppressed by the conveyor contribution when the speed of operation is increased. From column 2, it is observed that microphone 2, located at the opening in the side of the conveyor, receives the greatest contribution from accelerometer 4 (motor-end left side-section) at speed 1 and from accelerometer 3 (motor-end tail-section) at speed 4. High contribution levels from accelerometers 3 and 4 to microphones 1 and 2 demonstrate that the steel plates that make up the motor-end left side-section and the motor-end tail-section produce the greatest amount of sound pressure inside the conveyor component which flows from the opening in the motor-end right side-section. Similarly, examining columns 3 and 4 of Tables 15 and 16 revealed that accelerometer 3 dominates microphone 3 (motor-end tail-section) and accelerometer 1 dominates microphone 4 (loading-end tail-section), both at speeds 1 and 4. These results are consistent with intuition. This is expected due to the close proximity of these near-field microphones to their respective accelerometers as can be seen in Figure 8. Column 5 of Table 15 identified accelerometer 1 as the greatest contributor to far-field microphone 5 at speed 1 and Table 16 identified accelerometer 4 to be the greatest at speed 4. However, the separation of the greatest contributors here is not significant enough to make certain conclusions about the dominant source contributions to the far-field microphone.

Figure 23 gives the broadband coherent power from accelerometer 3 to microphone 3, represented by the cyan line. Corresponding 1/3-octave values are represented by the magenta line and overall value by the gold line. The auto-spectrum of microphone 3 is shown using blue, green and red lines which represent the broadband, 1/3-octave, and overall (20-8,000 Hz) values, respectively. The presence of multiple coherent peaks suggests high structural contributions from respective sections at those frequencies, where the cyan line nearly touches the blue line. High coherent power contributions that correspond with recurring peak frequencies denoted in previous analyses were identified at 925, 1,300, 2,275, and 4,225 Hz, which have also been identified for speed 4.

Table 17 lists 1/3-octave and overall auto-spectral values of microphone 3 with respective coherent power and percent contributions from accelerometer 3. This table also identifies the 1,250 Hz 1/3-octave, in bold face type, as having the greatest 1/3-octave sound pressure level for microphone 3. The 1,250 Hz 1/3-octave band of microphone 3 has a value of 99.4 dBA and receives a significant 54 % contribution of 94 dBA from accelerometer 3 for speed 1. For speed 4, the 1,600 Hz 1/3-octave band dominates microphone 3 at 110.6 dBA receiving a major 46 % contribution of 103.8 dBA. Similar plots and tables were created at both speeds 1 and 4 for all source / receiver combinations analyzed with the FRF coherence technique.

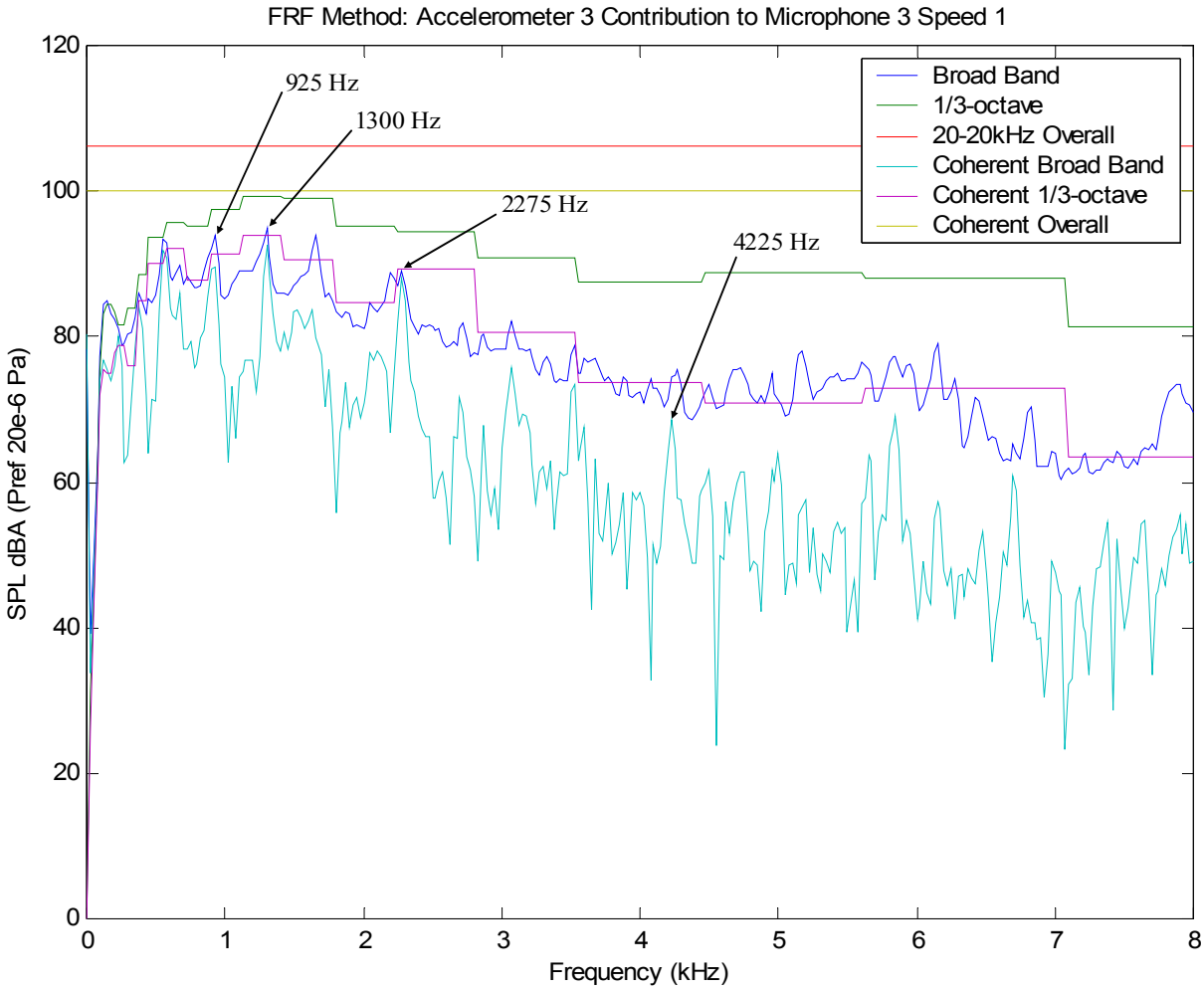

Figure 23 FRF Coherent Sound Pressure Level from Accelerometer 3 to Microphone 3 Speed 1

Table 17 1/3-octave and Overall FRF Coherent Sound Pressure Levels Accelerometer 3 to Microphone 3 Speed 1

1/3-octave (Hz)	SPL (dBA) Mic 3	SPL (dBA) from Accel 3	Contribution (%)
16	DNE	DNE	DNE
20	DNE	DNE	DNE
25	31.1	25.8	54
32	DNE	DNE	DNE
40	DNE	DNE	DNE
50	46.1	44.4	83
63	DNE	DNE	DNE
80	64.2	60.8	68
100	75.2	71.8	67
125	83.2	75.4	41
160	84.4	75	34
200	83.3	77.8	53
250	81.5	78.8	73
315	83.9	75.9	40
400	88.5	84.9	66
500	93.7	90.1	66
630	95.6	92.1	67
800	95.1	87.8	43
1000	97.5	91.4	49
1250	**99.4**	**94**	**54**
1600	99	90.6	38
2000	95.3	84.8	30
2500	94.5	89.3	55
3150	90.9	80.6	31
4000	87.5	73.6	20
5000	88.7	70.9	13
6300	88	72.9	18
8000	82.8	64.7	12
Overall	106.3	100.1	50

Primary results of the FRF contributions from accelerometer 3 to microphone 3 are summarized in Table 18, which lists a total of twenty-two frequencies with high contribution. These include the four identified from near-field sound pressure, sound intensity, and tap test analyses, which are given in bold. Microphone 3 received 50 % and greater overall contributions from accelerometer 3 at both speeds as seen in Table 18. The 1-3 kHz band was scanned for greatest 1/3-octave contributions. This band was chosen in accordance with the most sensitive part of the human hearing range. Results revealed the 2,500 Hz 1/3-octave as the most contributive from accelerometer 3 to microphone 3 at both speeds under test. Further details regarding the findings discussed above are summarized in Table 18.

Table 18 Summary Results of FRF Contributions to Microphone 3

	Speed 1	Speed 4
Microphone 3 Overall SPL (dBA)	106.3 dBA	117.4 dBA
Source	Accelerometer 3	Accelerometer 3
Overall Contribution (%) [SPL (dBA)]	50 % [100.1 dBA]	54 % [111.6 dBA]
Most Contributive 1/3-octave (Hz) [SPL (dBA)] *	2500 Hz [94.5 dBA] *	2500 Hz [108.2 dBA] *
1/3-octave Contribution (%) [SPL (dBA)] *	55 % [89.3 dBA] *	80 % [106.2 dBA] *
Discrete Frequencies with High Contribution (Hz)	225, 375, 550, **925**, **1300**, **2275**, 3525, **4225**, 6700, 11025, 11900, 12900, 14675, 16325, 18875, 19250, 19350	225, 375, 550, **925**, **1300**, 1750, **2275**, 2850, **4225**, 5000, 5825, 7625

* Spanning 1-3 kHz in accordance with most sensitive band of human hearing range

Figure 24 gives broadband, 1/3-octave, and overall (20-8,000 Hz) coherent power from accelerometer 3 to far-field microphone 5 at speed 4. A recurring broadband peak contribution from accelerometer 3 to far-field microphone 5 has been identified at 2,275 Hz as in Figure 24. This peak frequency was also contributed to microphone 3 and is seen to be efficiently

transmitted to the far-field at speed 4. Primary results of the FRF contributions from accelerometer 3 to far-field microphone 5 are summarized in Table 19. Next, the near-field to far-field microphone contributions will be analyzed. Note that microphone-to-microphone contributions cover the 20-20,000 Hz band.

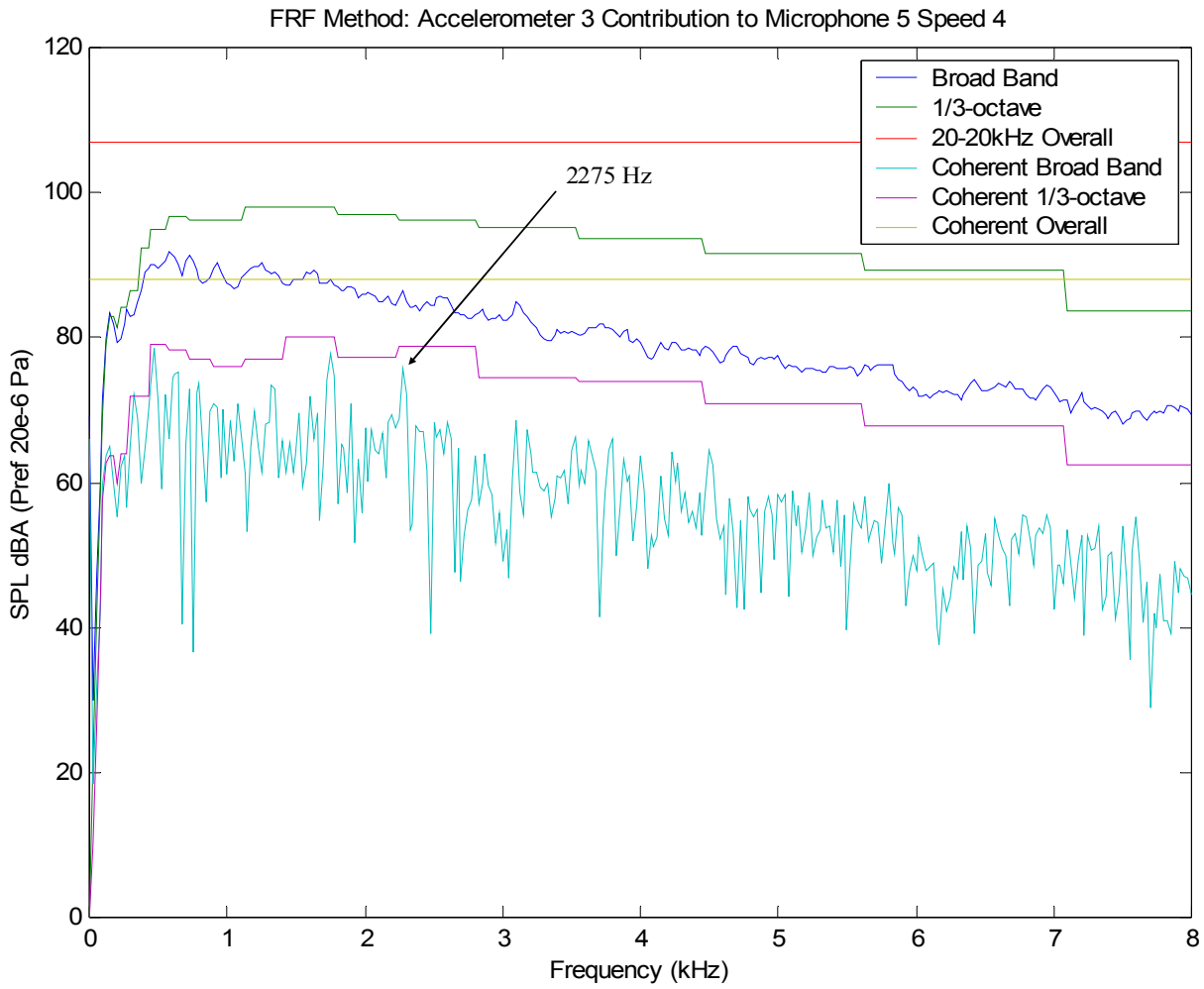

Figure 24 FRF Coherent Sound Pressure Level from Accelerometer 3 to Microphone 5 Speed 4

Table 19 Summary Results of FRF Contributions to Microphone 5

	Speed 1		Speed 4	
Microphone 5 Overall SPL (dBA)	97.1 dBA		106.9 dBA	
Source	Accelerometer 3	Microphone 3	Accelerometer 3	Microphone 3
Overall Contribution (%) [SPL (dBA)]	12 % [78.6 dBA]	21% [80.6 dBA]	12 % [88.1 dBA]	17 % [88.5 dBA]
Most Contributive 1/3-octave (Hz) [SPL (dBA)] *	1000 Hz [88.8 dBA] *	1000 Hz [88.8 dBA] *	1600 Hz [98 dBA] *	2000 Hz [96.9 dBA] *
1/3-octave Contribution (%) [SPL (dBA)] *	15 % [72.6 dBA] *	16 % [72.8 dBA] *	13 % [80.1 dBA] *	11 % [77.6 dBA] *
Discrete Frequencies of High Contribution (Hz)	3175, 3650, 5825, 11050, 11400, 13325, 14975, 16125, 16500	8400, 8525, 11250, 13100, 13425, 14700, 15900, 16275	475, 1750, **2275**, 8600, 11900, 16125, 16650	150, 600, 1875, **2275**, 11000, 13150, 13350, 16725

* Spanning 1-3 kHz in accordance with most sensitive band of human hearing range

Near-field to far-field microphone overall sound pressure level contributions can be seen in Table 20 for speed 1 and Table 21 for speed 4. The results identified microphone 2, located at an opening to the inside of the conveyor in the motor-end right side-section, to be the greatest contributor to the far-field microphone 5 at both speeds 1 and 4. The contribution seems to increase and become slightly greater than the other microphones with an increase in speed. This strong relative contribution from microphone 2, located at an opening in the side of the conveyor, to the far-field microphone further supports that a significant amount of energy exists inside the conveyor and should be contained or damped through treatments. However, once again the separation of the greatest contributor here is not significant enough to make certain conclusions about the dominant source contributions to the far-field microphone.

Table 20 FRF Microphone to Microphone Overall (20-20,000 Hz) Sound Pressure Level Contributions Speed 1

Speed 1		Overall Percent (%) Contributions To				
		Mic 1	Mic 2	Mic 3	Mic 4	Mic 5
Overall Percent (%) Contributions From	Mic 1	-	59	41	32	20
	Mic 2	53	-	48	26	**21**
	Mic 3	38	51	-	25	21
	Mic 4	25	23	18	-	20
	Mic 5	19	18	21	26	-

		Overall SPL (dBA) Contributions To				
		Mic 1	Mic 2	Mic 3	Mic 4	Mic 5
Overall SPL (dBA) Contributions From	Mic 1	-	96.2	94.7	91.5	82.2
	Mic 2	91.8	-	95.9	91.2	**82.7**
	Mic 3	87.7	93.1	-	92.4	80.6
	Mic 4	83.3	88.9	89.2	-	80.1
	Mic 5	85	90.3	90.3	92.3	-

Table 21 FRF Microphone to Microphone Overall (20-20,000 Hz) Sound Pressure Level Contributions Speed 4

Speed 4		Overall Percent (%) Contributions To				
		Mic 1	Mic 2	Mic 3	Mic 4	Mic 5
Overall Percent (%) Contributions From	Mic 1	-	48	39	18	16
	Mic 2	47	-	37	18	**20**
	Mic 3	39	41	-	16	17
	Mic 4	21	20	24	-	18
	Mic 5	17	18	19	18	-

		Overall SPL (dBA) Contributions To				
		Mic 1	Mic 2	Mic 3	Mic 4	Mic 5
Overall SPL (dBA) Contributions From	Mic 1	-	102.4	106.2	95.3	88
	Mic 2	97.5	-	104.8	95.2	**89.6**
	Mic 3	97.1	101.3	-	96.5	88.5
	Mic 4	91.7	96.9	103.1	-	89
	Mic 5	91.3	97.1	101	95.7	-

Upon viewing the spectral distribution of coherent power from microphone 2 to microphone 5 in Figure 25, peak contributions significantly decrease across the bandwidth from speed 1 to speed 4, while the overall percent contribution remains relatively the same. This result leads to the conclusion that source identification becomes increasingly difficult for the FRF method as background noise levels increase with speed. When considering peak contributions from microphone 3 to far-field microphone 5, a recurring peak at 2,275 Hz has once more been identified at speed 4 as in Figure 26. The presence of this peak contribution frequency originating from the motor-end tail-section is contributed to microphone 3 and further seen to be efficiently transmitted to far-field microphone 5. Summary results of the FRF contributions to microphone 5 were already given in Table 19.

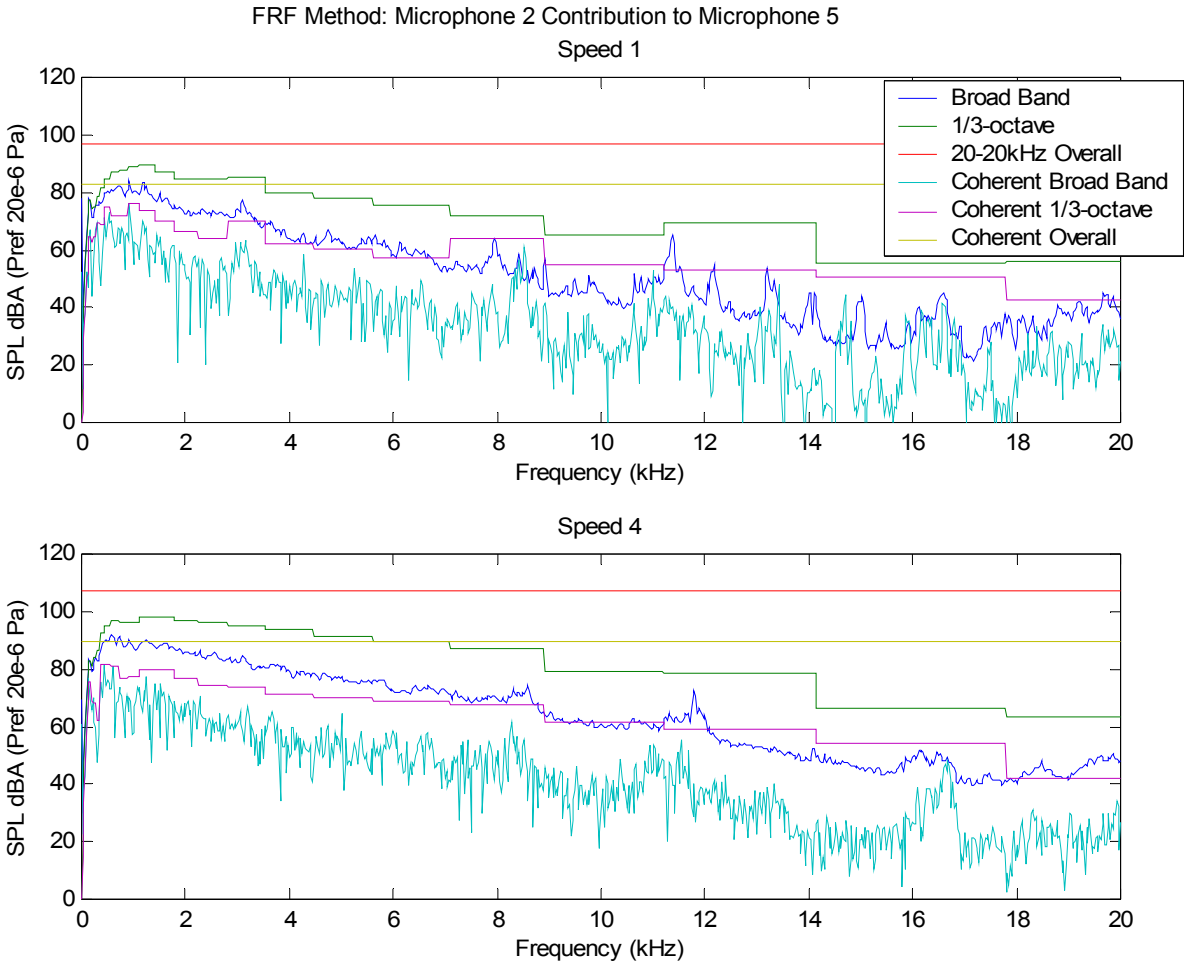

Figure 25 FRF Coherent Sound Pressure Level from Microphone 2 to Microphone 5

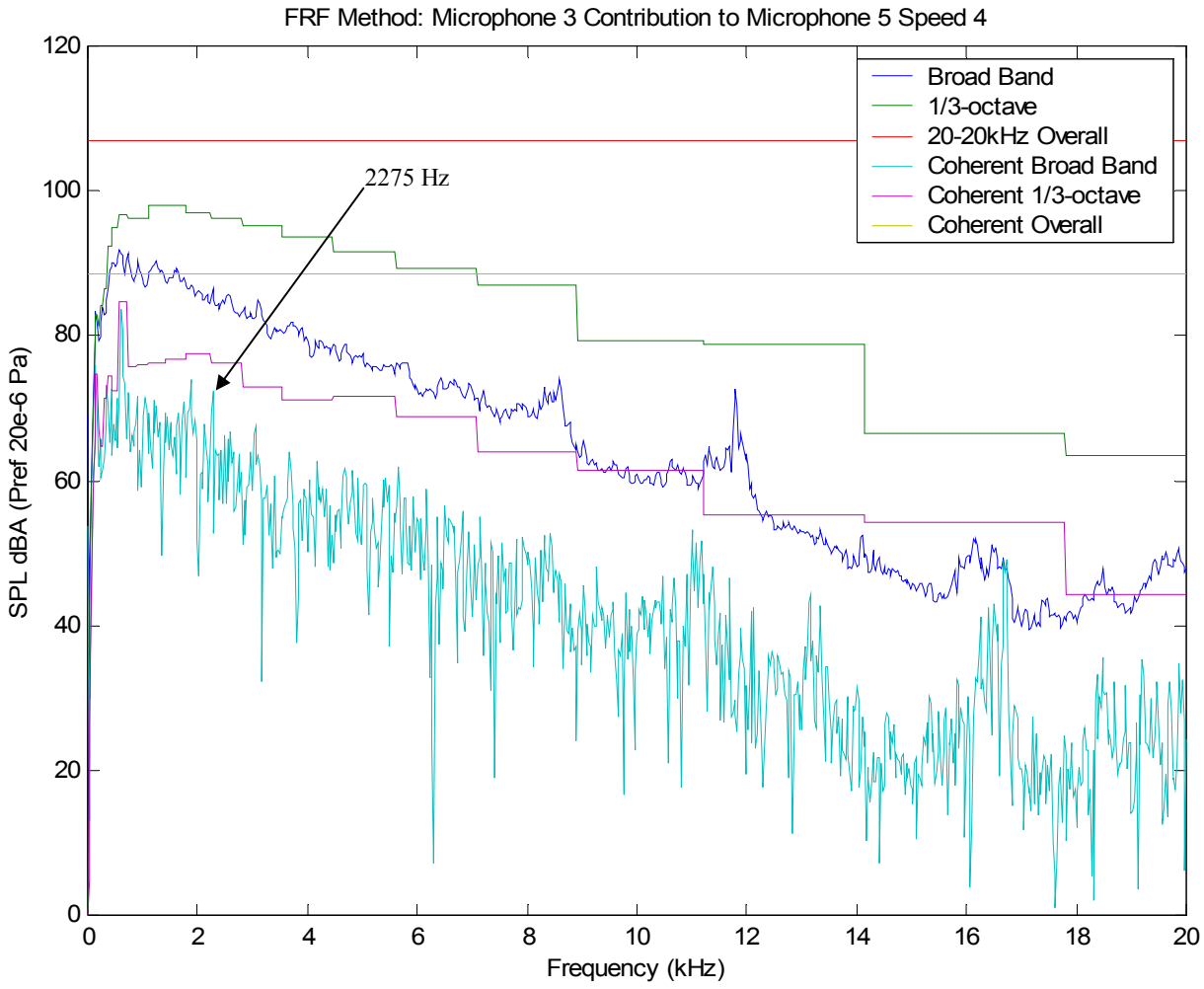

Figure 26 FRF Coherent Sound Pressure Level from Microphone 3 to Microphone 5 Speed 4

The motor-end tail-section was the only section found to have frequencies in common with those identified from the near-field sound pressure, sound intensity, and tap test analyses, see bold face type values in Table 13. The frequencies are 925, 1,300, 2,275, and 4,225 Hz and exist at both speeds 1 and 4. Also, 2,275 Hz is the only one of these recurring frequencies found by the FRF method to be efficiently transmitted to the far-field at speed 4.

4.4.2 Partial Coherence Function (PCF) Approach

The PCF method is a more complex method of determining coherent power contributions. Due to the limited cross-computational ability of the measurement equipment only four sources could be analyzed per receiver. Thus, accelerometers 1-4 were analyzed as a group separately from accelerometers 5-8. For this reason, the overall and 1/3-octave values for the receivers may vary slightly throughout the PCF analysis, and as a result reference of relative percentages may be incongruous. However, valid conclusions can be made about identifying dominant noise sources. Firstly, accelerometer to near-field and far-field microphone overall (20-8,000 Hz) sound pressure level contributions are given in Table 22 for speed 1 and Table 23 for speed 4 in terms of percent and dBA of relative contributions. The largest contributions are denoted with bold face type.

Table 22 PCF Accelerometer to Microphone Overall (20-8,000 Hz) Sound Pressure Level Contributions Speed 1

Speed 1		Overall Percent (%) Contributions To				
		Mic 1	Mic 2	Mic 3	Mic 4	Mic 5
Overall Percent (%) Contributions From	Accel 1	10	10	9	**38**	10
	Accel 2	9	8	8	17	10
	Accel 3	16	22	**41**	8	11
	Accel 4	**27**	**27**	23	13	10
	Accel 5	17	25	19	15	10
	Accel 6	17	18	18	12	11
	Accel 7	9	10	13	15	**11**
	Accel 8	15	16	13	10	10

		Overall SPL (dBA) Contributions To				
		Mic 1	Mic 2	Mic 3	Mic 4	Mic 5
Overall SPL (dBA) Contributions From	Accel 1	79.1	85	85.6	**97.7**	78.1
	Accel 2	79.4	83.6	84.6	90.3	77.3
	Accel 3	82.3	89.7	**98.6**	83.4	78.3
	Accel 4	**86.4**	**92.2**	92.6	85.3	78.3
	Accel 5	83.7	90.6	92.3	85.6	77.7
	Accel 6	83.3	90.3	92.1	85.3	78.3
	Accel 7	79.5	84.8	89	90	**78.9**
	Accel 8	85.1	89.6	89.2	85.4	77.9

Table 23 PCF Accelerometer to Microphone Overall (20-8,000 Hz) Sound Pressure Level Contributions Speed 4

Speed 4		Overall Percent (%) Contributions To				
		Mic 1	Mic 2	Mic 3	Mic 4	Mic 5
Overall Percent (%) Contributions From	Accel 1	9	9	8	**42**	10
	Accel 2	9	9	8	15	11
	Accel 3	13	19	**40**	9	11
	Accel 4	**20**	**20**	30	10	**11**
	Accel 5	15	19	20	11	9
	Accel 6	14	17	22	10	10
	Accel 7	17	10	10	8	9
	Accel 8	11	12	12	14	10

		Overall SPL (dBA) Contributions To				
		Mic 1	Mic 2	Mic 3	Mic 4	Mic 5
Overall SPL (dBA) Contributions From	Accel 1	87.5	93.4	95.6	**108.3**	86.4
	Accel 2	86.9	93.5	95.4	98.1	87.2
	Accel 3	91.5	100	**109.7**	93.8	87.4
	Accel 4	**93.9**	**100.4**	106.9	94.3	**87.6**
	Accel 5	92.6	99.8	104.1	93.7	85.8
	Accel 6	91.8	100.1	105.5	94	85.7
	Accel 7	93.3	95.4	98	91.7	86.2
	Accel 8	88.4	93.9	97.4	96.7	86.5

Upon examining the first two columns of Tables 22 and 23 accelerometer 4 (motor-end left side-section) was identified from the results to be the most contributive source to microphone 1 (motor) and microphone 2 located at the opening in the side of the conveyor, at both speeds 1 and 4. Results are nearly identical to those from the FRF approach including how the contribution of accelerometer 8 on the motor to microphone 1 by the motor drops from 15 % at speed 1 to 11 % at speed 4, indicating higher incoherent background noise. Also, PCF method results again reveal that the steel plates that make up the motor-end left side-section and the motor-end tail-section produce the greatest amount of sound pressure inside the conveyor. As with the FRF approach, the PCF method provided that the accelerometers located on the tail-sections dominate the collocated near-field microphones. Again for the PCF method, the separation of accelerometer to far-field microphone contributions in Tables 22 and Table 23 is not significant enough to make certain conclusions regarding dominant sources.

The identification of discrete frequency points where accelerometer 3 is highly contributive to microphone 3 and common to frequencies identified in previous analyses for the motor-end tail-section can be seen in Figure 27 for speed 1. Corresponding 1/3-octave and overall (20-8,000 Hz) values with respective percent contributions are listed in Table 24. Recurring peak contributions were again identified at 925, 1,300, 2,275, and 4,225 Hz for speeds 1 and 4. Similar plots and tables were also created for all combinations analyzed with the PCF method. When comparing Figures 23 and 27, very similar results are observed.

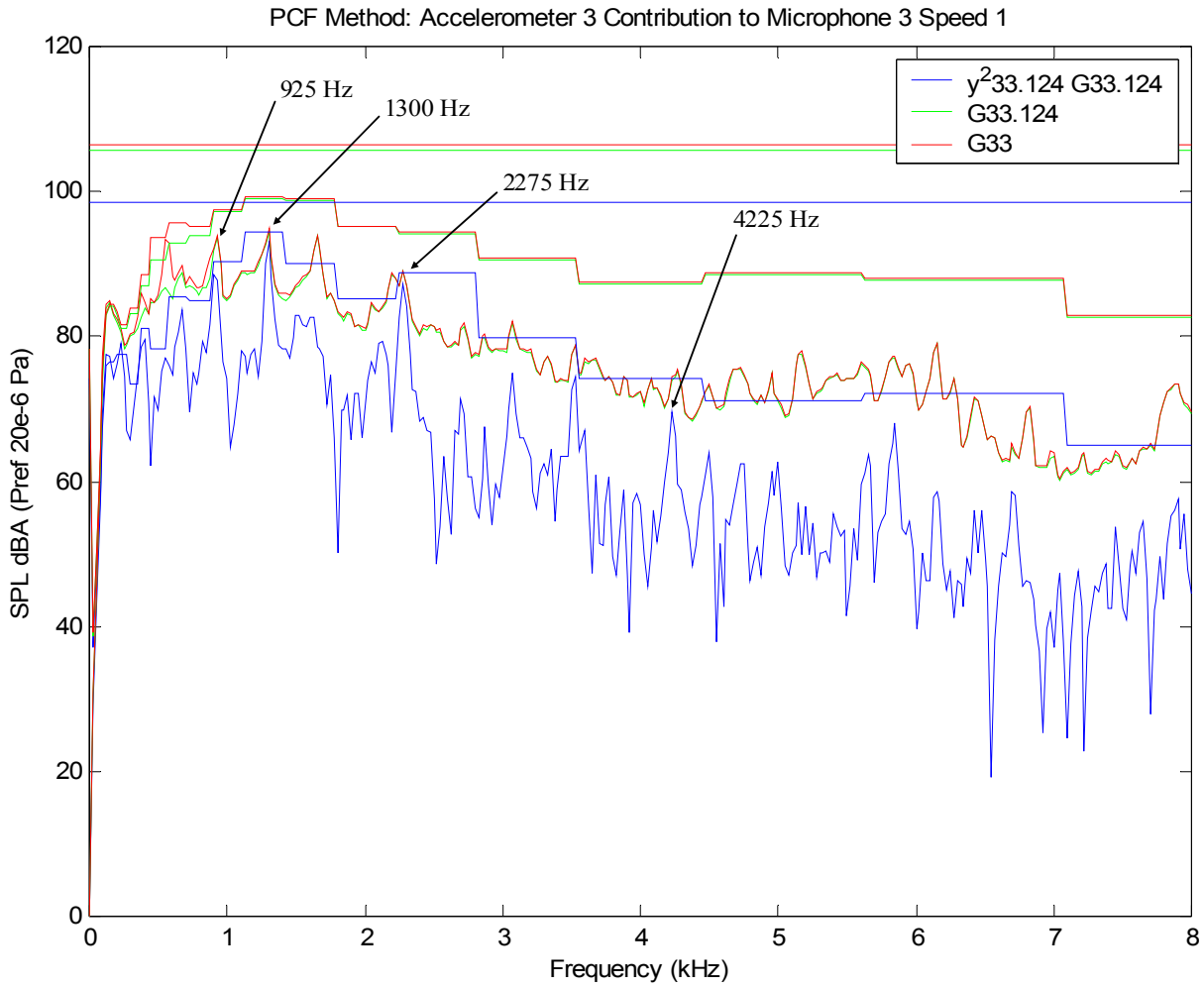

Figure 27 PCF Coherent Sound Pressure Level from Accelerometer 3 to Microphone 3 Speed 1

Table 24 1/3-octave and Overall PCF Coherent Sound Pressure Levels Accelerometer 3 to Microphone 3 Speed 1

		Residual	Coherent Residual	
1/3-octave (Hz)	SPL (dBA) Mic 3	SPL (dBA) from Accel 3	SPL (dBA) from Accel 3	Contribution (%)
16	DNE	DNE	DNE	DNE
20	DNE	DNE	DNE	DNE
25	31.1	30.6	29.1	79
32	DNE	DNE	DNE	DNE
40	DNE	DNE	DNE	DNE
50	46.1	46	43.9	78
63	DNE	DNE	DNE	DNE
80	64.2	62.8	57.2	45
100	75.2	73.3	67.2	40
125	83.2	82.8	76.1	44
160	84.4	84.2	76.5	40
200	83.3	83	77.5	51
250	81.5	81.2	77.6	63
315	83.9	83.3	73.4	30
400	88.5	87.1	81.1	42
500	93.7	90.5	78.3	17
630	95.6	92.9	85.5	31
800	95.1	93.8	85	31
1000	97.5	97.2	90.2	43
1250	**99.4**	**99**	**94.5**	**57**
1600	99	98.8	90	36
2000	95.3	95.1	85.2	31
2500	94.5	94.3	88.7	51
3150	90.9	90.6	79.8	28
4000	87.5	87.3	74.1	21
5000	88.7	88.5	71.2	13
6300	88	87.8	72.1	16
8000	82.8	82.6	65	13
Overall	106.3	105.7	98.6	41

A summary of key results for the PCF contributions from accelerometer 3 to microphone 3 are summarized in Table 25. Only sixteen peak contribution frequencies were identified by the PCF method for this source / receiver combination, which is six less than identified by the FRF approach. However, these also include the four frequencies denoted throughout this chapter and are presented with bold text in Table 25. The PCF method predicted a more conservative 40-41 % overall contribution from accelerometer 3 where the FRF method determined values of 50 % and greater. Differences in the most contributive 1/3-octave predictions exist at speed 1 were the PCF method identified the 1,250 Hz 1/3-octave as an alternative to the 2,500 Hz 1/3-octave identified by the FRF technique. Further contrast between results for contributions from accelerometer 3 to microphone 3 obtained using the FRF and PCF methods can be made with results from Tables 18 and 25.

Table 25 Summary Results of PCF Contributions to Microphone 3

	Speed 1	Speed 4
Microphone 3 Overall SPL (dBA)	106.3 dBA	117.4 dBA
Source	Accelerometer 3	Accelerometer 3
Overall Contribution (%) [SPL (dBA)]	41 % [98.6 dBA]	40 % [109.7 dBA]
Most Contributive 1/3-octave (Hz) [SPL (dBA)] *	1250 Hz [99.4 dBA] *	2500 Hz [108.2 dBA] *
1/3-octave Contribution (%) [SPL (dBA)] *	57 % [94.5 dBA] *	67 % [104.8 dBA] *
Discrete Frequencies of High Contribution (Hz)	225, **925**, **1300**, **2275**, 3525, **4225**, 11025, 11900, 12875, 14650, 16300, 19400	375, 610, **925**, **1300**, 1750, **2275**, 2850, **4225**

* Spanning 1-3 kHz in accordance with most sensitive band of human hearing range

The PCF method has also identified the recurring broadband frequency of 2,275 Hz as having peak contributions from accelerometer 3 and microphone 3 to microphone 5 at speed 4. This further supports that this frequency is in fact transmitted to the far-field at this speed. Significant results of these PCF contributions to microphone 5 are summarized in Table 26. Overall contribution results are once more slightly less than those determined by the FRF method. Results for most contributive 1/3-octave contributions from accelerometer 3 are also in agreement following this same trend, while for microphone 3 the 1,250 Hz 1/3-octave is most contributive at speed 1 and the 1,000 Hz 1/3-octave is greatest at speed 4.

Table 26 Summary Results of PCF Contributions to Microphone 5

	Speed 1		Speed 4	
Microphone 5 Overall SPL (dBA)	97.1 dBA		106.9 dBA	
Source	Accelerometer 3	Microphone 3	Accelerometer 3	Microphone 3
Overall Contribution (%) [SPL (dBA)]	11 % [78.3 dBA]	19% [79.3 dBA]	11 % [87.4 dBA]	13 % [87 dBA]
Most Contributive 1/3-octave (Hz) [SPL (dBA)] *	1000 Hz [88.8 dBA] *	1250 Hz [89.7 dBA] *	1600 Hz [98 dBA] *	1000 Hz [96.9 dBA] *
1/3-octave Contribution (%) [SPL (dBA)] *	14 % [71.6 dBA] *	13 % [72 dBA] *	11 % [78.7 dBA] *	10 % [76.5 dBA] *
Discrete Frequencies of High Contribution (Hz)	5825, 9350, 11400, 13325, 14975, 16100, 16525	150, 875, 1250, 3175, 6650, 8350, 11350, 13450, 16475	475, 1750, **2275**, 8600, 11900, 16125, 16650	625, 1750, **2275**, 8600, 11900, 16125, 16675

* Spanning 1-3 kHz in accordance with most sensitive band of human hearing range

The PCF method applied to the near-field to far-field microphone overall sound pressure level contributions can be seen in Table 27 for speed 1 and Table 28 for speed 4. Just as the FRF method, the results identified microphone 2 as the greatest contributor to microphone 5. The contribution seems to increase and become greater than the other microphones with an increase in speed. This further supports that a significant amount of energy exists inside the conveyor. As with the FRF method, the separation of the greatest contributor here is once more insufficient to draw conclusions about dominant source contributions to the far-field microphone.

Table 27 PCF Microphone to Microphone Overall (20-20,000 Hz) Sound Pressure Level Contributions Speed 1

Speed 1		Overall Percent (%) Contributions To				
		Mic 1	Mic 2	Mic 3	Mic 4	Mic 5
Overall Percent (%) Contributions From	Mic 1	-	37	21	18	18
	Mic 2	41	-	33	14	**18**
	Mic 3	22	29	-	19	19
	Mic 4	14	11	13	-	16
	Mic 5	15	15	14	19	-

		Overall SPL (dBA) Contributions To				
		Mic 1	Mic 2	Mic 3	Mic 4	Mic 5
Overall SPL (dBA) Contributions From	Mic 1	-	94.2	90.6	87.9	80.6
	Mic 2	89.3	-	93.7	87.4	**81.2**
	Mic 3	83.8	90.8	-	91.9	79.3
	Mic 4	81.4	86.6	89.3	-	80
	Mic 5	82.5	88	88	90	-

Table 28 PCF Microphone to Microphone Overall (20-20,000 Hz) Sound Pressure Level Contributions Speed 4

Speed 4		Overall Percent (%) Contributions To				
		Mic 1	Mic 2	Mic 3	Mic 4	Mic 5
Overall Percent (%) Contributions From	Mic 1	-	33	27	16	13
	Mic 2	36	-	27	12	**16**
	Mic 3	25	25	-	17	13
	Mic 4	12	11	15	-	15
	Mic 5	12	12	12	18	-

		Overall SPL (dBA) Contributions To				
		Mic 1	Mic 2	Mic 3	Mic 4	Mic 5
Overall SPL (dBA) Contributions From	Mic 1	-	101.8	104.4	94.2	87.4
	Mic 2	96.3	-	103.4	93.7	**88.9**
	Mic 3	95.7	100.5	-	95.7	87
	Mic 4	89.6	94.3	99.5	-	87.8
	Mic 5	89.4	95.7	98.5	94.9	-

Significant decreases in microphone 2's peak power contributions to microphone 5 from speed 1 to speed 4 were also observed using the PCF method. Also, the overall percent contribution remained relatively the same as with the FRF method. This leads to the conclusion that broadband noise levels become increasingly contributive with speed while broadband peak contributions from microphone 2 become less significant.

The results for the PCF method nearly agree with those determined with the FRF method, but tend to become more conservative as speed increases. This occurs because source cross-contamination increases with speed and the FRF method determines individual contributions which include signal portions common with other sources, while the PCF method identifies the unique contributions ignoring portions coherent with other sources. This suggests that the FRF method will estimate the greatest possible amount that a source will contribute while the PCF method will estimate the least amount. The actual contribution will be somewhere between the FRF and PCF determinations.

The FRF and PCF methods concur that the motor-end tail-section was the only section found to have frequencies in common with those identified from the near-field sound pressure, sound intensity, and tap test analyses. The frequencies are 925, 1,300, 2,275, and 4,225 Hz and exist at both speeds 1 and 4. The PCF method also reveals that the 2,275 Hz recurring frequency is the only one to be efficiently transferred to the far field at speed 4. Highly contributive frequencies produced by the motor-end tail-section that were identified by the two coherence methods and the tap test analysis are summarized in Table 29 for speeds 1 and 4. Corresponding recurring frequencies denoted in the near-field sound pressure and sound intensity analyses are in bold face type.

Table 29 Motor-End Tail-Section: Coherent Power / Tap Test Significant Frequencies

	Accelerometer 3 to Microphone 3				Motor-End Tail-Section Tap Test SPL Related Frequencies	
	FRF Method		PCF Method			
	Speed 1	Speed 4	Speed 1	Speed 4	Speed 1	Speed 4
Frequencies (Hz)	225	225	225			
	375	375		375		
	550	550				
				610	610	610
	925	**925**	**925**	**925**	**925**	**925**
	1300	**1300**	**1300**	**1300**	**1300**	**1300**
						1610
		1750		1750		
	2275	**2275**	**2275**	**2275**	**2275**	**2275**
		2850		2850		
					3150	3150
					3510	3510
	3525		3525			
	4225	**4225**	**4225**	**4225**	**4225**	**4225**
		5000				5000
		5825				
	6700					6700
						7610
		7625				
					9180	9180
					10630	10630
	11025		11025			
	11900		11900			
			12875			
	12900					
			14650			
	14675					
			16300			
	16325					
	18875					
	19250					
	19350					
			19400			

4.5 Enhanced Time Measurements

Enhanced time measurements were applied to the system to identify signal portions related to the repetitive or cyclic passing of the conveyor flights. The signals were measured with four accelerometers, and three microphones. The accelerometers were placed on the bottom surface of the top conveyor sections to measure structural response signals. Two microphones were placed in the near-field of each tail-section since these are the loudest areas of the system, while the third was placed in the far-field. A capacitive proximity sensor was positioned at the edge of either tail-section to trigger when each flight passes. Accelerometer and microphone signals were first measured and averaged in the frequency domain using a "free-run" trigger in order to capture the entire response of each signal. Standard auto-spectrums resulted. Next, the signals were measured in the time domain using the flight triggering to capture the time-averaged response for two consecutive flight events. Twenty averages produced the best results for analysis. The time-averaged signals were then correlated with the spatial distribution of the conveyor chain as shown in Figure 28.

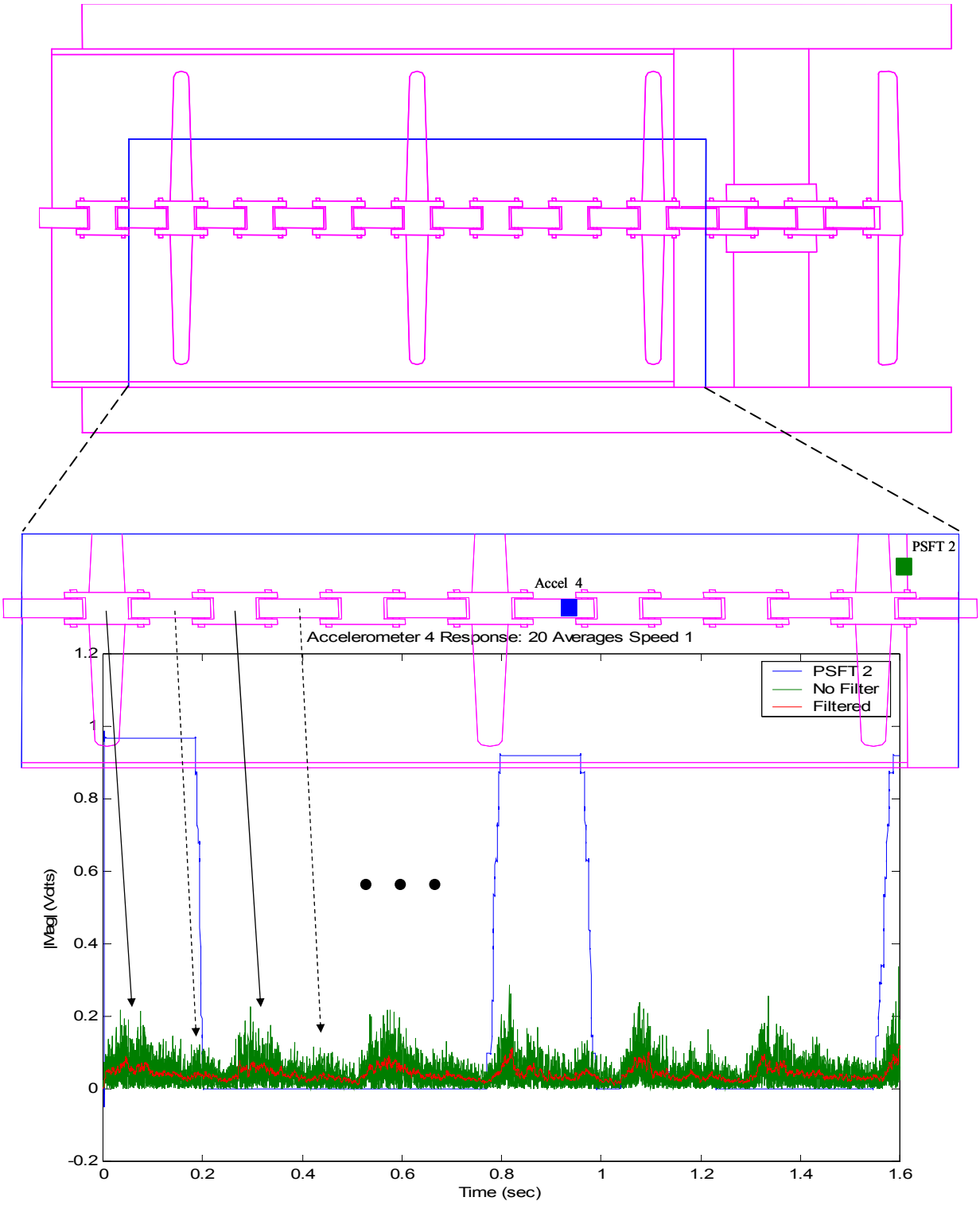

Figure 28 Accelerometer 4 Time Averaged Response Speed 1

The flight trigger signal is represented by the blue line; a high value (0.95 volts) signals the flight presence. The green line shows the time-averaged response of accelerometer 4 (motor-end tail-section) for two consecutive flight events. This signal was post-processed using MATLAB's "filter.m" script to produce the low-pass filtered response in red. Drive-link events correspond with the large humps identified by the solid arrows, while the smaller humps are caused by the idler-links as pointed out by the dashed arrows. There is no distinction in the signals between the response to drive-links and that of the flights.

Time-averaged signals were converted to the frequency domain using MATLAB's "psd.m" script, which estimated the power spectral density of the signal. Frequency-averaged and time-averaged spectra were plotted together to discern the cycle-related portion of the overall signal content. Also, the difference between these signals was plotted to gain a clear perspective of frequencies dominated by cyclic events, which occur where the difference is zero.

The cycle-related signal content of near-field microphone 2 (motor-end tail-section) is shown in Figures 29 and 30 for speeds 1 and 4, respectively. It is interesting to note that the time-averaged and frequency-averaged signals in both figures have nearly the same spectral content over the frequency band but the time-averaged spectrum is lower. Also, it was observed that as the number of averages increased the time-averaged signal diverged from the frequency-averaged signal. This implies that the signal content is mostly unrelated to the flight cycle or that the periodic process is not exactly repeatable.

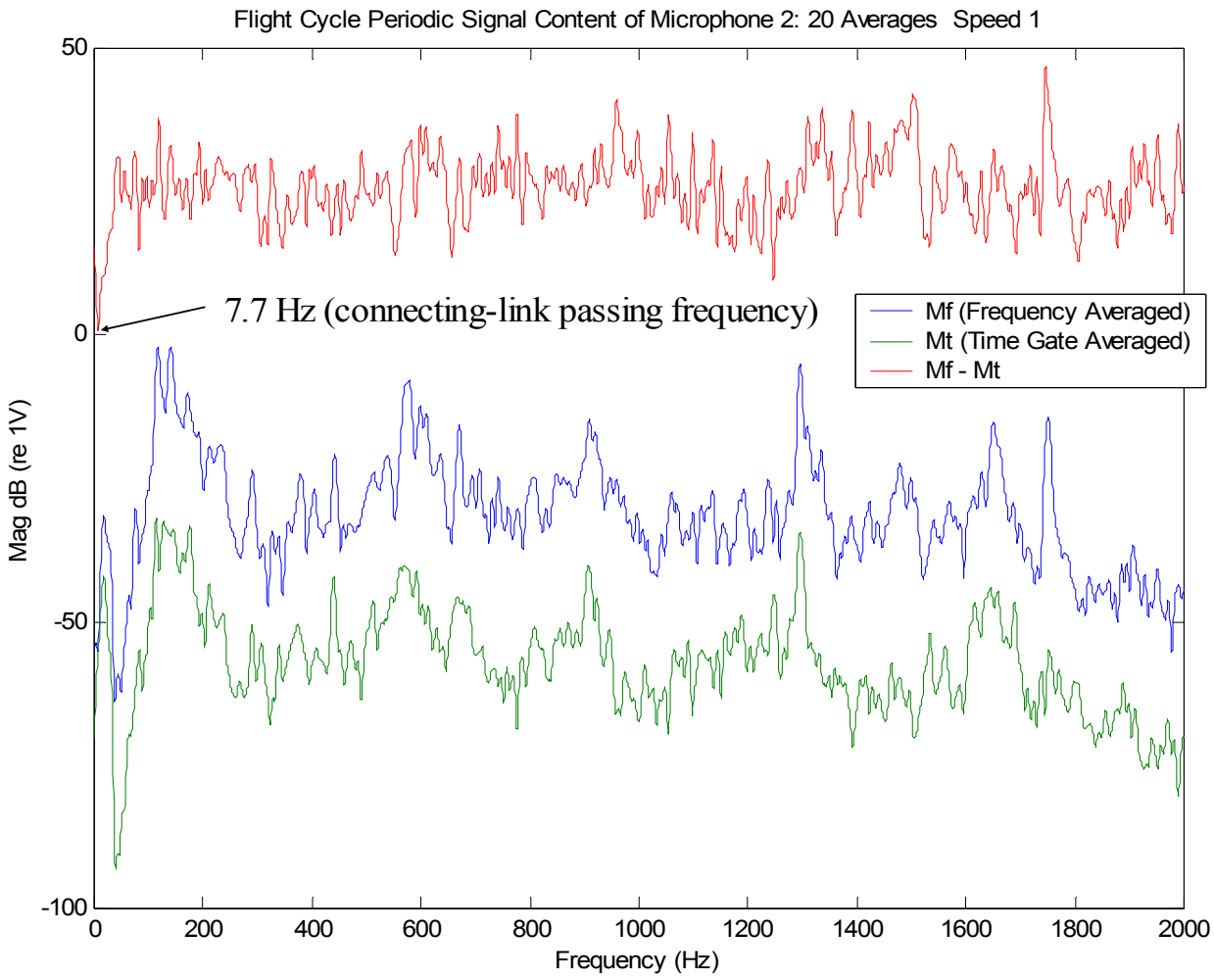

Figure 29 Time-Averaged / Frequency-Averaged Response Microphone 2 Speed 1

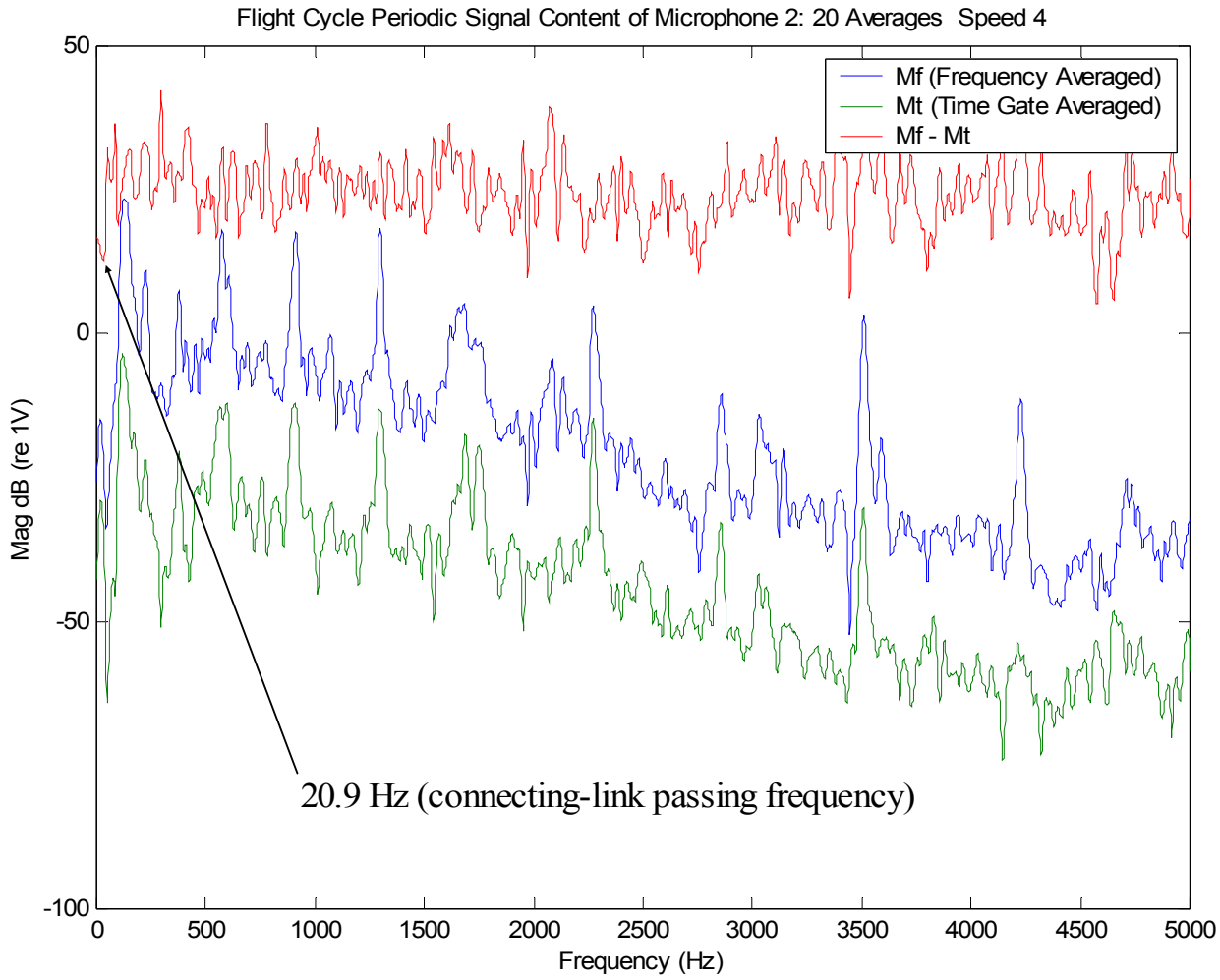

Figure 30 Time-Averaged / Frequency-Averaged Response Microphone 2 Speed 4

When examining the difference between the enhanced time and the normal spectra in Figure 29, the connecting-link frequency of 7.7 Hz at speed 1 clearly stands out as related to the flight cycle. At this frequency, the difference between the frequency-averaged signal and the time-averaged signal is nearly zero. When the operating speed is increased to speed 4, the presence of the connecting-link passing frequency, now 20.9 Hz, is diminished by the amplified background noise as seen in Figure 30. As a result, it was determined that the connecting-links, especially the drive-links, impact the loading-end and motor-end tail sections and create structure-borne noise. Yet, when compared to peak responses of this near-field microphone signal, the connecting-link impacts contribute an insignificant amount of air-borne noise.

There is a slight presence of cycle related signal content at peak response frequencies. However, the difference is greater than 20 dB (re 1 V), and thus none of these are significant enough to be further investigated. Similar results and conclusions occur when triggering and measuring at the loading-end tail-section, except the peaks and humps are slightly less distinct. The accelerometers located on the spacer-plate and main conveyor sections do not contain significant cycle related signal content, nor does far-field microphone 3, irrespective of which tail-section was used for triggering.

5.0 CONCLUSIONS AND FUTURE WORK

The techniques used to analyze the chain conveyor / motor test bed effectively revealed the noise characteristics of the system. Near-field sound pressure and sound intensity determined the locations of noise sources through the use of contour plots conformal to the surface of the system. Primary noise sources occur at areas corresponding with the highest levels. Additionally, gradient arrows can be added to the acoustic intensity contour plots to show the variation across the surface. Specific peak frequencies produced by noise sources were identified from the sound pressure and sound intensity spectra. Corresponding 1/3-octave values were used to determine the frequency bands where system energy is concentrated. Although often considered bad practice to measure sound pressure in the near-field, the near-field sound pressure analysis proved to be very effective, when contrasted to sound intensity results. Near-field sound pressure levels were consistently greater than corresponding sound intensity values, indicating the presence of reactive field components. Future sound intensity measurements could include those taken with a shorter probe spacer(s) so that higher frequency data could be obtained in order to cover the 20-8,000 Hz range. Note that normal intensity could also be integrated over the measurement surface in order to determine sound power from part or all of the system while *in-situ*.

Structural tap testing combined with near-field sound pressure and sound intensity revealed frequencies where there is potentially structural radiation. Suspected frequencies must be checked against driving frequencies in order to rule them out and verify that radiation is actually produced by structural vibration. Future tap testing could investigate the potential of simultaneous microphone and accelerometer measurements at a close proximity to each other in order to directly measure structural-acoustic transfer functions. However, a very quiet environment (anechoic) would be required. This technique could potentially provide a more accurate means of relating the radiation of structural modes to the acoustic environment surrounding the component. Additionally, it may be possible to implement coherence techniques on these measurements to gain insight to the spectral efficiency of structural-acoustic transfer. Overall, the tap test technique proved to be effective. However, similar information was gleaned from the coherence analysis, with much less effort.

Coherent power measurements identify specific noise source contributions and transmission paths. The Frequency Response Function (FRF) and Partial Coherence Function (PCF) methods were analyzed in this thesis. The FRF method was much simpler to use since only one equation was required to provide source contribution results. PCF coherent power computations are much more complex due to the use of multiple equations needed to reveal an individual source contribution. The FRF method is well suited to identify noise source contributions for systems with low source coherence and when used in environments with low levels of background noise. The PCF method provides the ability to determine the unique source contributions of a well-defined system. A well-defined system is one in which system sources are identifiable with slight or no coherence. Other interesting data if possible would be accelerometer and microphone data from the moving chain and flights. However this would inflict great risk of destroying expensive equipment and the consequences should be seriously weighed against the potential results. Coherent power measurement techniques are very useful for noise source investigation and should be considered the starting point for all noise source investigations due to the simplicity of their implementation.

Enhanced time measurements provide the ability to separate cycle related signal content. A trigger signal must be generated from some cycle component or process. The technique can be applied to near-field acoustic pressure or vibration measurements. Humps in the enhanced time signal are correlated with the position of suspect moving components. Information about the mechanisms of sound generation (e.g. gear tooth impact) can often be determined from the analysis. These signals can also be converted to the frequency domain using the Fast Fourier Transform (FFT). Comparison of corresponding time-averaged and frequency-averaged signal content reveal the contribution of air-borne noise caused by a cyclic impact.

System analysis performed with the techniques discussed above all revealed that the loading-end and the motor-end tail-sections are the dominant noise sources while the motor has a smaller contribution than all of the other conveyor components. Thus, analysis focused on these conveyor sections. The inside of the test bed, discontinuities, and areas of impact also contribute to system noise levels. As a result, all of these should be the focus of noise control methods. The main section and side-sections of the conveyor seem to contribute noise, however their levels were not as significant compared to other conveyor sections.

As expected, the system is very loud and presents the potential for a significant amount of hearing loss to an operator without or improperly used hearing protection especially at high operation speeds. Findings provide that the larger main section produces less noise than the tail-sections. It is suspected that the nature of impact received from the chain components is directly correlated with the noise contribution of each section. Enhanced time measurements revealed that the tail-sections received cyclic impact from the chain linkage. Since impacts are a source of air-borne and structure-borne noise they should be reduced or eliminated. A rail or roller type chain guide track and alternate drive gear material are a few suggested solutions. Also, the addition of damping controls to radiating components would be beneficial. Examples of these would include surface coatings on panels and other sound radiating surfaces, and the isolation of acoustic power inside the waveguide-like conveyor component. From an administrative controls standpoint, the operator should avoid the tail sections and any holes along the sides.

The analysis techniques used in this project proved to be effective. It would be interesting to apply these techniques to more complex mining systems, such as continuous miners, long wall miners, shuttle cars, and roof bolters, which would provide a more significant challenge to the measurement techniques due to the presence of multiple prime movers and noise sources. The methods can be applied to treated and untreated systems in order to quantify the effectiveness of treatments as well as “see” the resulting noise distributions. Knowledge of these noise identification techniques is significant because they can ultimately contribute to the implementation of effective noise reduction treatments and devices to ensure a safer work environment for miners.

APPENDICIES

APPENDIX A

SOUND INTENSITY PROBE CALIBRATION

The sound intensity probe was calibrated using a Brüel & Kjær 3541 sound intensity calibrator. Sound pressure and sound intensity were measured with the probe microphones inserted into the Brüel & Kjær 4228 piston-phone component which was attached to the Brüel & Kjær ZI 0055 broad-band noise source. Both sound intensity between the microphones and sound pressure level were simultaneously measured. The magnitude of the intensity spectrum was subtracted from the pressure spectrum resulting in the Residual Pressure-Intensity Index (the blue line in Figures 31-34). The Dynamic Capability (green line in Figures 31-34) of the probe was then determined by subtracting 10 dB from the Residual Pressure-Intensity Index spectrum. The Pressure-Intensity Index spectrum (red line in Figures 31-34) for each measurement made on the system was obtained by subtracting the corresponding sound intensity from the sound pressure measured at that point. The usable bandwidth of the sound intensity probe is the region where the Pressure-Intensity Index is less than the Dynamic Capability of the probe. The usable region was selected as 20-4,000 Hz for this thesis and is shown to the left of the vertical line at 4 kHz in Figures 31 through 34.

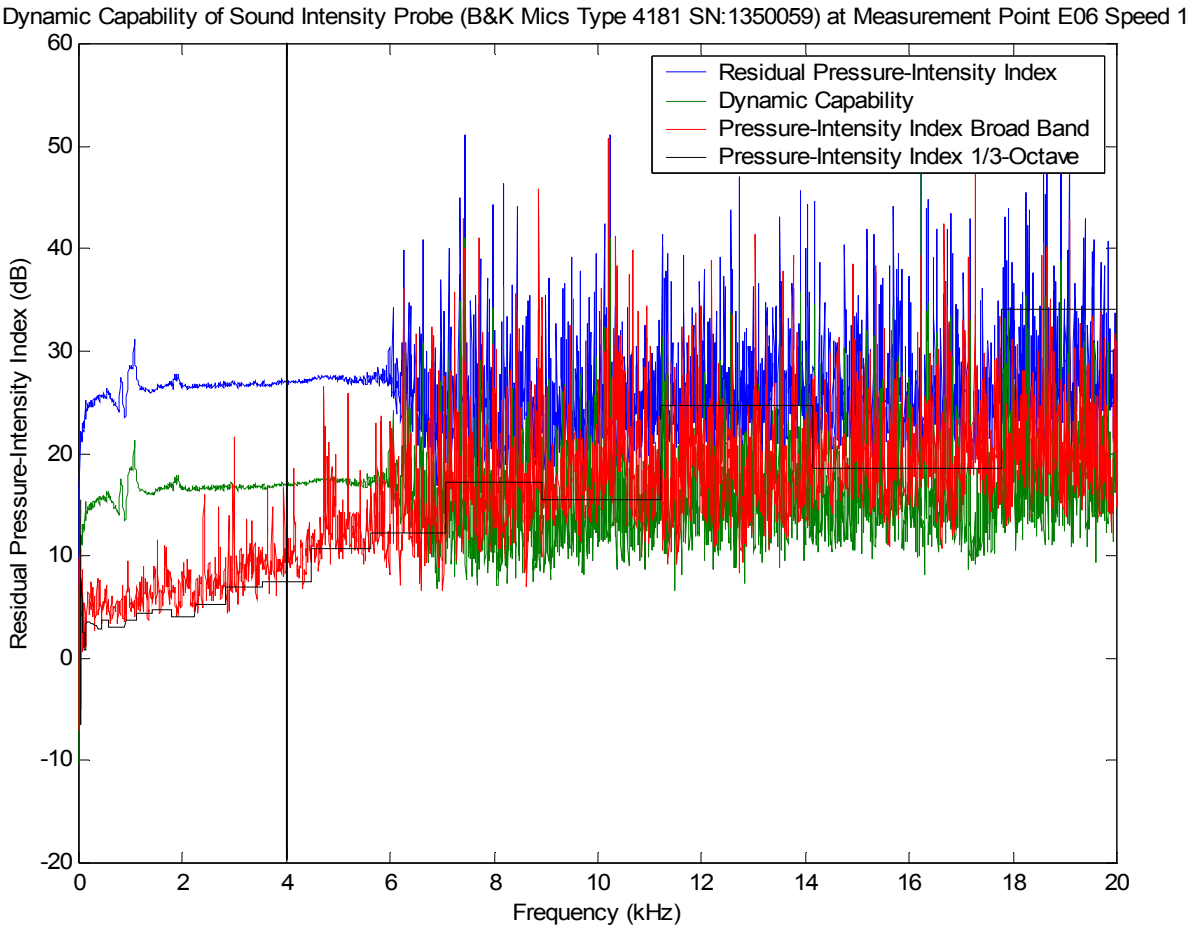

Figure 31 Dynamic Capability at Measurement Point E06 Speed 1

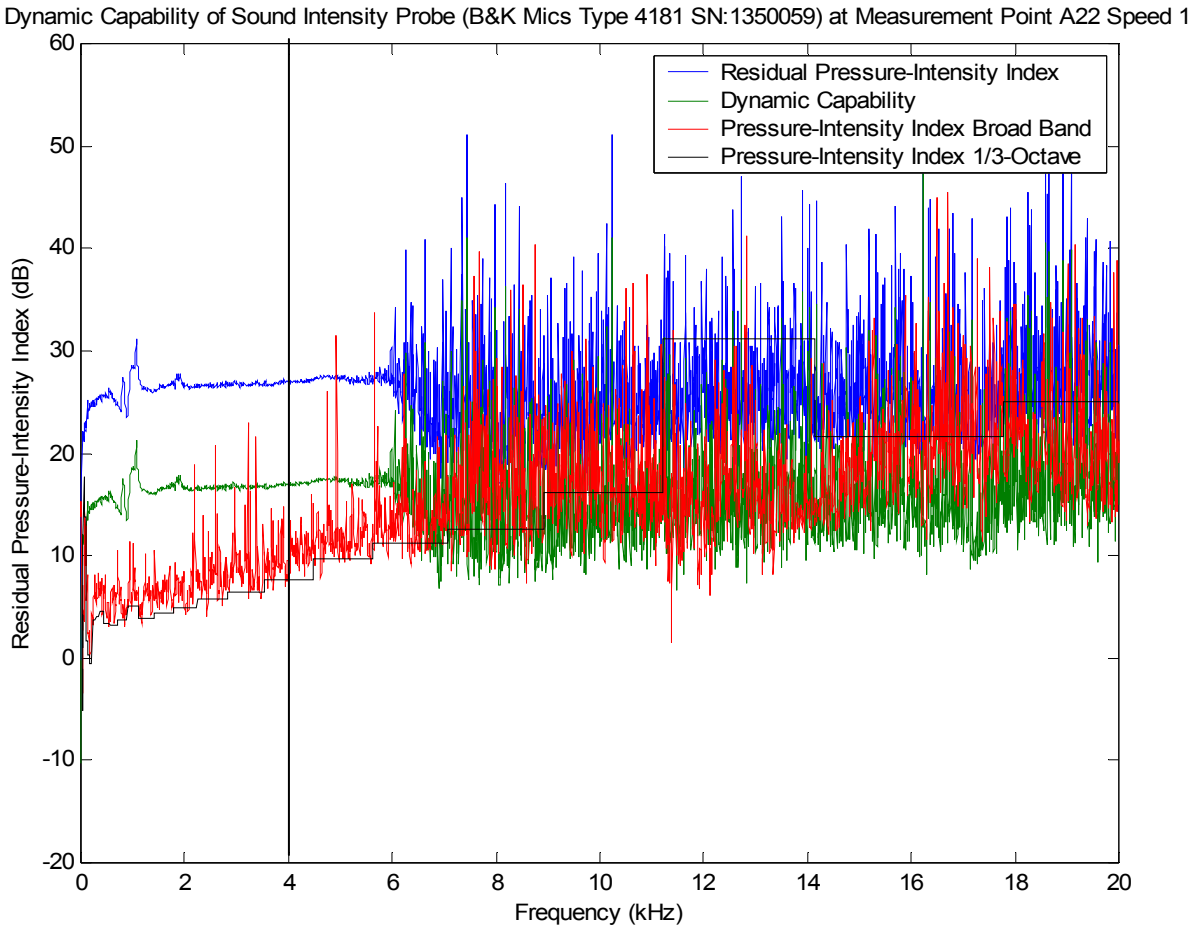

Figure 32 Dynamic Capability at Measurement Point A22 Speed 1

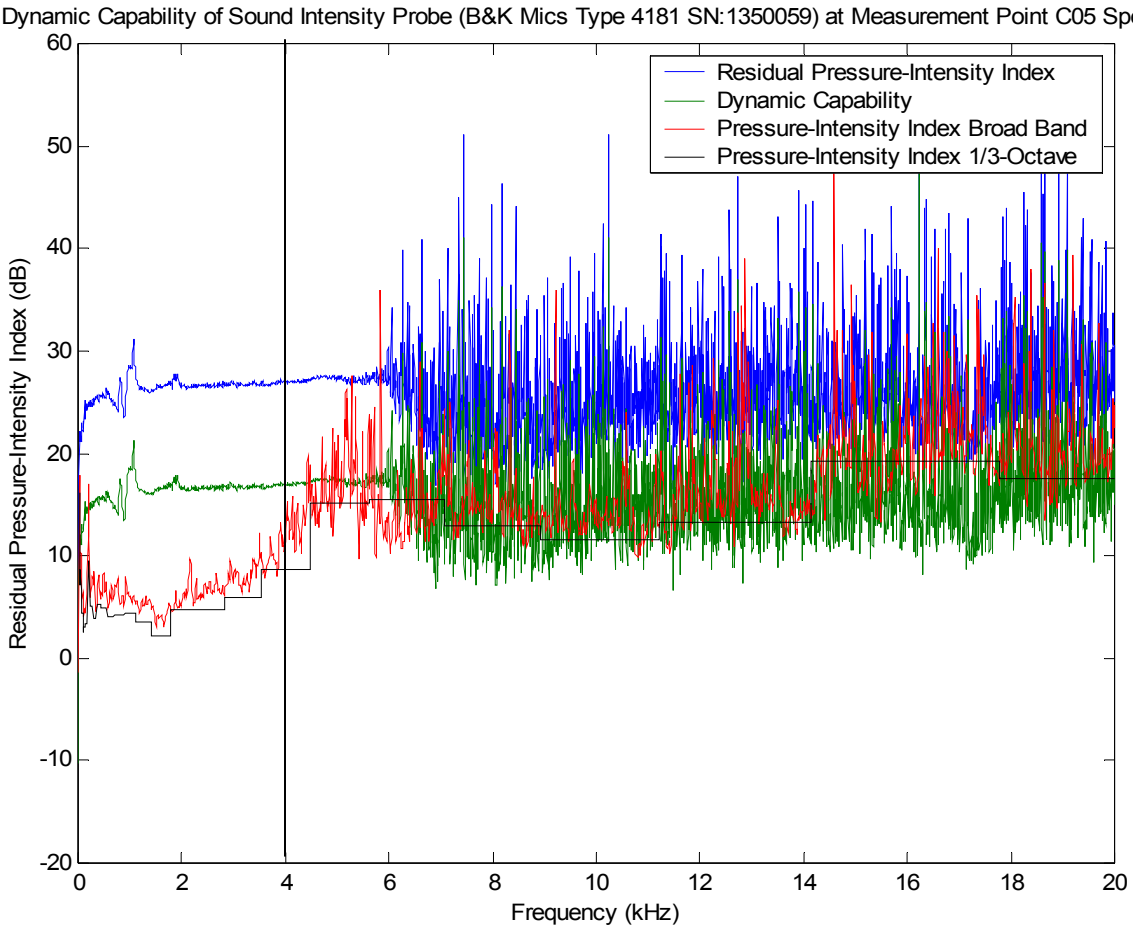

Figure 33 Dynamic Capability at Measurement Point C05 Speed 4

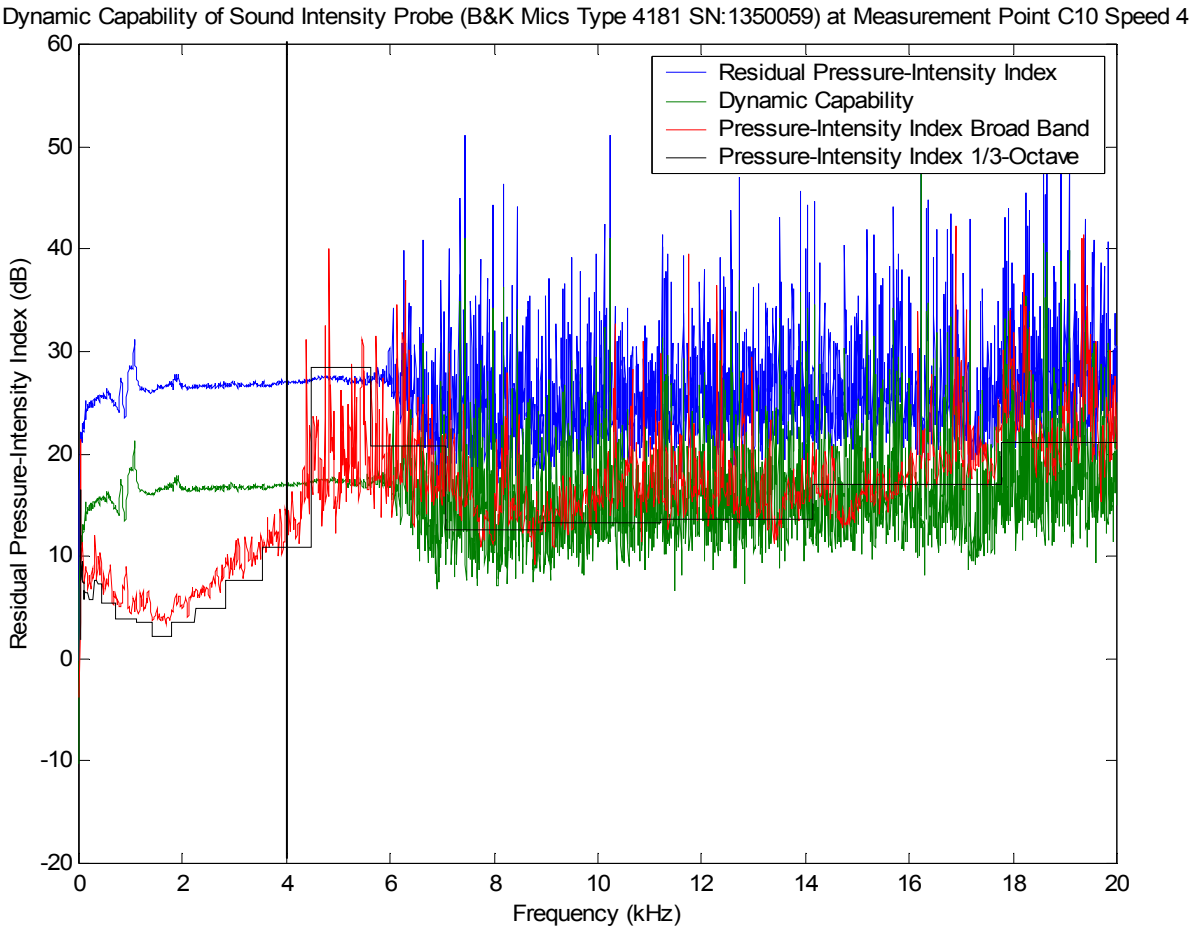

Figure 34 Dynamic Capability at Measurement Point C10 Speed 4

APPENDIX B

ADDITIONAL CONVEYOR PICTURES

Figure 35 Loading-end Tail-section Left Side View Showing Chain Tensioner Spring

Figure 36 Chain Conveyor / Motor Test Bed Left Side View

Figure 37 Motor / Transmission Component

Figure 38 Motor-end Adjustable Discontinuity Right Side View

Figure 39 Loading-end Adjustable Discontinuity Right Side View

BIBLIOGRAPHY

BIBLIOGRAPHY

1. Alberti, P.W., ed. *Personal Hearing Protection in Industry*, Raven Press, New York, 1982.

2. Aljoe, W.W., Bartholomae, R.C., Bobick, T.G., and Redmond, G. W., "The Bureau of Mines Noise-Control Research Program – A 10-Year Review," *Bureau of Mines Information Circular 9004*, Bureau of Mines – USDOI, 1985.

3. Andersen, D., Galaitsis, A., and Madden, R., "Noise Reduction of Chain Conveyors Vol. I," *Bolt Beranek and Newman Inc.*, Bureau of Mines – USDOI, Dec. 1979.

4. ANSI / ASME PTC 36-1985. *Measurement of Industrial Sound*, The American Society of Mechanical Engineers, New York, 1985.

5. ANSI S12.12-1992. *American National Standard: Engineering Method for the Determination of Sound Power Levels of Noise Sources Using Sound Intensity*, American National Standards Institute, New York, 1992.

6. ANSI S3.44-1996. *American National Standard: Determination of Occupational Noise Exposure and Estimation of Noise-Induced Hearing Impairment*, American National Standards Institute, New York, 1996.

7. Barber, A., *Handbook of Noise and Vibration Control*, 6th ed., Elsevier Science, Oxford, United Kingdom, 1992.

8. Bell, D. H., and Bell, L. H., *Industrial Noise Control: Fundamentals and Applications*, 2nd ed., Marcel Dekker, Inc., New York, 1994.

9. Bendat, J. S., and Piersol, A. G., *Random Data: Analysis and Measurement Procedures*, John Wiley & Sons, New York, 1971.

10. Bendat, J. S., "Modern Analysis Procedures for Multiple Input / Output Problems," *Journal of the Acoustical Society of America* (1980) 68(2), 498-503.

11. Bendat, J. S., "Solutions for the Multiple Input / Output Problem," *Journal of Sound and Vibration* (1976) 44(3), 311-325.

12. Blackstock, D. T., *Fundamentals of Physical Acoustics*, John Wiley & Sons, New York, 2000.

13. Chung, J. Y., "Cross Spectral Method of Measuring Acoustic Intensity without Error Caused by Instrument Phase Mismatch," *Journal of the Acoustical Society of America* (1978) 64(6), 1613-1616.

14. Crocker, M. J., and Jacobsen, F., "Sound Intensity," *Handbook of Acoustics*, Crocker, M. J., ed. John Wiley & Sons, New York, 1998, Ch. 106, 1327-1340.

15. Crocker, M. J., and Reinhart, T. E., "Source Identification on a Diesel Engine Using Acoustic Intensity Measurements," *Noise Control Engineering*, May-June 1982, 84-92.

16. Crocker, M. J., and Wang, M. E., "On the Application of Coherence Techniques for Source Identification in a Multiple Noise Source Environment," *Journal of the Acoustical Society of America* (1983) 74(3), 861-872.

17. Ewins, D. J., *Modal Testing: Theory and Practice*, Research Studies Press, Letchworth, England, 1986.

18. Fahy, F. J., *Sound and Structural Vibration: Radiation, Transmission, and Response*, Academic Press, London, 1985.

19. Fahy, F. J., *Sound Intensity*, 2nd ed., E & FN Spon, London, 1995.

20. Gade, S., Herlufsen, H., and Konstantin-Hansen, H., *Order Tracking of a Coast-down of a Large Turbogenerator*, Brüel & Kjær Application Note (BO 0469-11), Nærum, Denmark. 6 Feb. 2003. <http://www.bksv.com/pdf/Bo0469.pdf>

21. Giardino, D. A., and Marraccini, L. C., *Noise in the Mining Industry: An Overview* Mine Safety and Health Administration – USDOL, Pittsburgh, PA, 1981.

22. Ginn, K. B., *Noise Control Survey on a Pump Using the Gated Technique*, Brüel & Kjær Application Note (BO 0388-11), Nærum, Denmark. 6 Feb. 2003. <http://www.bksv.com/pdf/Bo0388.pdf>

23. Harris, C. M., ed. *Handbook of Acoustical Measurements and Noise Control*, 3rd ed., McGraw-Hill, New York, 1991.

24. *Health Standards to Protect Miners from Hearing Loss*, Mine Safety and Health Administration – USDOL, 1 Sept. 1999. 23 March 2003. <http://www.msha.gov/1999noise/noiseinfo.pdf>

25. ISO 3745-1977. *International Standard: Acoustics – Determination of Sound Power Levels of Noise Sources – Precision Methods for Anechoic and Semi-Anechoic Rooms*, International Organization for Standardization, Geneva, Switzerland, 1982.

26. ISO 3746-1995. *International Standard: Acoustics – Determination of Sound Power Levels of Noise Sources Using Sound Pressure – Survey Method Using an Enveloping Measurement Surface Over a Reflecting Plane*, International Organization for Standardization, Geneva, Switzerland, 1995.

27. ISO 9614-1:1993. *International Standard: Acoustics – Determination of Sound Power Levels of Noise Sources Using Sound Intensity – Part 1: Measurement at Discrete Points*, International Organization for Standardization, Geneva, Switzerland, 1993.

28. Konstantin-Hansen, H., *Gated Tracking Applied on an Automobile Engine Using Multichannel Analysis System Type 3550*, Brüel & Kjær Application Note (BO 0444-11), Nærum, Denmark. 6 Feb. 2003. <http://www.bksv.com/pdf/Bo0444.pdf>

29. Miller, R. K., and Thumann, A., *Fundamentals of noise control engineering*, 2nd ed., Fairmont Press, Lilburn, GA, 1990.

30. *Mining Facts – 2001 Publication No. 2003-105*, National Institute for Occupational Safety and Health – DHHS, Feb. 2003. 19 March 2003. <http://www.cdc.gov/niosh/mining/data/pdfs/fact2001.pdf>

31. *MSHA News Release No. 99-0909*, Mine Safety and Health Administration – USDOL, 9 Sept. 1999. 12 March 2003. <http://www.msha.gov/media/press/1999/nr990909.htm>

32. *Noise Exposure Computation – 1910.95 App A*, Occupational Safety and Health Administration – USDOL, 6 Jan. 2003. <http://www.osha.gov/pls/oshaweb/owadisp.show_document?p_table=STANDARDS&_id=9736&p_text_version=FALSE>

33. Rao, S. S., *Mechanical Vibrations*, 3rd ed., Addison-Wesley, New York, 1995.

34. Rasmussen, G., "Intensity – Its Measurement and Uses," *Sound and Vibration*, March 1989, 12-21.

35. Sataloff, J., and Sataloff, R. T., *Occupational Hearing Loss Second Edition, Revised and Expanded*, Marcel Dekker, New York, 1993.

36. Wilson, C. E., *Noise Control: Measurement, Analysis, and Control of Sound and Vibration*, Harper & Row, New York, 1989.

37. Wismer, N. J., *Time Domain Averaging Combined with Order Tracking*, Brüel & Kjær Application Note (BO 0420-11), Nærum, Denmark. 6 Feb. 2003. <http://www.bksv.com/pdf/Bo0420.pdf>